Catalysts Design for Ammonia Synthesis at Room Temperature

by

Qinye Li

A dissertation submitted for the degree of Doctor of Philosophy in the Department of Chemical Engineering at Monash University

June 2019

Supervisors: Prof. Xiwang Zhang
Dr. Lizhong He

Department of Chemical Engineering

Copyright notice

Thesis including published works declaration

I hereby declare that this thesis contains no material which has been accepted for the award of any other degree or diploma at any university or equivalent institution and that, to the best of my knowledge and belief, this thesis contains no material previously published or written by another person, except where due reference is made in the text of the thesis.

This thesis includes 3 original papers published in peer reviewed journals and 2 submitted publications. The core theme of the thesis is catalysts design for ammonia synthesis at room temperature. The ideas, development and writing up of all the papers in the thesis were the principal responsibility of myself, the student, working within the Department of Chemical Engineering under the supervision of Prof. Xiwang Zhang.

(The inclusion of co-authors reflects the fact that the work came from active collaboration between researchers and acknowledges input into team-based research.)

In the case of *chapter 2-6* my contribution to the work involved the following:

Thesis Chapter	Publication Title	Status (published, in press, accepted or returned for revision, submitted)	Nature and % of student contribution	Co-author name(s) Nature and % of Co-author's contribution*	Co-author(s), Monash student Y/N*
2	*Insight into the Reactivity of Carbon Structures for Nitrogen Reduction Reaction*	*Published*	70%. Concept and collecting data and writing first draft	1) Siyao Qiu 5% 2) Chuangwei Liu 5% 3) Fengling Zhou 5% 4) Lizhong He 5% 5) Xiwang Zhang 5% 6) Chenghua Sun 5%	1) Yes 2) Yes 3) No 4) No 5) No 6) No
3	*Computational Study of MoN2 Monolayer as Electrochemical Catalysts for Nitrogen Reduction*	*Published*	80%. Calculations, collecting data and writing first draft	1) Lizhong He 5% 2) Chenghua Sun 5% 3) Xiwang Zhang 10%	1) No 2) No 3) No
4	*Exploration of iron borides as electrochemical catalysts for nitrogen reduction reaction*	*Submitted*	70%. Calculations, collecting data and writing first draft	1) Chuangwei Liu 5% 2) Siyao Qiu 5% 3) Lizhong He 5% 4) Xiwang Zhang 10% 5) Chenghua Sun 5%	1) Yes 2) Yes 3) No 4) No 5) No

				1) *Siyao Qiu 5%*	1) *Yes*
5	*Impact of H-termination on the nitrogen reduction reaction of molybdenum carbide as an electrochemical catalyst*	*Published*	*75%. Calculations, collecting data and writing first draft*	1) *Siyao Qiu 5%* 2) *Lizhong He 5%* 3) *Xiwang Zhang 10%* 4) *Chenghua Sun 5%*	1) *Yes* 2) *No* 3) *No* 4) *No*
6	*Computational Design of Single-Molybdenum Catalysts for the Nitrogen Reduction Reaction*	*Published*	*70%. Calculations, collecting data and writing first draft*	1) *Siyao Qiu 5%* 2) *Chuangwei Liu 5%* 3) *Mingguo Liu 5%* 4) *Lizhong He 5%* 5) *Xiwang Zhang 5%* 6) *Chenghua Sun 5%*	1) *Yes* 2) *Yes* 3) *No* 4) *No* 5) *No* 6) *No*

*If no co-authors, leave fields blank

I have / have not renumbered sections of submitted or published papers in order to generate a consistent presentation within the thesis.

Student signature: (Qinye Li) Date: 22-06-2019

The undersigned hereby certify that the above declaration correctly reflects the nature and extent of the student's and co-authors' contributions to this work. In instances where I am not the responsible author I have consulted with the responsible author to agree on the respective contributions of the authors.

Main Supervisor signature: (Xiwang Zhang) Date: 22-06-2019

Acknowledgement

My PhD study started on 29th Feb 2016 and will finish after I submit this thesis. I like to take this opportunity to express my deepest gratitude to those who have helped and supported me in the past three years.

Qinye

June 2019

Table of contents

Chapter 4 FeBx nanosheets as NRR catalyst

Chapter 5 Mo₂C nanosheets as NRR catalyst

Chapter 6 Single-atom catalyst for NRR

Chapter 7 Summary and future work

Publications during enrolment

❖ Journal articles

Q. Li, L. He, C. Sun, X. Zhang. Computational Study of MoN2 Monolayer as Electrochemical Catalysts for Nitrogen Reduction, *J. Phys. Chem. C* 121, 27563-27568 (2017).

Q. Li, S. Qiu, L. He, X. Zhang, C. Sun. Impact of H-termination on the nitrogen reduction reaction of molybdenum carbide as an electrochemical catalyst, *Phys. Chem. Chem. Phys*. 20, 23338-23343 (2018).

Q. Li, S. Qiu, C. Liu, M. Liu, L. He, X. Zhang, C. Sun. Computational Design of Single-Molybdenum Catalysts for the Nitrogen Reduction Reaction, *J. Phys. Chem. C* 123, 2347–2352 (2019).

Q. Li, C. Liu, S. Qiu, F. Zhou, L. He, X. Zhang, C. Sun. Exploration of iron borides as electrochemical catalysts for nitrogen reduction reaction. *J. Mater. Chem. A*, 7, 21507-21513 (2019).

Q. Li, S. Qiu, C. Liu, F. Zhou, L. He, X. Zhang, C. Sun. Insight into the Reactivity of Carbon Structures for Nitrogen Reduction Reaction. *ACS Catal*. submitted.

C. Liu, **Q. Li**, J. Zhang, Y. Jin, D.R. MacFarlane, C Sun. Theoretical Evaluation of Possible 2D Boron Monolayer in N2 Electrochemical Conversion into Ammonia. *J Phys. Chem. C* 122, 25268-25273 (2018).

C. Liu, **Q. Li**, J. Zhang, Y. Jin, D. MacFarlane, C. Sun. Conversion of dinitrogen to ammonia on Ru atoms supported on boron sheets: a DFT study. *J Mater. Chem. A* 7, 4771-4776 (2019).

C. Liu, **Q. Li**, C. Wu, J. Zhang, Y. Jin, D. MacFarlane, C. Sun. Single-Boron Catalysts for Nitrogen Reduction Reaction. *J. Am. Chem. Soc.* 141, 2882-2888 (2019).

Q. Yu, Y. Luo, S. Qiu, **Q. Li**, Z. Cai, Z. Zhang, J. Liu, C. Sun, B. Liu. Tuning the Hydrogen Evolution Performance of Metallic 2D Tantalum Disulfide by Interfacial Engineering. *ACS Nano*. Published online. DOI: 10.1021/acsnano.9b05933.

❖ Conference abstract

Defective graphene as catalysts for electrochemical ammonia synthesis. Carbon 2017.

Abstract

In this thesis, computer-aided catalysts design for nitrogen reduction reaction (NRR) has been presented. NRR is an essential process for the nitrogen-to-ammonia conversion, a critical process for modern chemistry and agriculture. Current expectation is to turn industry Haber-Bosch process to a green alternative, like ammonia production at room temperature without carbon footprints. The key is to develop high performance catalysts.

Novel catalysts for electrochemical synthesis has been targeted by this project. Specifically, three types of catalysts have been explored computationally, including graphene-based metal free catalysts, two-dimensional nanosheets (MoN_2, FeBx, Mo_2C) and single-Mo catalysts. As demonstrated by the calculations under the scheme of density functional theory, a series of promising candidates, including lowly coordinated carbon, nitrogen vacancies, hypercoordinated iron in FeB_6 nanosheets and Mo mediated by boron and carbon ligands, have been identified. These structures offer a performance similar or even better than flat Ru(0001), which has been viewed as one of the best catalysts for electrochemical NRR.

Through advanced analysis of these individual catalysts, it is found that these catalysts often present lowly coordinated active centre, which is helpful to break the linear constraint relationship between intermediate states. Moreover, active centres can be effectively mediated by defects, local coordination, dopants and ligands. Theoretical calculations can provide strong support for such efforts through screening the adsorption energy of single nitrogen and hydrogen to predict NRR thermodynamics and selectivity. Such strategy has been employed for the design of single-atom catalysts in this project.

Although kinetics prediction is still difficult due to the theoretical difficulties, these efforts from this PhD project provide promising candidates for experimental studies, together with insights on the reaction mechanism and advanced knowledge regarding the rational design of NRR catalysts. This paves the way to green ammonia production.

Nomenclature

2D: Two-dimensional

AE: Adsorption energy

ARC: Australian Research Council

ATM: Atmosphere

BP: Black phosphorus

CAMD: Computer-aided materials design

DG: Defective graphene

DFT: Density functional theory

DOS: Density of states

FE: Faraday efficiency

GGA: Generalised gradient approximation

HER: Hydrogen evolution reaction

HOMO: Highest occupied molecular orbitals

HPC: High performance computational

LCC: Lowly coordinated carbon

Mo_2C: Molybdenum carbide

MoN_2: Molybdenum nitride

NG: N-doped graphene

NRR: Nitrogen reduction reaction

NSG: N-S co-doped graphene

NV: Nitrogen vacancy

OG: O-doped graphene

O-HC: O-doped hollow carbon

PDS: Potential determining step

Os: Project objectives

RDS: Rate-determining step

RPBE: Revised Perdew-Burke-Ernzerhof

SACs: Single-atom catalysts

S-CNS: S-doped carbon nanospheres

SG: S-doped graphene

SHE: Standard hydrogen electrode

TMs: Transition metals

ZPE: Zero-point energy

Chapter 1 Introduction and Literature Review

1.1 Introduction

With the development of high performance computational (HPC) clusters, computers have become a powerful tool for new materials development. The most recent benchmark is the success reported by P. Raccuglia et al. that novel organic-inorganic materials have been designed through machine-learning from failed experiments [1]. Different from lab-based tests, computer-aided materials design can be performed based on computational calculations, in which new materials can be evaluated prior to the material synthesis [2]. The key merit is that thousands of candidates can be computationally tested through parallel calculations, which not only saves the time and money, but also advances the knowledge because 'unsuccessful' candidates will be thoroughly examined against the criteria to obtain fundamental insights.

This PhD program is a computational project, with most of the research activities being performed by first principle calculation, focusing on the development of advanced catalysts for NRR, which is the basis for ammonia synthesis. As one of the key industry reactions, various approaches have been developed for the large-scaled production of ammonia, among which the Haber−Bosch process is the most successful one. However, it is operated at high temperature 400-500^0 C and high pressure 15-25 MPa, consuming around 2% of global energy; more importantly, such huge energy consumption is not necessarily required based on the reaction thermodynamics as the real challenge comes from the kinetics, more specifically due to the activation of nitrogen.

In chemistry, the role of catalysts is to speed up reaction through reducing the reaction barrier and improving the kinetics, which is exactly demanded for ammonia synthesis. To reduce the energy consumption and carbon emission associated with ammonia industry, it is ideal to produce ammonia at mild condition. This is possible, and actually is the way how nature produces ammonia: root nodule bacteria synthesize ammonia from air and water at room temperature and normal pressure. Different from bacteria, industry production needs high efficiency and reasonable cycle, achieving the production capacity of millions tons each year. The key is catalysts.

1.2 Literature Review

1.2.1 Ammonia Synthesis

Ammonia ($NH3$) is one of the key industry chemicals, which has been widely used for the production of fertilizers and plays a key role for modern agriculture [3, 4]. Currently, the industry production is based on the Haber-Bosch process [5],

$$N_2 + 3\ H_2 \rightarrow 2NH_3 \qquad \Delta H^0 = \text{-91.8 kJ}, \Delta G^0 = \text{-32.8 kJ} \qquad (1)$$
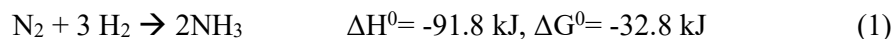
in which nitrogen (N_2) and hydrogen (H_2) are dissociated as N- and H-adatoms over catalysts, namely dissociative mechanism, as described by the following elementary reactions [6]:

$$N_2\ (g) + * \rightarrow N_2* \qquad\qquad (2)$$

$$N_2* \rightarrow 2N* \qquad\qquad (3)$$

$$H_2\ (g) + * \rightarrow *H_2 \qquad\qquad (4)$$

$$H_2* \rightarrow 2H* \qquad\qquad (5)$$

$$N* + 3H* \rightarrow NH_3* \qquad\qquad (6)$$

$$NH_3* \rightarrow NH_3(g) + * \qquad\qquad (7)$$
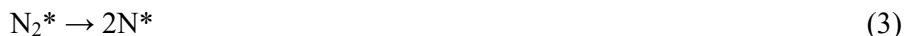
Typically, the reaction is conducted at 15-25 MPa and between 400-500 °C. As indicated by the thermodynamics, the reaction is an exothermic reaction, and can happen, in theory, spontaneously; however, ammonia synthesis is an energy-extensive process, which accounts for around 2% of the global energy consumption [7]. The challenge is the kinetics: nitrogen molecules are extremely stable due to the triple bond between two nitrogen atoms, with a bond strength of 941 kJ/mol; as a result, the free energy change for Reaction (3) is very high [8]. To date, it remains a challenge to develop effective catalysts for nitrogen dissociation. Given the overall reaction is exothermic, high performance catalysts should be capable to adsorb nitrogens and promote their dissociation, ideally at room temperature. After extensive effort over half century, iron-based catalysts have been identified as an promising catalyst due to its low cost and effectiveness. The main issue for Fe-catalyst is the optimal working temperature, which is around 500 °C. To achieve the ammonia synthesis at room temperature, electrochemical approaches have been proposed.

1.2.2 Electrochemical Synthesis of Ammonia

Different from the Haber-Bosch process, hydrogen is provided in electrochemical synthesis through the pair of proton (H+) and electron (e-), described as,

$$N_2 + 6(H^+ + e^-) \rightarrow 2NH_3 \qquad\qquad (8)$$
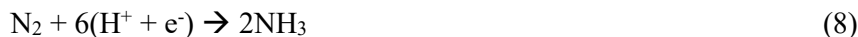
Compared with Haber-Bosch process, it has two key advantages: (i) Theoretically, the reaction can be performed under room temperature with an applied external potential, which can save large amount of energy by removing unnecessary high temperature of Haber-Bosch process; and (ii) Such reaction can be carried out using small-scale electrochemical devices at ambient conditions, without building large chemical plants. As such, the reaction can be driven using electricity, which can be generated by small solar- or wind-powered devices. This is of great values because many farms, which are often far away from the fertilizer plants, can get fertilizer from local small devices without the cost associated with the shipping and storage of fertilizer.

Theoretically, several elementary steps are involved for Reaction (8), as schematically shown in Figure 1 [9]. In the scheme, several potential reaction paths are proposed and need to be determined based on the energy profiles. The key challenge is the development of the catalyst which can adsorb and reduce nitrogen. Compared with the dissociative mechanism involved in Haber-Bosch process, electrochemical reduction of nitrogen starts with the associative adsorption of nitrogen to the catalysts, which is often referred as associative mechanism. It is worth to mention that this is how the nature produces ammonia from nitrogen using nitrogenase enzymes at ambient conditions, as observed in nodule bacteria.
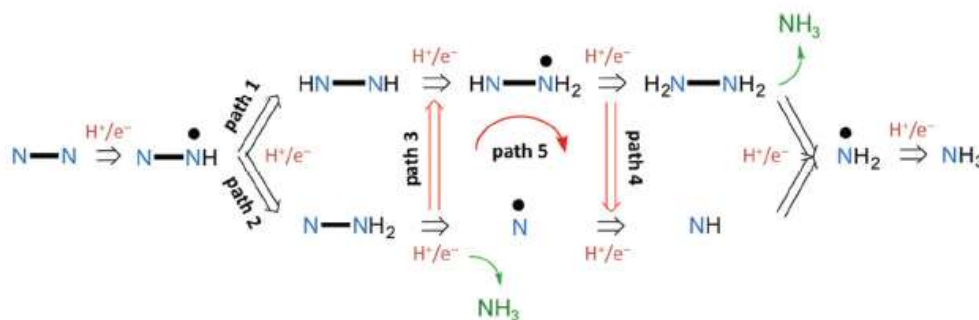
Figure 1 Schematic reaction paths for NRR. Reprinted with permission from [9]. Black dots indicate radicals.

1.2.3 NRR Catalysts

For nodule bacteria, nitrogen reduction is conducted at room temperature, without large amount of electricity supply, providing a vivid example to learn from the nature. 'Learning from the Nature' is the key philosophy of this PhD program. Based on this philosophy, the systems listed in the project objectives (POs) are proposed; nitrogenases are actually a [FeMo]-based catalyst [10], as shown in Figure 2. It is composed of Fe-protein and MoFe protein, containing three Metal-cores as the reactive centre, namely, F-cluster, P-cluster and M-cluster. Currently, it is widely accepted that the NRR actually occurs over the M-cluster, more specifically on Fe-centre [11-14].
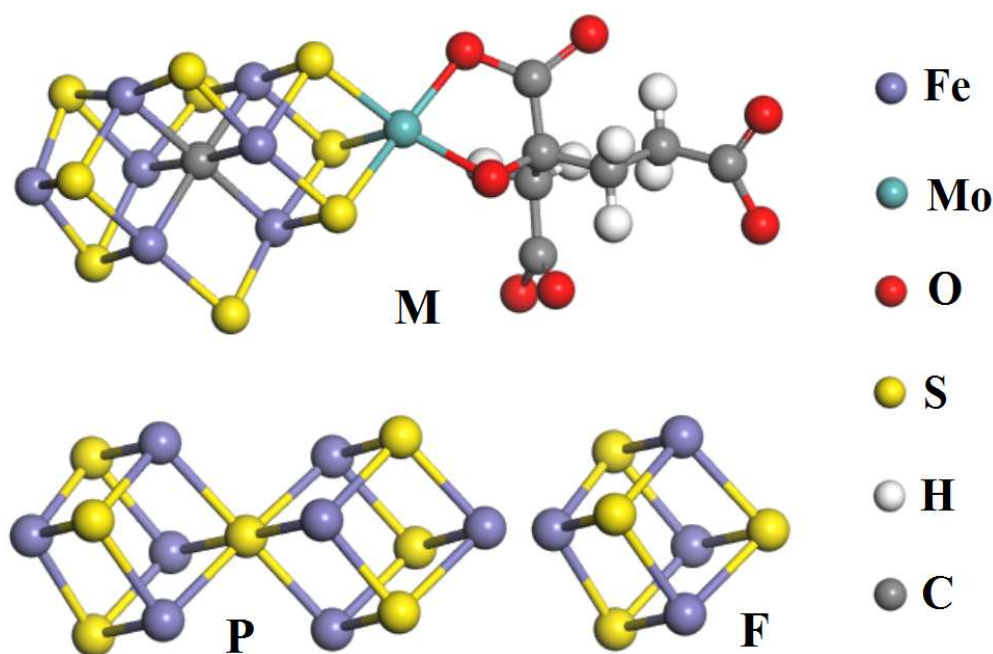
Figure 2 Schematic structure of metal cores (F, P, M) contained in nitrogenase enzymes.

Examining the M-cluster, it is found that Fe, S, C, and Mo are involved, with organic ligands connected to the two oxygen atoms bonded to Mo, as shown in Figure 2. Interestingly, current industry catalyst for Haber-Bosch process is also based on iron compounds [15]. Bio-inspired molecular catalysts are very attractive and have been studied extensively, in most cases the catalytic centre is low-coordinated Fe-atoms in multinuclear iron complexes [16-18]. For instance, iron nitride has been employed [16], in which nitrogen is firstly introduced to bond with iron to form nitride and then react with the proton and electron pair. Another example is

iron-potassium complex, as shown in Figure 3 [18]. Although these molecular catalysts are structurally close to enzymes, their conductivity is often low, a big issue for electrochemical reactions; moreover, nitrogen is often directly introduced to the complex, and it is often a challenge to get stable complex with a low cost.
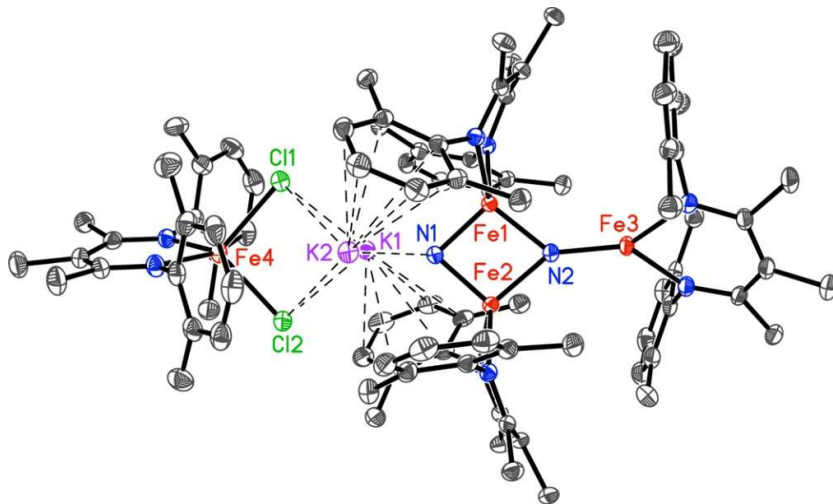
Figure 3: An example of iron-potassium complex as molecular catalysts for NRR. Nitrogen is stabilized by iron and potassium. Reprinted with permission from [18].

Inorganic catalysts, especially metals, are widely employed as electrode in electrochemical devices; it has been extensively studied, including Au, Ag, Ru, Re, V, Co, Ir, Ni, etc [19-29]. After the efforts over one century, several systems have been identified as high performance NRR catalysts, such as Ag-Pd, Ni, Cu, etc, as summarized in a recent review [27]. So far, the reaction rates and faradaic efficiencies are achieved as high as 3.3×10^{-8} mol s^{-1} cm^{-2} [28] and 90.4% [29]. Currently, the operation temperature is typically in the range of 200-500 °C [27], underlining the need to develop better catalysts to operate at room temperature.

During the development of nitrogen reduction reaction (NRR) catalysts, theoretical calculations have been proved to be an effective approach to understand the mechanism and predict new catalysts [30-32]. The typical way is to calculate the free energy profiles to establish the reaction routes with detailed thermodynamics information, serving as an indicator of the thermodynamic overpotential – a way to define how energy efficient the catalyst is. An example is shown in Figure 4 in which the free energy changes associated with the elementary steps are shown [32]. Clearly, Ru(211) and Re(111) are better NRR catalysts than Au(211) and V(110). Such calculations computationally compared different catalysts at the same level without the synthesis of such materials.

Ideally, new catalysts are still expected to deliver high performance without using expensive metals. At the same time, it is also important to avoid the side reactions to achieve higher efficiency. Given hydrogen evolution reaction (HER), $H^+ + e^- \rightarrow 1/2H_2$, can happen readily over most of these metals, protons may be consumed completely by HER rather than NRR. It is thus critical to compare HER and. As shown in Figure 5, the overpotentials for HER and NRR have been calculated and plotted in one figure for comparison [32], showing that HER is always easier than NRR for those metals – that is a key limitation for these metals. In reality, HER is always the key side reactions which should be seriously considered in catalysts design.
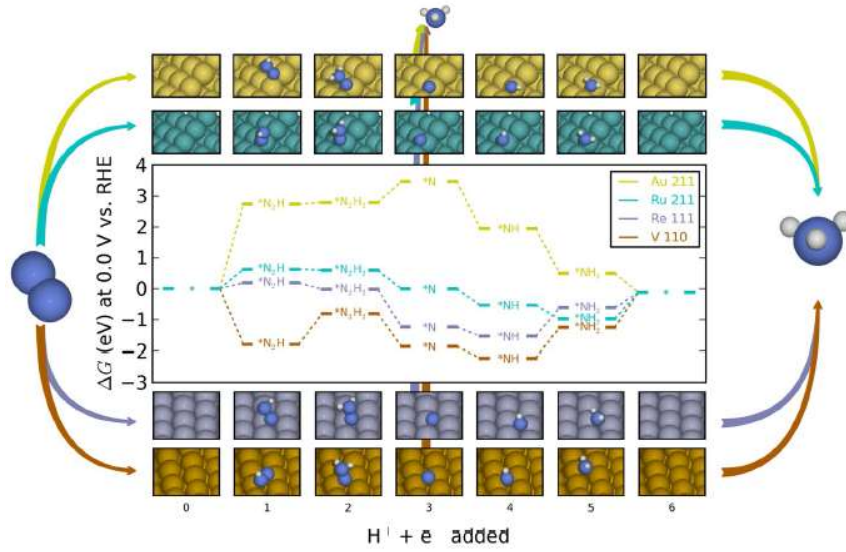
Figure 4. Free-energy diagram and optimized structures for the intermediate states involved in NRR. Reprinted from [32] with permission.
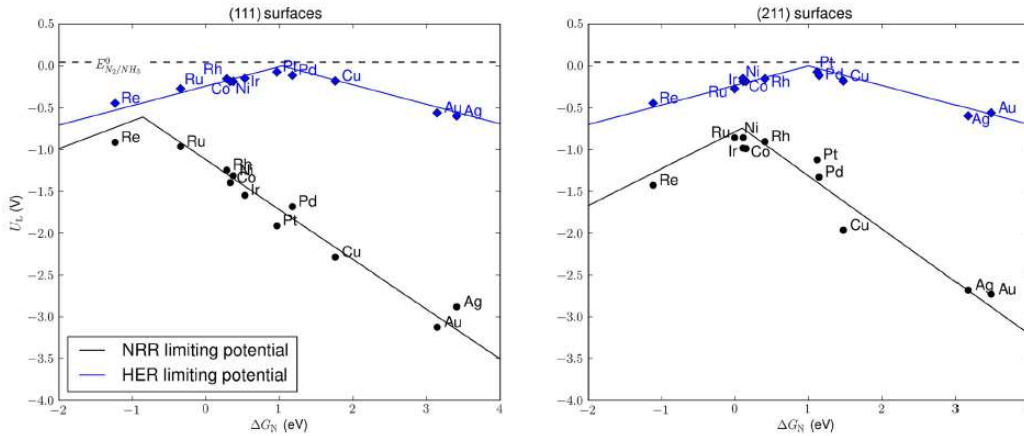
Figure 5. Calculated overpotentials of HER and NRR over different metals. For NRR, the free energy change of N bonding (ΔG_N) has been employed as an indicator for NRR, while for HER,

ΔG_H is often employed. Studied surfaces include (111) and (211). Plots are reprinted from [32] with permission.

1.3 Computer-Aided Catalysts Design for NRR

In recent years, two-dimensional (2D) materials are emerging as active catalysts, such as graphene, MoS_2, etc [33-35]. Different from traditional metal catalysts, 2D catalysts offer ultrahigh surface areas and high stability in the solution. Moreover, a lot of 2D materials have excellent conductivity, ideal for electrochemical reactions. This PhD program with a focus on 2D catalysts will thus explore several 2D materials as NRR catalysts.

Given computational modelling and calculations will be the key approach for this program, current progress on computer-aided catalysts design for NRR has been systematically reviewed and collected in Table 1. Specifically, these computational designs focus on two categories of catalysts, including bulk materials [36-60] and single-atom catalysts (SACs) [61-94], as listed in Table 1 and Table 2, respectively. Through studying these reports, computational approaches and key principles for catalysts design can be established, as introduced below.

1.3.1 Current Calculation Protocols

NRR is a typical multiple step reaction and the products of former step is the reactants for following ones; as a result, these intermediate states are not independent. Therefore, catalysts have to be optimized to suit all steps to achieve optimum performance. For this purpose, it is critical to calculate the free energy change ΔG for each elementary steps, being listed as ΔG_i, with i indicating the number of elementary reaction. The overall thermodynamics has been strongly determined by the maximum, $\Delta G_{max}=\max\{\Delta G_i\}$, which shows the thermodynamics barrier (minimum energy input) to drive these full NRR. The step associated with ΔG_{max} can be identified as the rate-determining step (RDS). Such barrier and RDS information has been collected for bulk catalysts and SACs in Table 1 and Table 2.

It is also noted that current calculations are overwhelmingly performed based on standard density functional theory, using Perdew-Burke-Ernzerhof (PBE) or revised PBE (RPBE) in most cases. In terms of calculation performance, PBE and RPBE show a notable difference. Using experimental data, the standard free energy change for gas-phase $N_2 + 3H_2 \rightarrow 2NH_3$ is -0.34 eV, while PBE and RPBE calculations lead to $\sim$ -0.7 eV and $\sim$-0.4 eV based on my tests. In other words, both DFT functionals have the risk to slightly overestimate the performance,

and RPBE seems to be more reliable, being consistent with the recommendation in the literature [92].

While reaction kinetics is critical, but for electrochemical reactions, the searching of transitional states (TS) is even more challenging. The first search is the treatment of separated protons and electrons, which are the reactants for NRR steps. To run TS searching, they have to be coupled as 'reactant state', shown as H*, assuming that the kinetic barrier does not coming from the proton-electron coupling, but from following steps. While this assumption has not been clarified yet, TS can be determined using H* as the starting state together with a compensate scheme [93]. Another key challenge is the treatment of interfacial field associated with electrocatalysis. As electrons are pumped to the electrode to react with protons and nitrogen, it may generate an electric field over the electrolyte/catalyst interface and affect the reaction kinetics. Such field is dynamically changing and can hardly be properly described by standard DFT. Due to these challenges, current computational design focuses on the thermodynamics calculations.

1.3.2 Current Rational Designs

As listed in Tables 1 and 2, current designs focus on bulk catalyst and SACs, with the later emerged as the dominant one. For the former, carbides and nitrides are widely studied, together with a couple of studies for oxides, borides and phosphides, in part, due to their high conductivity, that is essential for high performance electrocatalysts. So far, CoN, predicted by RPBE, has been best among the listed candidates, with a thermodynamics barrier of 0.23 eV, following by RuN (0.40 eV). Mo is very popular in the design of NRR catalysts due to its strong capacity to adsorb N_2, but Mo-N interaction is too strong and needs additional mediation. Iron (Fe) has been studied widely in the experiments, but the investigation of Fe-based bulk catalysts is very limited, due to the nature of Fe-N bonding. With respect to Mo, Fe-N bonding is weak, and once forming compounds, Fe is highly coordinated and Fe-N becomes too weak to activate N_2. Therefore, Fe with low coordination number is more suitable for NRR, like Fe-based SAC.

For SACs, the following elements have been studied widely, including Fe, Mo, B, W, Au, Ti, Al, N, V, Ni and Ru, as listed in Table 2. Among these designs, Ru and B show the best performance, with thermodynamic barriers as 0.42 eV (Ru/Boron sheet) and 0.31 eV (B/Graphene). For low-cost metals, Fe and Mo are promising, which are also the two metals contained in nitrogenases for NRR catalysis. For SACs, an important factor is the substrate,

which plays the key role to mediate the reactivity of single-atom active sites. So far, 2D materials have been widely employed to host SACs both computationally and experimentally. For catalyst design, 2D substrate can be modelled with slabs with small sizes, ideal for computational screening. Another merit is the relatively simple geometry of SACs and intermediate states on the substrate, providing reliable structure-performance relationship for catalyst designs.

Metal-free catalysts are emerged as a new direction in catalysts design over the last decade after its success for oxygen reduction reaction. For NRR, boron is particularly attractive due to its electron-deficient nature, which is helpful to accept electrons from nitrogen, performing similarly with transition metals. Therefore, both boron nanosheets and single-boron have been actively considered in recent years. So far, it seems that B-N_2 interaction is weak, but B-N bonding is strong; therefore, metal with strong capacity to fix N_2 may be an option to combine with boron and form dual active centres.

Table 1 Current bulk NRR catalysts by computational design.

Catalyst	Functional	Barrier (eV)	RDS
Boron Carbide Sheet[36]	PBE	0.34	NH_3
Boron Sheet[37]	PBE	1.30	NH_3
V_3C_2[38]	PBE	0.32	NH_3
$Ti_3C_2\,T_x$[39]	PBE	1.06	NH_3
Phosphorene[40]	PBE	0.85	N_2H^*
La_2O_3[41]	PBE	0.76	N_2H^*
MoC_6[42]	PBE	0.54	N_2H^*
MoC[43]	PBE	0.28	N_2H^*
Mo_2C[44]	PBE	1.02	N_2H^*
MoS_2[45]	PBE	0.68	N_2H^*
$Ti_3C_2T_x$[46]	PBE	0.64	N_2H^*
Boron Phosphide[47]	PBE	0.12	NH_3^*
Mo_2TiC_2[48]	PBE	0.26	NH_3^*
MoO_3[49]	PBE	2.25	N^*
MoO_2[50]	PBE	0.69	$NHNH^*$
MoN[51]	PBE	0.70	NH_2^*
Mo_2C[52]	PBE	N.A.	NH_2^*
Boron Sheet[53]	RPBE	0.77	N_2^*
VN[54]	RPBE	0.51	N_2H^*
VN[55]	RPBE	0.50	N_2H^*
CrN[56]	RPBE	0.68	N_2H^*
CoN[57]	RPBE	0.23	N_2H^*
MoS_2[58]	RPBE	0.64	N_2H^*
RuN[59]	RPBE	0.41	NH_3
$TiO_2/Ti_3C_2T_X$[60]	DMol	0.40	$N_2H_2^*$

Table 2 Current single-atom catalysts for NRR by computational design.

Catalyst	Functional	Barrier (eV)	RDS
N/Carbon[61]	PBE	0.70	$NHNH_2^*$
Fe@N$_3$/Graphene[62]	PBE	0.66	N_2H^*
Al/Graphene[63]	PBE	0.94	N_2H^*
W@N/Ggraphdiyne[64]	PBE	0.29	N_2H^*
Li-S/MoS$_2$[65]	PBE	0.42	N_2H^*
Fe/MoS$_2$[66]	PBE	1.02	N_2H^*
Mo/MoS$_2$[67]	PBE	0.53	N_2H^*
V/MoP[68]	PBE	0.69	N_2H^*
Mo/N$_3$-doped Graphene[69]	PBE	0.50	N_2H^*
Mo/Ti$_3$C$_2$O$_2$[70]	PBE	0.68	N_2H^*
V/Boron Sheet[71]	PBE	0.28	N_2H^*
B/Graphene[72]	PBE	0.43	NH_2^*
W/Graphene[73]	PBE	0.25	NH_2^*
Mo/N-doped Graphene[74]	PBE	0.47	NH_3
Fe@N$_3$-doped Graphene[75]	PBE	2.29	NH_3
Mo/C$_2$N[76]	PBE	0.17	NH_3
W/C$_3$N$_4$[77]	PBE	0.35	NH_3
Fe/Phosphorene[78]	PBE	2.34	NH_3
Ni/Graphene[79]	PBE	1.23	N^*
Ti/C$_3$N$_4$[80]	PBE	0.51	NH_3^*
B/C$_3$N$_4$[81]	PBE	0.20	NH_3^*
B/C$_2$N[82]	PBE	0.15	$NHNH^*$
Pt/C$_3$N$_4$[83]	PBE	0.24	$NHNH^*$
B/C$_2$N[84]	PBE	0.35	$NH_2NH_3^*$
Ru/TiO$_2$[85]	PBE	0.21	NH^*
Ti@N$_4$/Graphene[86]	RPBE	0.69	NH_3^*
B/Graphene[87]	RPBE	0.31	NH^*
B/C$_3$N$_4$[87]	RPBE	0.89	NH_3
Mo/C$_3$N$_4$[88]	RPBE	0.82	N_2H^*
Ru/Boron Sheet[89]	RPBE	0.42	N_2H^*
Mo/C$_3$N$_4$[88]	RPBE	0.82	N_2H^*
Mo@BC$_2$/Phosphorene[90]	RPBE	0.60	N_2H^*
Fe/MoN$_2$[91]	RPBE	0.47	N_2H^*

1.4 Project Outline

1.4.1 Project Objectives and Approaches

Based on the above literature review, this PhD project aims to design high performance catalysts for NRR. The central hypothesis is that novel catalysts can be identified from first principle calculations. Specifically, the following project objectives (POs) have been proposed:

PO1: To explore graphene-based metal-free catalysts. It will answer whether carbon can catalyse NRR, focusing on the effect of perfect graphene, defects, functional groups and dopants on NRR performance.

PO2: To explore 2D metal based materials (MoN_2, FeB_6 and Mo_2C) as NRR catalysts. Three 2D structures have been selected based on: (i) Mo-N, Fe-B and Mo-C bonding networks have been demonstrated as stable and highly conductive 2D structures; and (ii) Fe, Mo and B are also active for NRR.

PO3: To explore single-Mo NRR catalysts. Mo is an excellent element to fix N_2, but Mo-N bonding needs to be mediated. Systematically searching of various ligands (L) combinations will be performed in this program to identify an optimum Mo-L system for NRR catalysis.

PO4: To establish criteria for computer-aided design of NRR catalysts. Based on a series of cases studied in PO1-PO3, the basic principles for rational designs of NRR catalysts will be examined, towards the establishment of an advanced design strategy.

To achieve the above POs, concept catalysts will be proposed and examined by DFT-based calculations, using the following protocols:

(i) Computational setting: DFT-based calculations with RPBE functional, as embedded in VASP [94-95]. All energies will be corrected with a full consideration of zero-point energy and van der Waals interaction under the DFT-D3 scheme [96]. Cutoff energy and k-points will be determined based on the supercell sizes and catalyst components. All work will be performed using National Computational Infrastructure at Canberra.

(ii) Catalyst evaluation: Full energy files (ΔG_i) for these catalysts will be calculated, using the scheme of standard hydrogen electrode [97] to treat the free energy of ($H^+ + e^-$) couple. When ΔG_{max} for NRR is less than 0.60 eV, such catalyst has been recommended as promising candidate in terms of thermodynamics. A further investigation of HER will be performed to examine the selectivity, with $\Delta G_{max}(NRR) < \Delta G_{max}(HER)$ as the selectivity criteria.

1.4.2 Thesis Structures

This thesis has seven chapters, being organized as:

Chapter 1: Introduction

Chapter 2: Insight into the Reactivity of Carbon Structures for Nitrogen Reduction Reaction;

Chapter 3: Computational Study of MoN_2 Monolayer as Electrochemical Catalysts for Nitrogen Reduction;

Chapter 4: Exploration of iron borides as electrochemical catalysts for nitrogen reduction reaction;

Chapter 5: Impact of H-termination on the nitrogen reduction reaction of molybdenum carbide as an electrochemical catalyst;

Chapter 6: Computational Design of Single-Molybdenum Catalysts for the Nitrogen Reduction Reaction;

Chapter 7: Summaries, Perspective and Future work.

These chapters are presented based on published journal papers (Chapters 3, 5, 6) or submitted manuscripts (Chapters 2, 4). Chapter 2 is to achieve PO1, Chapters 3-5 for PO2, Chapter 6 for PO3 and Chapter 7 for PO4.

1.5 References

[1]   Raccuglia, P.; Elbert, K. C.; Adler, P. D. F.; Falk, C.; Wenny, M. B.; Mollo, A.; Zeller, M.; Friedler, S. A.; Schrier, J.; Norquist, A. J. *Nature* **2016,** 533, 73.

[2]   Nørskov, J. K.; Abild-Pedersen, F.; Studt, F.; Bligaard, T. *PNAS USA* **2011,** 108, 937.

[3]   Smil, V. *Nature* **1999,** 415, 400.

[4]   Smil, V. Enriching the earth: Fritz Haber, Carl Bosch, and the Transformation of World Food Production, Massachusetts Institute of Technology. **2001.**

[5]   Haber, F.; Van, G. *Anorg. Chem.* **1905,** 47, 42.

[6]   Ertl, G. *Catal. Rev.* **1980,** 21, 201.

[7]   Erisman, J. W.; Sutton, M. A.; Galloway, J.; Klimont, Z.; Winiwarter, W. *Nature Geoscience* **2008,** 1, 636.

[8]   Luo, Y. R. Comprehensive Handbook of Chemical Bond Energies, Boca Raton, FL, *CRC Press*, **2007.**

[9]   Azofra, L. M.; MacFarlane, N. Li, D.; Sun, C. *Energ. Environ. Sci.* **2016,** 9, 2545.

[10]   Dos Santos, P.C.; Igarashi, R. Y.; Lee, H. I.; Hoffman, R. M.; Seefeldt, L. C.; Dean, D.R. *Acc. Chem. Res.* **2005,** 38, 208.

[11]   Burgess, B. K.; Lowe, D. J. *Chem. Rev.* **1996,** 96, 2983.

[12]   Hoffman, B. M.; Dean, D. R.; Seefeldt, L. C. *Chem. Rev.* **2009,** 42, 609.

[13]   McWilliams, S. F.; Holland, P. L. *Acc. Chem. Res.* **2015,** 48, 2059.

[14]   Hoffman, B. M.; Lukoyanov, D.; Yang, Z. Y.; Dean, D. R.; Seefeldt, L. C. *Chem. Rev.* **2014,** 114, 4041.

[15]   Liu, H. Z. Ammonia synthesis catalysts: Innovation and practice. Chemical Industry Press, Beijing **2013**.

[16]   Burford, R. J.; Yeo, A.; Fryzuk, M. D. *Coord Chem. Rev.* **2017,** 334, 84.

[17]   MacLeod, K. C.; McWilliams, S. F.; Mercado, B. Q.; Holland, P. L. *Chem. Sci.* **2016**, 7, 5736.

[18]   Honkala, K.; Hellman, A.; Remediakis, I. N.; Logadottir, A.; Carlsson, A.; Dahl, S.; Christensen, C. H.; Nørskov, J. K. *Science* **2005,** 307, 555.

[19]   Haber, F. Nobel Prize Lecture 1918, in Nobel Lectures, Chemistry 1901–1921 (Elsevier, Amsterdam, **1966**).

[20]   Mittasch, A. *Adv. Catal.* **1950,** 2, 81.

[21]   Logadottir, A.; Nørskov, J. K. *J. Catal.* **2003,** 220, 273.

[22]   Bowker, M. *Top Catal.* **1994,** 1, 165.

[23] Wang, B. H.; Liu, R. Q.; Wang, J. D.; Li, Z. J.; Xie, Y. H. *Chin. J. Inorg Chem* **2005,** 21, 1551.

[24] Liu, R. Q.; Xie, Y. H.; Wang, J. D.; Li, Z. J.; Wang, B. H. *Solid State Ionics* **2006,** 177, 73.

[25] Chen, C.; Ma, G. *J. Alloy Comp.* **2009,** 485, 69.

[26] Amar, I. A.; Lan, R.; Petit, C. T. G.; Tao, S. *Int. J. Electrochem. Sci*. **2015**, 10, 3757.

[27] Kyriakou, V.; Garagounis, I.; Vasileiou, E.; Vourros, A.; Stoukides, M. *Catal. Today* **2017**, 286, 2.

[28] Murakami, T.; Nishikiori, T.; Nohira, T.; Ito, Y. *J. Electrochem. Soc.* **2005,** 152, D75.

[29] Xu, G. C.; Liu, R. Q.; Wang, J. *Sci. China Ser. B* **2009,** 52, 1171.

[30] Yoo, J. S.; Christensen, R.; Vegge, T.; Nøskov, J. K.; Studt, F. *ChemSusChem* **2016,** 9, 358.

[31] Greeley, J. *Annu. Rev. Chem. Biomol. Eng.* **2016,** 7, 605.

[32] Montoya, J. H.; Tsai, C.; Vojvodic, A.; Nøskov, J. K. *ChemSusChem* **2015,** 8, 2180.

[33] Dai, V.; Xue, Y.; Qu, L.; Choi, H. J.; Baek, J. B. *Chem. Rev*. **2015,** 115, 4823.

[34] Yang, Z.; Ren, J.; Zhang, Z.; Chen, X.; Guan, G.; Qiu, L.; Zhang, Y.; Peng, H. *Chem. Rev.* **2015,** 115, 5159.

[35] Machado, B.F.; Serp, P. *Catal. Sci. Technol.* **2012,** 2, 54.

[36] Qiu, W.; Xie, X. Y.; Qiu, J.; Fang, W. H.; Liang, R.; Ren, X.; Ji, X.; Cui, G.; Asiri, A. M.; Cui, G.; Tang, B.; Sun, X. P. *Nature. Commun.* **2018,** 9, 3485.

[37] Zhang, X.; Wu, T.; Wang, H.; Zhao, R.; Chen, H.; Wang, T.; Wei, P.; Luo, Y.; Zhang, Y.; Sun, X. *ACS Catal.* **2019,** 9, 4609.

[38] Azofra, L. M.; Li, N.; MacFarlane, D. R.; Sun, C. *Energ. Environ. Sci.* **2016,** 9, 2545.

[39] Zhao, J.; Zhang, L.; Xie, X. Y.; Li, X.; Ma, Y.; Liu, Q.; Fang, W. H.; Shi, X.; Cui, G.; Sun, X. *J. Mater. Chem. A* **2018,** 6, 24031.

[40] Zhang, L.; Ding, L. X.; Chen, G. F.; Yang, X.; Wang, H. *Angew. Chem. Int. Ed.* **2019,** 58, 2612.

[41] Xu, B.; Liu, Z.; Qiu, W.; Liu, Q.; Sun, X.; Cui, G.; Wu, Y.; Xiong, X. *Electrochimica Acta* **2019,** 298, 106.

[42] Chen, Z. W.; Lang, X. Y.; Jiang, Q. *J. Mater. Chem. A* **2018,** 6, 9623.

[43] Matanovic, I.; Garzon, F. H. *Phys. Chem. Chem. Phys.* **2018,** 20, 14679.

[44] Li, Q.; Qiu, S.; He, L.; Zhang, X.; Sun, C. *Phys. Chem. Chem. Phy.* **2018,** 20, 23338.

[45] Zhang, L.; Ji, X.; Ren, X.; Ma, Y.; Shi, X.; Tian, Z.; Asiri, A. M.; Chen, L.; Tang, B.; Sun, X. *Adv. Mater.* **2018,** 30, 1800191.

[46] Luo, Y.; Chen, G. F.; Ding, L.; Chen, X.; Ding, L. X.; Wang, H. *Joule* **2019,** 3, 279.

[47] Chen, Z.; Zhao, J.; Yin, L.; Chen, Z. *J. Mater. Chem. A* **2019**, 7, 13284.

[48] Gao, Y.; Cao, Y.; Zhuo, H.; Sun, X.; Gu, Y.; Zhuang, G.; Deng, S.; Zhong, X.; Wei, Z.; Li, X.; Wang, J. *Catal. Today* **2018**.

[49] Han, J.; Ji, X.; Ren, X.; Cui, G.; Li, L.; Xie, F.; Wang, H.; Li, B.; Sun, X. *J. Mater. Chem. A* **2018,** 6, 12974.

[50] Zhang, G.; Ji, Q.; Zhang, K.; Chen, Y.; Li, Z.; Liu, H.; Li, J.; Qu, J. *Nano Energy* **2019,** 59, 10.

[51] Matanović, I.; Garzon, F. H.; Henson, N. J. *Phys. Chem. Chem. Phys.* **2014,** 16, 3014.

[52] Shao, M.; Shao, Y.; Chen, W.; Ao, K. L.; Tong, R.; Zhu, Q.; Chan, I. N.; Ip, W. F.; Shi, X.; Pan, H. *Phys. Chem. Chem. Phys.* **2018,** 20, 14504.

[53] Liu, C.; Li, Q.; Zhang, J.; Jin, Y.; MacFarlane, D. R.; Sun, C. *J. Phys. Chem. C* **2018,** 122, 25268.

[54] Abghoui, Y.; Garden, A. L.; Hlynsson, V. F.; Björgvinsdóttir, S.; Ólafsdóttir, H.; Skúlason, E. *Phys. Chem. Chem. Phys.* **2015,** 17, 4909.

[55] Abghoui, Y.; Garden, A. L.; Howalt, J. G.; Vegge, T.; Skúlason, E. *ACS Catal.* **2016,** 6, 635.

[56] Abghoui, Y.; Skúlason, E. *Catal. Today* **2017,** 286, 69.

[57] Abghoui, Y.; Skúlason, E. *J. Phys. Chem. C* **2017,** 121, 6141.

[58] Suryanto, B. H. R.; Wang, D.; Azofra, L. M.; Harb, M.; Cavallo, L.; Jalili, R.; Mitchell, D. R. G.; Chatti, M.; MacFarlane, D. R. *ACS Energy Lett.* **2019,** 4, 430.

[59] Abghoui, Y.; Skúlasson, E. *Procedia Computer Science* **2015,** 51, 1897.

[60] Fang, Y.; Liu, Z.; Han, J.; Jin, Z.; Han, Y.; Wang, F.; Niu, Y.; Wu, Y.; Xu, Y. *Adv. Energy Mater.* **2019,** 9, 1803406.

[61] Liu, Y.; Su, Y.; Quan, X.; Fan, X.; Chen, S.; Yu, H.; Zhao, H.; Zhang, Y.; Zhao, J. *ACS Catal.* **2018,** 8, 1186.

[62] Guo, X.; Huang, S. *Electrochimica Acta* **2018,** *284*, 392.

[63] Tian, Y. H.; Hu, S.; Sheng, X.; Duan, Y.; Jakowski, J.; Sumpter, B. G.; Huang, J. *J. Phys. Chem. Lett.* **2018,** 9, 570.

[64] He, T.; Matta, S. K.; Du, A. *Phy. Chem. Chem. Phys.* **2019,** 21, 1546.

[65] Liu, Y.; Han, M.; Xiong, Q.; Zhang, S.; Zhao, C.; Gong, W.; Wang, G.; Zhang, H.; Zhao, H. *Adv. Energy Mater.* **2019,** 9, 1803935.

[66] Azofra, L. M.; Sun, C.; Cavallo, L.; MacFarlane, D. R. *Chem.-Eur. J* **2017,** 23, 8275.

[67] Zhao, J.; Zhao, J.; Cai, Q. *Phys. Chem. Chem. Phys.* **2018,** 20, 9248.

[68] Han, M.; Wang, G.; Zhang, H.; Zhao, H. *Phys. Chem. Chem. Phys.* **2019,** 21, 5950.

[69] Zhao, W.; Zhang, L.; Luo, Q.; Hu, Z.; Zhang, W.; Smith, S.; Yang, J. *ACS Catal.* **2019,** 9, 3419.

[70] Gao, Y.; Zhuo, H.; Cao, Y.; Sun, X.; Zhuang, G.; Deng, S.; Zhong, X.; Wei, Z.; Wang, J. *Chin. J. Catal.* **2019,** 40, 152.

[71] Zhu, H. R.; Hu, Y. L.; Wei, S. H.; Hua, D. Y. *J. Phys. Chem. C* **2019,** 123, 4274.

[72] Yu, X.; Han, P.; Wei, Z.; Huang, L.; Gu, Z.; Peng, S.; Ma, J.; Zheng, G. *Joule* **2018,** 2, 1610.

[73] Ling, C.; Ouyang, Y.; Li, Q.; Bai, X.; Mao, X.; Du, A.; Wang, J. *Small Methods* **2019**, 0, 1800376.

[74] Ling, C.; Bai, X.; Ouyang, Y.; Du, A.; Wang, J. *J. Phys. Chem. C* **2018,** 122, 16842.

[75] Li, X. F.; Li, Q. K.; Cheng, J.; Liu, L.; Yan, Q.; Wu, Y.; Zhang, X. H.; Wang, Z. Y.; Qiu, Q.; Luo, Y. *J. Am. Chem. Soc.* **2016,** 138, 8706.

[76] Wang, Z.; Yu, Z.; Zhao, J. *Phys. Chem. Chem. Phys.* **2018,** 20, 12835.

[77] Chen, Z.; Zhao, J.; Cabrera, C. R.; Chen, Z. *Small Methods* **2019**, 0, 1800368.

[78] Wei, Z.; Zhang, Y.; Wang, S.; Wang, C.; Ma, J. *J. Mater. Chem. A* **2018,** 6, 13790.

[79] Yang, T.; Tang, S.; Li, X.; Sharman, E.; Jiang, J.; Luo, Y. *J. Phys. Chem. C* **2018,** *122* (44), 25441.

[80] Chen, X.; Zhao, X.; Kong, Z.; Ong, W. J.; Li, N. *J. Mater. Chem. A* **2018,** 6, 21941.

[81] Ling, C.; Niu, X.; Li, Q.; Du, A.; Wang, J. *J. Am. Chem. Soc.* **2018,** 140, 14161.

[82] Ji, S.; Wang, Z.; Zhao, J. *J. Mater. Chem. A* **2019,** 7, 2392.

[83] Yin, H.; Li, S. L.; Gan, L. Y.; Wang, P. *J. Mater. Chem. A* **2019,** 7, 11908.

[84] Cao, Y. Y.; Deng, S. W.; Fang, Q. J.; Sun, X.; Zhao, C. X.; Zheng, J. N.; Gao, Y. J.; Zhou, H.; Li, Y. J.; Yao, Z. H. *Nanotechnology* **2019**, 33, 33.

[85] Cheng, S.; Gao, Y. J.; Yan, Y. L.; Gao, X.; Zhang, S. H.; Zhuang, G. L.; Deng, S. W.; Wei, Z. Z.; Zhong, X.; Wang, J. G. *J. Energy Chem.* **2019,** 39, 144.

[86] Choi, C.; Back, S.; Kim, N. Y.; Lim, J.; Kim, Y. H.; Jung, Y. *ACS Catal.* **2018,** 8, 7517.

[87] Liu, C.; Li, Q.; Wu, C.; Zhang, J.; Jin, Y.; MacFarlane, D. R.; Sun, C. *J. Am. Chem. Soc.* **2019,** 141, 2884.

[88] Zhang, L.; Zhao, W.; Zhang, W.; Chen, J.; Hu, Z. *Nano Research* **2019,** 12, 1181.

[89] Liu, C.; Li, Q.; Zhang, J.; Jin, Y.; MacFarlane, D. R.; Sun, C. *J. Mater. Chem. A* **2019,** 7, 4771.

[90] Li, Q.; Qiu, S.; Liu, C.; Liu, M.; He, L.; Zhang, X.; Sun, C. *J. Phys. Chem. C* **2019,** 123, 2347.

[91] Li, Q.; He, L.; Sun, C.; Zhang, X. *J. Phys. Chem. C* **2017,** 121, 27563.

[92] Honkala, K.; Hellman, A.; Remediakis, I. N.; Logadottir, A.; Carlsson, A.; Dahl, S.; Christensen, C. H.; Nørskov J. K. *Science* **2005,** 307, 555.

[93] Nie, X.; Esopi, M. R.; Janik, M. J.; Asthagiri, A. *Angew. Chem. Int. Ed.* **2013,** 52, 2459.

[94] Perdew, J. P.; Burke, K.; Ernzerhof, M. *Phys. Rev. Lett.* **1996,** 77, 3865.

[95] Kresse, G.; Joubert, D. *Phys. Rev. B* **1999,** 59, 1758.

[96] Grimme, S.; Antony, J.; Ehrlich, S.; Kerieg, H. *Chem. Phys*. **2010,** 132, 154104.

[97] Skúlason, E.; Bligaard, T.; Gudmundsdóttir, S.; Studt, F.; Rossmeisl, J.; Abild-Pedersen, F.; Vegge, T.; Jónssonac, H.; Nørskov, J. K. *Phys. Chem. Chem. Phys.* **2012,** 14, 1235.

Chapter 2 Graphene-based NRR Catalyst

2.1 Overview

Graphene, as the most extensively studied 2D material, has been widely employed as catalysts and catalyst supports for various electrochemical reactions. This chapter aims to explore its catalysis performance for NRR, focusing on three key questions: (i) does graphene work for NRR; (ii) if yes, what is the active site; and (iii) how it catalyses NRR.

In the literature, several groups reported that carbon structures, especially graphene and porous carbon, can offer promising performance for NRR, but the origin for such observations has not been clarified. Defects, dopants and functional groups have been proposed as active sites, which is still debated. In this PhD work, systematic calculations of 20 graphene-based structures have been performed, focusing on the effect of these proposed structures on NRR. It is found that graphene can catalyse NRR, but active sites come from lowly coordinated carbon, which may be introduced by the structural evolution of defects, functional groups or dopants during NRR process.

This work has been submitted to *ACS Catalysis*.

Insight into the Reactivity of Carbon Structures for Nitrogen Reduction Reaction

Qinye Li,[a] Siyao Qiu,[b] Chuangwei Liu,[c] Fengling Zhou,[b] Lizhong He,[a] Xiwang Zhang,[*,a] Chenghua Sun[*,d]

[a] School of Chemical Engineering, Monash University, Clayton, Victoria 3800, Australia

[b] Science & Technology Innovation Institute, Dongguan University of Technology, Dongguan 523808, China

[c] School of Chemistry, Monash University, Clayton, Victoria 3800, Australia

[d] Department of Chemistry and Biotechnology, Center for Translational Atomaterials, Faculty of Science, Engineering & Technology, Swinburne University of Technology, Hawthorn, VIC 3122, Australia

Supporting Information Placeholder

ABSTRACT: Graphene-based structures have been widely reported as promising metal-free catalysts for nitrogen reduction reaction (NRR). To explain the reactivity origin, various structures have been proposed and debated, including defects, functional groups and doped heteroatoms. This computational work demonstrates that these structures may evolute from one to another under electrochemical conditions, generating lowly coordinated carbons, which have been identified as the active sites for N_2 adsorption and activation.

Introduction

Ammonia (NH_3), as the basis of modern agriculture and chemical engineering, is one of the most highly produced inorganic chemicals.[1-3] Industrial ammonia production is dominated by the famous Haber-Bosch process at high temperature and high pressure,[4] consuming ~1.5% of global energy and producing ~1% of carbon emissions.[4,5] In this context, electrochemical synthesis has been proposed as a green technology to produce ammonia.[6-12]

To activate and convert N_2 to NH_3 under electrochemical conditions, high performance NRR catalysts are essential. So far, catalyst searching focuses on metal-based catalysts, like compounds[13-17] and single-atom catalysts[18-26], but the performance is still far from satisfaction[27], underlining the need for novel catalyst design. Carbon structures, as metal-free catalysts, has been extensively tested and demonstrated as promising NRR catalysts in recent years.[28-40] For instance, Li-incorporated poly(N-ethyl-benzene-1,2,4,5-tetra-carboxylic diimide) has been tested, leading to an yield of 2 μg h^{-1} cm^{-2} and Faraday efficiency FE=3%, in which [O-Li$^+$] has been proposed as active NRR site. Later, a series of heteroatom-doped structures have been reported, including S-doped carbon nanospheres (S-CNS), N-doped graphene (NG) and porous carbon, O-doped graphene (OG) and hollow carbon (O-HC), S-doped graphene (SG), N-S codoped graphene (NSG), with typical yield of 10-30 μg h^{-1} mg^{-2} cat., and heteroatoms and their neighboring carbon are believed to dominate the reaction performance. Functional groups have also been proposed as potential active sites, such as N-containing groups (N-g) in polyaniline, pyridinic-N in alfalfa-derived carbon and MOF-derived N_4-site embedded in the graphene plane. While N-free carbon has also been reported as active NRR catalysts, in which oxygen-containing groups (O-g) and defective graphene (DG) are often proposed as the reactivity origin (see Table S1, supporting information). Clearly, the performance origin of these carbon structures has not been fully understood.

So far, N- and O-containing functional groups (N-g, O-g), doped heteroatoms and defects have been proposed as active sites. It is possible that these structures play key roles for NRR in specific samples determined by the synthesis process, but it is worth to ask: (i) whether pure carbon, like vacancies and topological defects, can catalyze NRR; (ii) if not, is there any connections between these active sties under electrochemical conditions; and (iii) is there a general mechanism to explain observed experimental data. These questions are proposed because it not only helps accurate measurements and understanding of existing NRR data, but also guides the further improvement. For instance, N-containing groups may release NH_3 as concerned widely;[41-43] therefore, it is highly necessary to verify whether N is solely contributed from N_2, rather than fully or partially from catalysts. But experimental identification is very challenging, which requires quantitative determination of various defects and functional groups. Even all these information can be accurately collected, it is hard to decouple their effects on electrochemical processes. Therefore, a systematic computational investigation has been employed in this work, aiming to clarify the effect of these proposed active sites on NRR and deliver an insight into the reactivity of carbon-based catalysts.

Our strategy is to investigate NRR over a series of active sites and compare their performance with each other. Particularly, this work focuses on the evolution of defects and functional groups. For this purpose, the investigation was performed with three levels, including primary screening of 15 carbon structures, studying NRR without N-contribution from catalysts and NRR with functional groups evolutions. As demonstrated below, structural evolution can occur between defects and functional groups, generating lowly coordinated carbon (LCC), which is active to adsorb and activate N_2, offering similar or even better performance than transition metals in NRR. Because LCC is very active and may be terminated by hydrogen, a potential stabilization mechanism electrolyte based on LCC-electrolyte interactions has been explored as well.

2 Computational Methods

Spin-polarized calculations were carried out based on standard density functional theory, under the generalized gradient approximation with the revised Perdew-Burke-Ernzerhof.[44,45] An energy cut-off of 380 eV was employed, together with k-space being sampled with a Monkhorst-Pack grid of 3×3×1. All structures have been fully relaxed until the maximum force on each atom was less than -0.02 eV/Å and energy change less than 10^{-4} eV. Zero point energy corrections were calculated over gamma points. The van der Waals interaction has been considered using the DFT-D3 scheme.[46]

NRR has been studied through calculating the free energy change (ΔG) for each elementary step, as summarized in the literature.[47-51] At the beginning, 15 catalysts with different active sites, as listed in Scheme 1, have been scanned using the adsorption energies of N_2 and N as the indicators.[50-52] Starting from perfect graphene (G), topologic defects (5775, 585) and single carbon vacancy have been introduced, showing as G5775, G585 and GV. To examine the reactivity of sp³-hybridized carbon, (111) surface of diamond crystal has been built as a slab, as D111. Heteroatoms (F, S, N, O) are doped or co-doped to graphene, as FG, SG, NG, OG and NSG, respectively. Pore terminated by -CH, -C≡N, N-groups and O-groups has been modelled and shown as Pore, CN, N-g, and O-g in Scheme 1. Carbon nanotube (6, 6), labelled as NT66, has been employed to study the curvature effect. All these models are fully optimized before considering N_2 adsorption and NRR. Promising sites are then investigated through calculating full energy profile for further evaluation. To evaluate the evolution of functional groups, cluster models containing N- and O-groups have been employed. Coupled proton and electron have been introduced to the system as the hydrogen resource to reduce N_2 or added to functional groups using standard hydrogen electrode as the reference, as well described in the literature.[51] For LCC stabilization, single sodium ion (Na^+) has been introduced to local active sties (carbon cluster), followed with full optimization without considering the solvation effect.
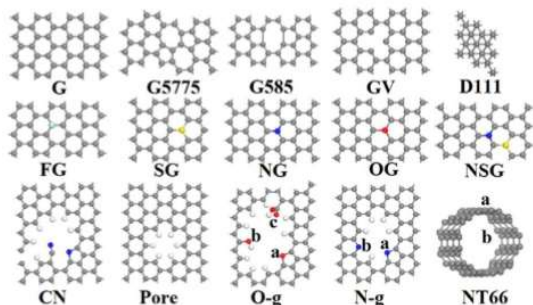
Scheme 1. Proposed models for studying N_2 adsorption. C, O, F, N, H, and S are shown as gray, red, cyan, blue, white and yellow spheres. Different adsorption sites are labelled as a, b and c.

3 Results and Discussion

3.1 NRR without N-contribution from catalysts

N_2 has very low solubility in water and thus effective N_2-adsorption is critical for NRR.[53] The calculated adsorption energy $AE(N_2^*)$ for the models listed in Scheme 1 is in the range of -0.1 eV to -0.5 eV (see supporting information, Fig. S1), indicating that these are typical physical adsorptions. This can be further supported by the calculated distance between N_2 and catalyst, N-N bond length and net charges on adsorbed N_2, as shown in Fig. 1 for six candidates, according to which three features can be summarized (Fig. 1(a)): (i) N_2-catalyst distance is more than 3.0 Å; (ii) N-

N bond length (~1.12 Å) is close to that of gas-phase N_2[54]; and (iii) N_2 is almost neutral. It is clear that N_2 is physically adsorbed.

Fig. 1(b) shows the calculated charge density for G, SG, NG, Pore, CN and GV (see Scheme 1). Using perfect graphene as a reference, major changes associated with dopants and defects are highlighted by red triangles, where N_2 favors the adsorption. As discussed in the literature,[55-57] defects and heteroatoms can result in local charge polarization and deviations from perfect sp² hybridization, which is beneficial for N_2 adsorption. For perfect graphene, both electron accepting and donating impair the conjugated π-bonding system, demanding large energy input. As a result, physical adsorption is favourable, and N_2 activation is very difficult. For non-perfect graphene, however, dopants, defects and functional groups can break the high symmetry and introduce electron-rich and/or deficient regions. Such change is particularly remarkable for Pore, CN and GV, as shown in Fig. 1(b). It is worth to further check the difference between these structures. For Pore, local electronics is dominated by C-H bonding, which is very strong and can hardly break at mild conditions. While C≡N and LCC contained in CN and GV are active, both of which may be involved in following reactions. Moreover, N-groups (like CN) are different from GV as they can be hydrogenated to release NH_3, while LCC may be terminated by hydrogen to form stable C-H bonds, which will passivate these sites. Therefore, it is highly essential to further examine whether such newly introduced active sites can adsorb and activate N_2, as demanded for full NRR.

Generally, the performance of NRR catalysts can be indicated by the adsorption energy of N-atom $AE(N^*)$.[50-52] Fig. 1(c) presents calculated AE for those active sites shown in Scheme 1. Using Ru(0001) as a reference (AE=-0.46 eV, red line in Fig. 1(c)), catalysts with similar AE are often expected to offer high NRR performance, according to which GV is the only candidate promising for NRR. To understand it, optimized geometries of single N adsorbed on six active sties (G, D111, GV, OG, SG, NSG) have been shown in Fig. 1(d), in which GV is different from the other five with LCC being presented, as highlighted by green circles. In fact, GV, among the five candidates in Scheme 1, is the only structure showing LCC. To further confirm that full NRR can occur over GV, free energy change ΔG for elementary steps has been calculated, as listed in Table S2, together with several other candidates without LCC. The calculated maximum ΔG, labelled as ΔG_{max}, has been employed to evaluate the limiting potential to drive the reaction, as presented in Fig. 1(e). Five of them show large ΔG_{max} (>2.0 eV), which comes from initial N_2 reduction ($N_2 \rightarrow N_2H$, see Table S2), confirming poor activation of N_2. While GV shows totally different reactivity, with ΔG_{max}=1.21 eV, as the best candidate among them. This striking difference underlines the importance of LCC.

Another evidence comes from the adsorption energy of N, $BE(N^*)$, presented in Fig. 1(c). GV is the only candidate with negative $BE(N^*)$, indicating that N-adsorption can remarkably stabilize LCC given $BE(N^*)$ is calculated with gas-phase N_2 as the energy reference. To clarify this, optimized geometries and highest occupied molecular orbitals (HOMO) for GV and GV-N have been collected in Fig. S2, with LCC atoms are labelled as C1, C2 and C3. The dangling bond can be vividly seen from HOMO and HOMO-1, which are active. In addition, the distance between LCC atoms is as large as 2.36 Å, being too large to form stable C-C bonds. With N-adsorption, C1-N bond (1.27 Å) is generated as a typical double bond[54] and C1 is saturated. At the same time, σ bond is generated between C2 and C3, but bond length (1.85 Å) is large. Associated with this bonding network, HOMO is dominated by C1-N π* feature centred at N site, while HOMO-1 is typical C2-C3 σ-bonding. Overall, it is concluded that GV is highly active due to LCC-associated dangling bond, which has been partially stabilized due to N-adsorption. Newly resulted C1-N π* (HOMO) and C2-C3 σ-bond (HOMO-1) may be further involved in following NRR steps.
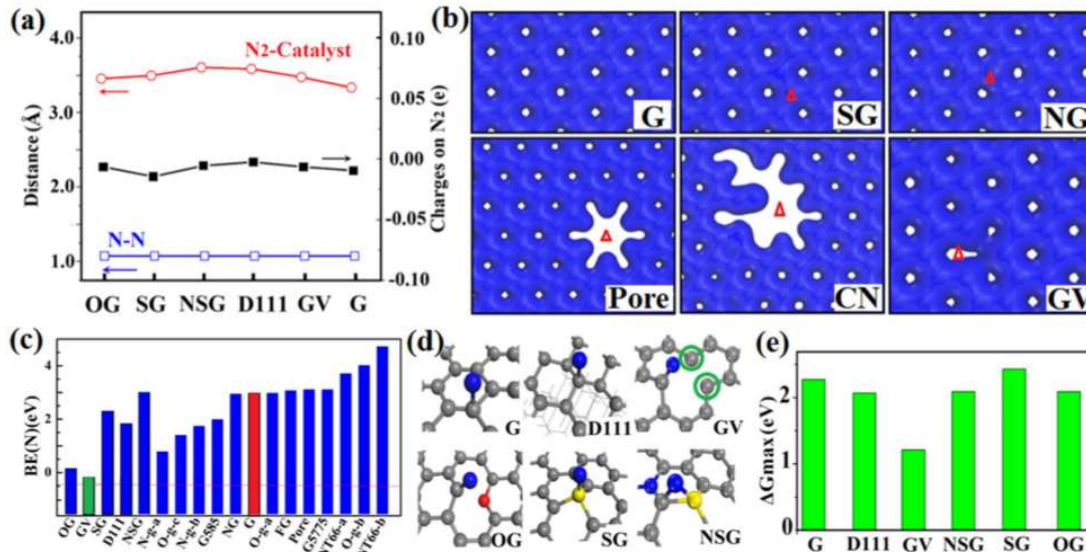
Figure 1. Primary evaluation of NRR performance. (a) N_2-catalyst distance, N-N bond length, and net charges for N_2 adsorbed on selected candidates; (b) Calculated charge density for G, SG, NG, Pore, CN and GV (isovalue=0.2); (c) Calculated BE(N*), with red line indicating the reference Ru(0001) with AE=-0.46 eV; (d) Optimized geometries of N* on six candidates; (e) Calculated ΔG_{max} in unit of eV for six selected candidates. Active sites (a, b, c) are shown in Scheme 1. C, N, O, and S in (b) are shown as grey, blue, red and yellow spheres. LCCs are highlighted by green circles in (d).
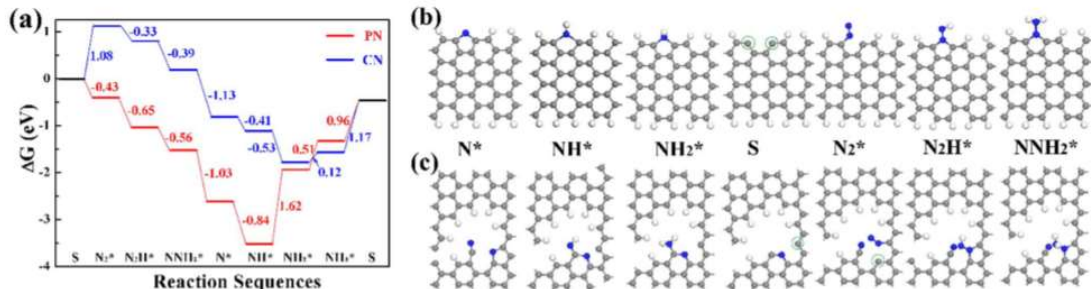
3.2 NRR with N-contribution from Catalysts

For N-containing groups, there is another path to be involved in NRR – they can directly contribute as N-resource to release NH_3, like amine, $-NH_2^* + (H^+ + e^-) \rightarrow NH_3$. In fact, such N-contribution may overestimate the performance of NRR catalysts, and ^{15}N isotope validation is recommended for NRR tests.[41-43] Particularly, such NH_3 production does not have to get over the barrier for N≡N activation; therefore, its reaction rate may be much higher than that for full N_2 reduction. When it is unsustainable, poor durability and low FE will be resulted because proton and electrons may be consumed to terminate LCC on residual fragments. While, when N_2 can be effectively fixed to the residual fragments after releasing NH_3, these N-groups may be regenerated with full nitrogen reduction. Therefore, the key is their regenerations to complete full NRR, rather than whether or not N-groups are involved.

Following above analysis, two specific N-groups, namely nitrile (CN) and pyridine (PN), have been selected from Scheme 1 to explore full NRR with N-contribution from catalysts. Starting with N embedded in catalyst, hydrogen has been introduced to form NH* and NH_2^*, and further H-adding will release NH_3 with N-vacancy generated, which will be filled with one nitrogen from N_2 adsorption, leaving another nitrogen as active site for more H-adding, until the release of second NH_3. The calculated free energy profiles and intermediate states for the above reactions over CN and PN have been shown in Fig. 2, from which ΔG_{max} has been derived as 1.17 eV and 1.65 eV for nitrile and pyridine groups, respectively, being close to that of GV (1.21 eV) and much better than the others. In our description for the reaction sequence, the state before N_2 adsorption is set as S, followed by six elementary steps associated with full NRR, generating N_2^*, N_2H^*, NNH_2^*, N* (original structure with N-groups), NH*, NH_2^*, as labelled in Fig. 2. Clearly, N_2 has been adsorbed and activated by LCC contained in S state, as highlighted by green circles in Fig. 2(b) and (c). Using ΔG_{max} as an indicator, the overall performance is close or even better than typical transition metals.[51] Therefore, N-groups can catalyse full NRR without large energy cost.

It is particularly worth to find out the common features between these two promising catalysts (nitrile and pyridine groups), as these would help us to establish a general understanding of the performance. Based on the intermediate states, the whole process can be split as two stages, namely N-group evolution and N_2 reduction, corresponding to the steps from N* to S and from S to NNH_2^* in Fig. 3, respectively. When NH_3 is released from NNH_2^* state, N-groups are regenerated as N* state. Therefore, this process is sustainable, but N-exchange occurs between adsorbed N_2 and initial nitrogen contained in the catalyst.

Another interesting phenomenon is the generation of LCC, which is not only active to fix N_2, but also activate N≡N effectively because the initial reduction from N_2^* to N_2H^* is not the PDS any more, with ΔG=-0.33 eV and -0.65 eV for nitrile and pyridine, respectively. Both of them are spontaneous, making it attractive as such step often results in large barrier in the case of metal-based catalysts.[51,58-60] Between CN and PN, they also perform differently as reflected by the calculated ΔG for elementary steps (see Fig. 3(a)), with PN offering better capacity to adsorb N_2 than GV and CN. This indicates a potential opportunity to optimize the functional groups to achieve better performance. From the above discussion, it is highly likely that LCC is the origin for the NRR reactivity for these carbon structures. But whether such evolution mechanism is applicable to other N-groups or even O-groups should be examined. Two key questions need to be answered: (i) whether LCC can be generated generally, and (ii) whether LCC has the capacity to catalyse full NRR, including N_2 adsorption, activation and reduction. In addition, it is necessary to confirm that O-groups will perform similarly with N-groups.

Figure 2. NRR with N-contribution from catalysts. (a) Calculated free energy profile for PN and CN and (b)&(c) intermediate states involved with for full NRR over nitrile (CN) and pyridine (PN) groups.
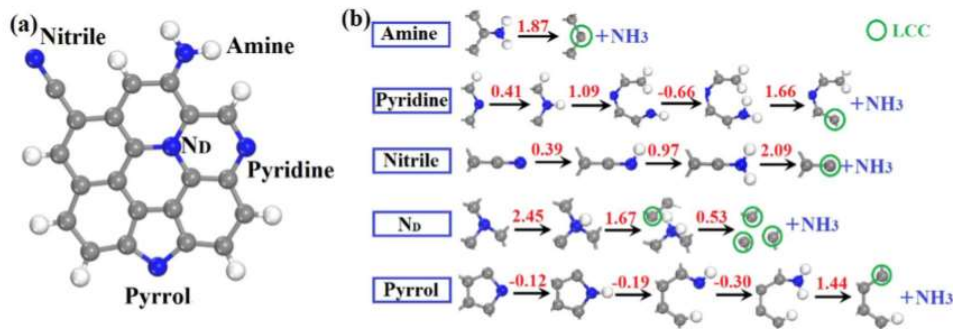
3.3 Evolution of N- and O-Groups

Following above investigation, we further examine the evolutions of other N-containing groups, aiming to examine whether LCC mechanism is applicable generally. To make a reliable comparison between these groups, a cluster model with five N-groups (amine, pyridine, nitrile, doped nitrogen N_D, and pyrrol group) has been employed, as shown in Fig. 3(a). Based on the strategy described in Section 3.2, the evolution has been explored through adding coupled proton and electron to these functional groups towards NH_3 production. The key structure changes associated with the evolution of these N-groups have been shown in Fig. 3(b), together with calculated ΔG for each step in unit of eV, according to which we found that (i) LCC has been frequently generated, as highlighted by green circles; (ii) calculated ΔG_{max} can change in a large range, from ΔG=1.44 to 2.45 eV, indicating the remarkable difference between these groups; (iii) same functional group (e.g., nitrile) may perform differently (ΔG_{max}=2.09 eV vs 1.17 eV in the periodical model, see Fig. 3), which should be related to LCC stability as determined by local carbon structures.

For all the five, the generation of LCC results in large ΔG, with four being PDS, except N_D, whose PDS comes from the initial hydrogenation (2.45 eV). This is reasonable because such step has to break the sp^2 network, highlighting the importance of heteroatoms and defects because they can break the perfect sp^2 hybridization. Therefore, the energy cost for N-groups evolution is mainly used to generate LCC, which are active for N_2 adsorption and reduction as identified from Section 3.2. Another interesting result is the competition between LCC and NH_x during the evolution. As demonstrated by pyrrol group in Fig. 3(b), the second hydrogen

added to the system prefers to bond with local LCC, rather than -NH. As a result, new C-H bond is generated, which brings large barrier to break when pyrrol group needs regeneration. Similar competition has been found for pyridine group, as shown in Fig. 3(b). Based on these results, it appears that additional mechanism should be introduced to stabilize LCC and promote N-groups regeneration.

O-groups are also widely found in carbon-based materials, especially for graphene oxides and biomass-derived carbon. Different from N-groups, they do not contain nitrogen; therefore, they cannot affect the N-source and accurate measurement of NH_3 yield. However, O-groups may also react with protons and electrons, releasing H_2O and generating LCC. Therefore, their evolution under electrochemical conditions is also important. The investigation is based on a similar-size cluster, as shown in Fig. 4(a), in which five O-groups have been contained, namely ketone, furfuryl, carboxylic acid, doped oxygen (O_D) and hydroxyl groups. Starting from this cluster, hydrogen has been added to O-site, towards the formations of H_2O and LCC. The energy profile and key parts for the intermediate states have been shown in Fig. 4(b). It is very interesting to see: (i) similar LCC and residual fragments with N-groups evolution have been observed; (ii) PDS often comes from the formation of LCC, except O_D because the initial hydrogenation needs to break the sp^2 network as discussed for N_D case; and (iii) local C-H bonds can be generated based on a competition with OH or H_2O formation. Based on these features, it is concluded that O-groups evolutions can result in the formation of LCC and similar active structures with N-groups.

Figure 3. Evolution of N-groups. (a) Cluster model with five N-groups; (b) Calculated free energy profile associated with elementary steps involved in the evolution. Carbon, nitrogen and hydrogen are shown as grey, blue and white spheres. Hydrogen is directly introduced to the evolution process through coupled electron and proton.
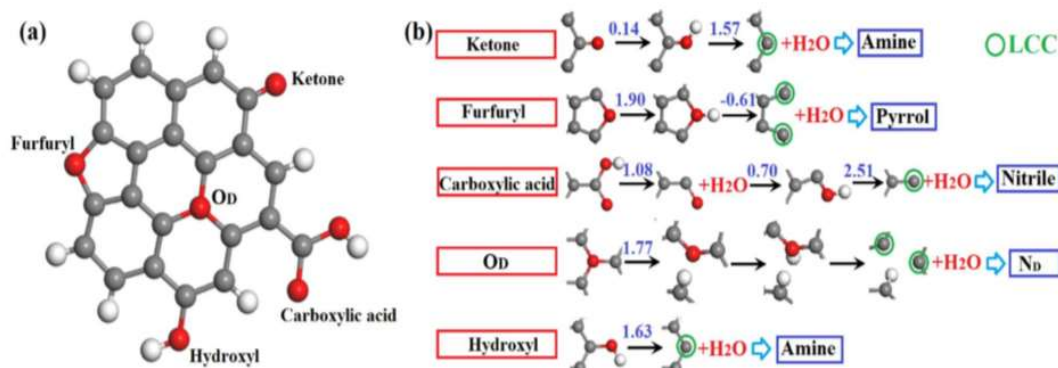
Figure 4. Evolution of O-groups. (a) Cluster model with five O-groups; (b) Calculated free energy profile associated with elementary steps involved in the evolution.

3.4 NRR Catalyzed by LCC

Based on the above sections, the evolution of both N- and O-groups can result in active LCC. Now the central question is whether such LCC can serve as active sites to catalyze full NRR and regenerate same or similar functional groups so that such process can continue. As shown in Fig. 5, the final structure obtained from pyridine evolution is similar with that from amine or pyrrol, so it is not considered separately. In addition, Fig. 4 shows an example of full NRR over pyridine group, which can be employed as a reference too. Given O-groups lead to similar LCC with N-groups, we focus on the activity of LCC generated from the evolutions of amine, nitrile, N_D and pyrrol.

The investigation of LCC-catalyzed full NRR starts with N_2 adsorption, as shown in Fig. 5. Step by step, one NH_3 has been released, following which additional hydrogenation regenerates N-groups. In other words, the production of two NH_3 molecules from each N_2 molecule is actually achieved at two stages, one at the evolution stage (see Fig. 4) and one from nitrogen reduction after N-

groups evolution. According to the calculated ΔG, PDS associated with LCC-catalysed NRR is smaller than that for functional groups evolution, with ΔG_{max} being in the range of 0.21-1.53 eV.

From the above analysis, the following roles of LCC can be identified: (i) strengthening N_2 adsorption due to high reactivity; (ii) activating N_2 for following hydrogenation, which can be reflected by the small or negative ΔG for $N_2 \rightarrow N_2H$; and (iii) regenerating N-groups so that sustainable NH_3 production can be achieved. At the same time, it is worth to note that high energy cost is resulted for LCC generation; as a result, PDS is often from the stage of functional groups evolution. Moreover, LCC may compete with NH_x for hydrogenation and form local C-H bonds. Given fully H-terminated carbon shows low reactivity and large barrier for C-H actitation (similar with Pore in Scheme 1), it is highly necessary to supress C-H formation and keep LCC active. LCC stabilization agent can be helpful for this purpose, as stabilized LCC can remarkably reduce ΔG_{max} based on Figs. 4-6. Experimentally, alkali metal ions (M+) have been reported as an agent to stabilize active sites during NRR, which mechanism deserves better understanding.
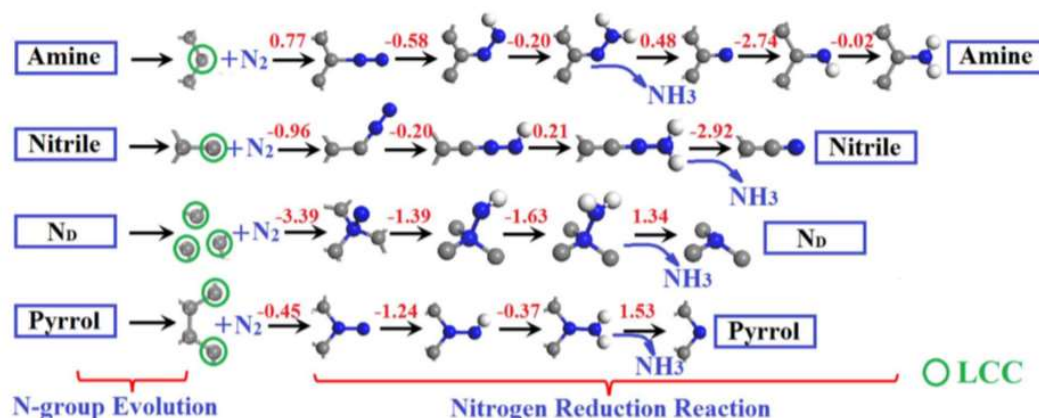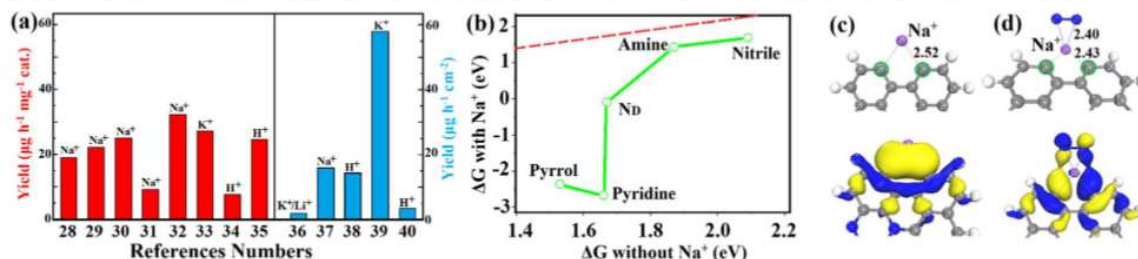

Figure 5. LCC-catalysed NRR. Calculated ΔG for each elementary step is show in unit of eV. Four N-groups are same as those shown in Fig. 4.

3.5 LCC Stabilization

In most NRR tests, buffer solutions have been widely employed, like Na_2SO_4, etc. We collected the NRR performance of 13 carbon catalysts in Table S1,[28-40] with nine being tested with electrolytes containing alkali metal ions, as shown in Fig. 6(a), based on which Na^+ has been selected as the stabilization agent for demonstration. Specifically, PDS has been re-examined through comparing the free energy change ΔG with that when Na^+ is not presented, as shown in Fig. 6(b). The red dash line indicating ΔG(with Na^+)= ΔG(without Na^+); as a result, data points below this line indicate positive stabilization by Na^+. As shown in Fig. 6(b), all five N-groups have been effectively stabilized by Na^+, supporting the hypothesis that alkali ions may stabilize active sites (LCC in these cases). As explain in above analysis (Section 3.1), the instability of LCC is featured with dangling bonds (nonbonded electrons), whose HOMO states are shown in Fig. S2. To become stable, these electrons may interact with empty orbitals of Na^+, forming multiple centre bonding. To verify this consideration, we plotted optimized geometry and HOMO for LCC-Na^+ in Fig. 6(c) using two LCC atoms (highlighted by green circles) as an example. Before N_2 adsorption, Na^+ interacts with LCC atoms, with HOMO dominated by 6C-Na π-bonding. Connected by this Na^+, non-bonded electrons from two LCC atoms form stable bonds, confirming Na^+-induced stabilization. It also plays a role to adsorb N_2, as shown in Fig. 6(d), in which N_2 weakly adsorbs over Na^+ with a distance of 2.40 Å, similar with that between LCC and Na^+. Based on this geometry, LCC electrons can overlap with that from N_2, suggesting that Na^+ may play a key role to assist N_2 adsorption over LCC. In 1994, Li-mediated NRR was reported by Sakata et al., in which it was believed that Li^+ turns to be active Li after accepting one electron and further react with N_2 to form Li_3N.[61] Such N_2 reduction strongly relies on the proton source because Li_3N is not stable and will further react to release NH_3 and organic salt. A full NRR process can be established with a reasonable energy cost,[62,63] but Li can hardly maintain fully reduced state in aqueous solutions. Therefore, it is essentially different from the mechanism suggested in Fig. 6. Another possibility is (Li^+ - electron pair) coupled state, which is more likely to be presented in water, such as [O-Li^+] state as proposed as active sites for NRR.[28] Most recently, K^+-promoted electrochemical NRR has been reported in the case of Bi-based catalysts, in which K^+ shows the capacity to stabilize N_2H^* state.[64] In fact, alkali ions have been reported as promotion agent for several reactions, like oxygen reduction[65,66] and N-deficient carbon nitride used for hydrogen evolution.[67] Even so, it is worth to point out that acid electrolyte (eg., H_2SO_4) without alkali ions has also been employed to test carbon structures, which also show NRR performance[34-35,38,40]; therefore, we cannot rule out other stabilization mechanism at this moment. In fact, the effect of electrolyte cations on NRR performance of catalysts is far from full understanding,[57] and more work should be carried out to advance the knowledge of these non-metal active sites, such as: (i) how to avoid C-H termination if no special agent is introduced to stabilize LCC, (ii) how to achieve high NRR selectivity, and (iii) whether linear scaling relationship is still applicable for LCC-catalysed NRR. All these are critical for following catalysts design, as highlighted by a recent reiew.[68]

Figure 6. Effect of M+. (a) Experimental work with the use of alkali metal ions. (b) Calculated ΔG for PDS associated with LCC-Catalysed NRR; (c) Na+ effect on the stabilization of non-bonded electrons of LCC and N_2 adsorption. LCC is highlighted by green circle.

4 Conclusion

In summary, we examined the NRR reactivity of various carbon-based structures, including defects, functional groups and dopants by DFT calculations. We demonstrated that these factors, except carbon vacancies, may promote N_2 adsorption, but not enough to activate N_2 to achieve full NRR efficiently. Functional groups can evolute from one to another and generate active LCC, which has been identified as the key reactivity origin for observed NRR catalysis by carbon materials. To achieve NRR, LCC stabilization should be fully considered, and alkali metal ions (M+), as widely contained in electrolyte, offers such stabilization capacity. Given carbon materials have been widely employed to host NRR catalysts, this work would suggest experimentalists to consider specific treatments to introduce more defects, N- and O-groups and optimize them to fully utilize carbon-substrate for optimum performance.

ASSOCIATED CONTENT

Supporting Information. The Supporting Information is available free of charge on the ACS Publication website at DOI:
Computational details (PDF)

AUTHOR INFORMATION

*chenghuasun@swin.edu.au

Notes

The authors declare no competing financial interest.

ACKNOWLEDGMENT

REFERENCES

(1) Schlögl, R., Ammonia Synthesis. *Handbook of Heterogeneous Catalysis* **2008.**

(2) Tamaru. K. *Catalytic ammonia synthesis.* Plenum Press: New York **1991.**

(3) Kandemir, T.; Schuster, M. E.; Senyshyn, A.; Behrens, M.; Schlögl, R. The Haber–Bosch Process Revisited: On the Real Structure and Stability of "Ammonia Iron" under Working Conditions. *Angew. Chem. Int. Edi.* **2013**, *52* (48), 12723-12726.

(4) Erisman, J. W.; Sutton, M. A.; Galloway, J.; Klimont, Z.; Winiwarter, W. How a Century of Ammonia Synthesis Changed the World. *Nature Geosci.* **2008**, *1*, 636.

(5) Chen, J. G.; Crooks, R. M.; Seefeldt, L. C.; Bren, K. L.; Bullock, R. M.; Darensbourg, M. Y.; Holland, P. L.; Hoffman, B.; Janik, M. J.; Jones, A. K.; Kanatzidis, M. G.; King, P.; Lancaster, K. M.; Lymar, S. V.; Pfromm, P.; Schneider, W. F.; Schrock, R. R. Beyond Fossil Fuel–Driven Nitrogen Transformations. *Science* **2018**, *360* (6391).

(6) Guo, C.; Ran, J.; Vasileff, A.; Qiao, S. Z. Rational design of electrocatalysts and photo(electro)catalysts for nitrogen reduction to ammonia (NH3) under ambient conditions. *Energy Environ. Sci.* **2018**, *11* (1), 45-56.

(7) Wang, Q.; Lei, Y.; Wang, D.; Li, Y. Defect Engineering in Earth-Abundant Electrocatalysts for CO2 and N2 Reduction. *Energy Environ. Sci.* **2019**, DOI: 10.1039/C8EE03781G.

(8) Cao, N.; Zheng, G. Aqueous Electrocatalytic N2 Reduction under Ambient Conditions. *Nano Research.* **2018**, *11* (6), 2992-3008.

(9) Cui, X.; Tang, C.; Zhang, Q. A Review of Electrocatalytic Reduction of Dinitrogen to Ammonia under Ambient Conditions. *Adv. Energy Mater.* **2018**, *8* (22), 1800369.

(10) Jin, H.; Guo, C.; Liu, X.; Liu, J.; Vasileff, A.; Jiao, Y.; Zheng, Y.; Qiao, S.-Z. Emerging Two-Dimensional Nanomaterials for Electrocatalysis. *Chem. Rev.* **2018**, *118* (13), 6337-6408.

(11) Zhang, B.-W.; Wang, Y. X.; Chou, S. L.; Liu, H. K.; Dou, S. X. Fabrication of Superior Single-Atom Catalysts toward Diverse Electrochemical Reactions. *Small Methods.* **2019**, *0* (0), 1800497.

(12) Zhang, L.; Chen, G. F.; Ding, L. X.; Wang, H. Advanced Non-metallic Catalysts for Electrochemical Nitrogen Reduction under Ambient Conditions. *Chem. Eur. J.* **2019**, *0* (ja).

(13) Azofra, L. M.; Li, N.; MacFarlane, D. R.; Sun, C. Promising Prospects for 2D d2–d4 M3C2 Transition Metal Carbides (MXenes) in N2 Capture and Conversion into Ammonia. *Energy Environ. Sci.* **2016**, *9* (8), 2545-2549.

(14) Li, Q.; He, L.; Sun, C.; Zhang, X. Computational Study of MoN2 Monolayer as Electrochemical Catalysts for Nitrogen Reduction. *J. Phys. Chem. C.* **2017**, *121* (49), 27563-27568.

(15) Li, L.; Tang, C.; Xia, B.; Jin, H.; Zheng, Y.; Qiao, S. Z. Two-Dimensional Mosaic Bismuth Nanosheets for Highly Selective Ambient Electrocatalytic Nitrogen Reduction. *ACS Catal.* **2019**, *9* (4), 2902-2908.

(16) Qin, G.; Cui, Q.; Du, A.; Wang, W.; Sun, Q. Transition Metal Diborides: A New Type of High-performance Electrocatalysts for Nitrogen Reduction. *ChemCatChem.* **2019**, DOI: 10.1002/cctc.201900538.

(17) Wang, Y.; Shi, M. M.; Bao, D.; Meng, F. L.; Zhang, Q.; Zhou, Y. T.; Liu, K. H.; Zhang, Y.; Wang, J. Z.; Chen, Z. W.; Liu, D. P.; Jiang, Z.; Luo, M.; Gu, L.; Zhang, Q. H.; Cao, X. Z.; Yao, Y.; Shao, M. H.; Zhang, Y.; Zhang, X.-B.; Chen, J. G.; Yan, J.-m.; Jiang, Q. Generating Defect-Rich Bismuth for Enhancing Rate of Nitrogen Electroreduction to Ammonia. *Angew.Chem. Int. Edi.* **2019**, DOI: 10.1002/anie.201903969.

(18) Li, X.-F.; Li, Q.-K.; Cheng, J.; Liu, L.; Yan, Q.; Wu, Y.; Zhang, X.-H.; Wang, Z.-Y.; Qiu, Q.; Luo, Y. Conversion of Dinitrogen to Ammonia by FeN3-Embedded Graphene. *J. Am. Chem.Soc.* **2016,** *138* (28), 8706-8709.

(19) Zhao, J.; Chen, Z. Single Mo Atom Supported on Defective Boron Nitride Monolayer as an Efficient Electrocatalyst for Nitrogen

Fixation: A Computational Study. *J. Am. Chem.Soc.* **2017**, *139* (36), 12480-12487.

(20) Azofra, L. M.; Sun, C.; Cavallo, L.; MacFarlane, D. R. Feasibility of N2 Binding and Reduction to Ammonia on Fe-Deposited MoS2 2D Sheets: A DFT Study. *Chem. -Eur. J.* **2017**, *23* (34), 8275-8279.

(21) Ling, C.; Ouyang, Y.; Li, Q.; Bai, X.; Mao, X.; Du, A.; Wang, J. A General Two-Step Strategy–Based High-Throughput Screening of Single Atom Catalysts for Nitrogen Fixation. *Small Methods.* **2018**, *0* (0), 1800376.

(22) Zhang, X.; Chen, A.; Zhang, Z.; Zhou, Z. Double-atom catalysts: transition metal dimer-anchored C2N monolayers as N2 fixation electrocatalysts. *J. Mater. Chem. A.* **2018**, *6* (38), 18599-18604.

(23) Li, Q.; Qiu, S.; Liu, C.; Liu, M.; He, L.; Zhang, X.; Sun, C. Computational Design of Single-Molybdenum Catalysts for the Nitrogen Reduction Reaction. *J. Phys. Chem. C.* **2019**, *123* (4), 2347-2352.

(24) Wang, M.; Liu, S.; Qian, T.; Liu, J.; Zhou, J.; Ji, H.; Xiong, J.; Zhong, J.; Yan, C. Over 56.55% Faradaic efficiency of ambient ammonia synthesis enabled by positively shifting the reaction potential. *Nature Commun.* **2019**, *10* (1), 341.

(25) Liu, C.; Li, Q.; Zhang, J.; Jin, Y.; MacFarlane, D. R.; Sun, C. Conversion of dinitrogen to ammonia on Ru atoms supported on boron sheets: a DFT study. *J. Mater. Chem. A.* **2019**, *7* (9), 4771-4776.

(26) Zhao, W.; Zhang, L.; Luo, Q.; Hu, Z.; Zhang, W.; Smith, S.; Yang, J. Single Mo1(Cr1) Atom on Nitrogen-Doped Graphene Enables Highly Selective Electroreduction of Nitrogen into Ammonia. *ACS Catal.* **2019**, *9*, 3419-3425.

(27) McPherson, I. J.; Sudmeier, T.; Fellowes, J.; Tsang, S. C. E. Materials for electrochemical ammonia synthesis. *Dalton Trans.* **2019**, *48*, 1562-1568.

(28) Xia, L.; Wu, X.; Wang, Y.; Niu, Z.; Liu, Q.; Li, T.; Shi, X.; Asiri, A. M.; Sun, X. S-Doped Carbon Nanospheres: An Efficient Electrocatalyst toward Artificial N2 Fixation to NH3. *Small Methods* **2018**, 180025.

(29) Zhao, C.; Zhang, S.; Han, M.; Zhang, X.; Liu, Y.; Li, W.; Chen, C.; Wang, G.; Zhang, H.; Zhao, H. Ambient Electrosynthesis of Ammonia on a Biomass-Derived Nitrogen-Doped Porous Carbon Electrocatalyst: Contribution of Pyridinic Nitrogen. *ACS Energy Lett.* **2019**, *4*, 2377-383.

(30) Wu,T.; Li, P.; Wang, H.; Zhao, R.; Zhou, Q.; Kong, W .; Liu, M.; Zhang, Y.; Sun, X.; Gong, F. Biomass-derived oxygen-doped hollow carbon microtubes for electrocatalytic N2-to-NH3 fixation under ambient conditions. *Chem. Commun.* **2019**, *55*, 2684-2687 .

(31) Zhao, J.; Yang,J.; Ji,L.; Wang,H.; Chen,H.; Niu,Z.; Liu,Q.; Li,T.; Cui,G.; Sun,X. Defect-rich fluorographene nanosheets for artificial N2fixation under ambient conditions. *Chem. Commun.* **2019**, *55*, 4266-4269.

(32) Zhao,J.; Wang,B.; Zhou,Q.; Wang ,H.; Li,X.; Chen,H.; Wei,Q.; Wu,D.; Luo,Y.; You,J.; Gong,F.; Sun,Q. Efficient electrohydrogenation of N2 to NH3 by oxidized carbon nanotubes under ambient conditions. *Chem. Commun.* **2019**, *55*, 4997-5000.

(33) Xia, L.; Yang, J.; Wang, H.; Zhao, R.; Chen, H.; Fang, W.; Asiri, A. M.; Xie, F.; Cui, G.; Sun, X. Sulfur-doped graphene for efficient electrocatalytic N2-to-NH3 fixation. *Chem commun.* **2019**, *55*, 3371-3374.

(34) Tian, Y.; Xu, D.; Chu, K.; We, Z.; Liu, W. Metal-free N, S co-doped graphene for efficient and durable nitrogen reduction reaction. *Mater. Sci.* **2019**. *54*, 9088-9097.

(35) Li, P.; Wang, J.; Chen, H.; Sun, X.; You, J.; Liu, S.; Zhang, Y.; Liu, M.; Niu, X.; Luo, Y. Synergistic Electrocatalytic N2 Reduction Using a PTCA Nanorod–rGO Hybrid. *J. Mater. Chem. A.* **2019**,*7*, 12446-12450.

(36) Chen, G-F.; Cao, X.; Wu, S.; Zeng, X.; Ding, L-X.; Zhu, M.; Wang,H. Ammonia Electrosynthesis with High Selectivity under Ambient Conditions via a Li+ Incorporation Strategy. *J. Am. Chem. Soc.* **2017**, *139*, 9771-9774.

(37) Li, W.; Wu, T.; Zhang, S.; Liu, Y.; Zhao, C.; Liu, G.; Wang, G.; Zhang, H.; Zhao, H. Nitrogen-Free Commercial Carbon Cloth with Rich Defects for Electrocatalytic Ammonia Synthesis under Ambient Conditions. *Chem. Commun.* **2018**, *54*, 11188-11191.

(38) Liu, Y.; Su, Y.; Quan, X.; Fan, X.; Chen, S.; Yu, H.; Zhao, H.; Zhang, Y.; Zhao, J. Facile Ammonia Synthesis from Electrocatalytic

N₂ Reduction under Ambient Conditions on N-Doped Porous Carbon. *ACS Catal.* **2018**, 8, 1186-1191.

(39) Mukherjee, S.; Cullen, D. A.; Karakalos, S.; Liu, K.; Zhang, H.; Zhao, S.; Xu, H.; More, K. L.; Wang, G.; Wu, G. Metal-organic framework-derived nitrogen-doped highly disordered carbon for electrochemical ammonia synthesis using N₂ and H₂O in alkaline electrolytes. *Nano Energy.* **2018**, 48, 217-226.

(40) Yu, J.; Li, J.; Zhu, X.; Zhang, X.; Jia, K.; Kong, W.; Wei, P.; Chen, H.; Sh, X.; Asiri, A. M.; Li, Q.; Sun, A. tructured Polyaniline: An Efficient and Durable Electrocatalyst for the Nitrogen Reduction Reaction in Acidic Media. *ChemElectroChem.* **2019**, 6, 2215-2281.

(41) Suranto, B. H. R.; Du, H.; Wang, D.; Chen, J.; Simonov, A. N.; MacFarlane, D. R. Challenges and prospects in the catalysis of electroreduction of nitrogen to ammonia. *Nature Cata.* **2019**, 2, 290−296.

(42) Zhao, Y.; Shi, R.; Bian, X.; Zhou, C.; Zhao, Y.; Zhang, S.; Wu, F.; Waterhouse, G. I. N.; Wu, L.; Tung, C.; Zhang, T. Ammonia Detection Methods in Photocatalytic and Electrocatalytic Experiments: How to Improve the Reliability of NH₃ Production Rates? *Adv. Sci.* **2019**, 6, 1802109.

(43) Andersen, S. Z.; Čolić, V.; Yang, S.; Schwalbe, J. A.; Nielander, A.C.; McEnaney, J. M.; Enemark-Rasmussen, K.; Baker, J. G.; Singh, A.R.; Rohr, B. A.; Statt, M. J.; Blair, S. J.; Mezzavilla, S.; Kibsgaard, J.; Vesborg, P. C. K.; Cargnello, M.; Bent, S. F. ; Jaramillo, T. F.; Stephens, I. E. L.; Nøskov, J. K.; Chorkendorff, I. A rigorous electrochemical ammonia synthesis protocol with quantitative isotope measurements . *Nature*, **2019**, DOI: 10.1038/s41586-019-1260-x.

(44) Perdew, J. P.; Burke, K. and Ernzerhof, M. Generalized Gradient Approximation Made Simple. *Phys. Rev. Lett.* **1996**, 77, 3865.

(45) Kresse, G and Joubert, D. From ultrasoft pseudopotentials to the projector augmented-wave method. *Phys. Rev. B.* **1999**, 59, 1758.

(46) Grimme, S.; Antony, J.; Ehrlich, S.; Krieg, H. A consistent and accurate *ab initio* parametrization of density functional dispersion correction (DFT-D) for the 94 elements H-Pu. *Chem. Phys.* **2010**, 132, 154104.

(47) Honkala, K.; Hellman,A.; Remediakis,I.N.; Logadottir, A.; Carlsson, A.; Dahl, S.; Christensen, C. H. Ammonia synthesis from first-principles calculations. *Science.* **2005**, 307, 555−558.

(48) Tang, Q.; Jiang, D. E. Mechanism of Hydrogen Evolution Reaction on 1T-MoS₂ from First Principles. *ACS Catal.* **2016**, 6, 4953-4961.

(49) Gao, G.; P. O'Mullane, A.; Du, A. 2D MXenes: A New Family of Promising Catalysts for the Hydrogen Evolution Reaction. *ACS Catal.* **2017**, 7, 494-500.

(50) Jacobsen, C. J. H.; Dahl, S.; Clausen, B. S.; Bahn, S. ; Logadottir, A.; Nørskov, J. K. Catalyst Design by Interpolation in the Periodic Table: Bimetallic Ammonia Synthesis Catalysts. *J. Am. Chem. Soc.* **2001**, 123, 34, 8404-8405.

(51) Skúlason, E.; Bligaard, T.; Gudmundsdóttir, S.; Studt, F.; Rossmeisl, J.; Abild-Pedersen, F.; Vegge, T. ; Jónsson, H.; Nørskov, J. K. A theoretical evaluation of possible transition metal electro-catalysts for N₂ reduction. *Phys. Chem. Chem. Phys.* **2012**, 14, 1235-1245.

(52) Li, Q.; Qiu, S. Y.; Liu, C. W.; Liu, M. G.; He, L. Z.; Zhang, X. W.; Sun, C. Computational Design of Single-Molybdenum Catalysts for the Nitrogen Reduction Reaction. *J. Phys. Chem. C.* **2019**, 123, 2347−2352.

(53) Zhou, F.; Azofra, L. M.; Ali, M.; Kar, M.; Simonov, A. N.; McDonnell-Worth, C.; Sun, C.; Zhang,X.; MacFarlane, D. R.; Electro-synthesis of ammonia from nitrogen at ambient temperature and pressure in ionic liquids. *Energy Environ. Sci.* **2017**, 10, 2516-2520.

(54) Luo, Y-R. Handbook of Chemical Bond and Energies. CRC Press **2007**.

(55) Jia, Y.; Zhang, L.; Du, A.; Gao, G.; Chen, J.; Yan, X.; Brown , C. L.; Yao, X. Defect Graphene as a Trifunctional Catalyst for Electrochemical Reactions. *Adv. Mater.* **2016**, 28, 9532 .

(56) Chen, C. ; Yan, D. ; Wang, Y. ; Zhou, Y.; Zou, Y.; Li, Y.; Wang. S. B-N Pairs Enriched Defective Carbon Nanosheets for Ammonia Synthesis with High Efficiency. *Small.* **2018**, 201805029.

(57) Zhao, S.; Lu, X.; Wang, L.; Gale, J.; Amal, R. Carbon-based metal-free catalysts for electrocatalytic reduction of nitrogen for synthesis of ammonia at ambient conditions. *Adv. Mater.* **2019**, 31, 1805367.

(58) Guo, X.; Huang, S. Tuning nitrogen reduction reaction activity via controllable Fe magnetic moment: A computational study of single Fe atom supported on defective graphene. *Electrochimica Acta.* **2018**, 284, 392.

(59)Tian, Y. H.; Hu, S.; Sheng, X.; Duan, Y.; Jakowski, J.; Sumpter, B. G.; Huang, J. Non-Transition-Metal Catalytic System for N₂ Reduction to NH₃: A Density Functional Theory Study of Al-Doped Graphene. *J Phys Chem Lett.* **2018**, 9 (3), 570.

(60)Zhu, H. R.; Hu, Y. L.; Wei, S. H.; Hua, D. Y. Single-Metal Atom Anchored on Boron Monolayer (β₁₂) as an Electrocatalyst for Nitrogen Reduction into Ammonia at Ambient Conditions: A First-Principles Study. *J Phys.Chem. C.* **2019**, 123 (7), 4274.

(61) Tsuneto, A.; Kudo, A.; Sakata, T. Lithium-mediated electrochemical reduction of high pressure N₂ to NH₃. *J. Electrochemical. Chem.* **1994**, 367 (1-2) , 183-188.

(62) McEnaney, J. M.; Singh, A. R.; Schwalbe, J. A.; Kibsgaard, J.; Lin, J. C.; Cargnello, M.; Jaramillo, T. F.; Nørskov,J.K., Ammonia synthesis from N₂ and H₂O using a lithium cycling electrification strategy at atmospheric pressure. *Energy Environ. Sci.* **2017**, 10, 1621-1630.

(63) Kim, K.; Lee, S. J.; Kim, D.; Yoo, C.; Choi, J. W.; Kim, J.; Woo,Y.; Yoon, H. C.; Han, J. Electrochemical Synthesis of Ammonia from Water and Nitrogen: A Lithium-Mediated Approach Using Lithium-Ion Conducting Glass Ceramics. *ChemSusChem.* **2018**, 11, 120 − 124.

(64) Hao, Y. C.; Guo, Y.; Chen, L. W.; Shu, M.; Wang, X. Y.; Bu, T. A.; Gao, W. Y.; Zhang, N.; Su, X.; Feng, X.; Zhou, J. W.; Wang, B.; Hu, C. W.; Yin, A. X.; Si, R.; Zhang, Y. W.; Yan, C. H. Promoting nitrogen electroreduction to ammonia with bismuth nanocrystals and potassium cations in water. *Nature Catal.* **2019**, 2, 448−456.

(65) Yu, H.; Shi, R.; Zhao, Y.; Bian, T.; Zhao, Y.; Zhou, C.; Waterhouse, G. I. N.; Wu, L.; Tung, C. H.; Zhang, T. Alkali-Assisted Synthesis of Nitrogen Deficient Graphitic Carbon Nitride with Tunable Band Structures for Efficient Visible-Light-Driven Hydrogen Evolution. *Adv. Mater.* **2017**, 29, 1605148.

(66) Zhou, Y.; Sun, Y.; Zhu, C.; Liu, Y.; Dai, X. ; Zhong, J.; Chen, Q.; Tian, H.; Zhou, R.; Kang, Z. C−O⁻K⁺ (Na⁺) groups in non-doped carbon as active sites for the oxygen reduction reaction. *J. Mater. Chem. A.* **2018**, 6, 8955-8961.

(67) Strmcnik, D.; van der Vliet, D. F.; Chang, K. C.; Komanicky, V.; Kodama, K.; You, H.; Stamenkovic, V. R.; Markovic, N. M. Effects of Li⁺, K⁺, and Ba²⁺ Cations on the ORR at Model and High Surface Area Pt and Au Surfaces in Alkaline Solutions. *J. Phys. Chem. Lett.* **2011**, 2, 2733-2736.

(68). Tang, C.; Qiao, S. Z. How to Explore Ambient Electrocatalytic Nitrogen Reduction Reliably and Insightfully. *Chem. Soc. Rev.* **2019**, DOI: 10.1039/c9cs00280d.

Chapter 3 MoN$_2$ Nanosheet as NRR Catalyst

3.1 Overview

As demonstrated by graphene-based catalysts in Chapter 2, effective adsorption of nitrogen is the first step for NRR and plays a key role for following activation and reduction. In nature, such N$_2$ fixation by iron (Fe) and molybdenum (Mo) contained in nitrogenases, both of which have been widely identified as excellent metals to adsorb N$_2$. Therefore, Fe- and Mo-based compounds and single-atom catalysts have been actively studied in the literature.

This chapter aims to explore the reactivity of 2D molybdenum nitride monolayer (MoN$_2$) for NRR. It is selected because Mo offers strong capacity to fix N$_2$, and N-Mo bonding can mediate the performance of Mo-site, which may bring better performance than pure Mo metals. In addition, lattice nitrogen is directly exposed to the electrolyte and may react with protons to release NH$_3$, generating nitrogen vacancy (NV). As presented below, such mechanism actually dominates the reaction with the following key features: (i) NV shows excellent capacity to adsorb and activate N$_2$; (ii) such NV can regenerated with full nitrogen reduction; and (iii) iron-doping can remarkably improve the performance, achieving low energy cost for NRR as indicated by calculated ΔGmax=0.47 eV.

This work has been published on The Journal of Physical Chemistry C titled as "Computational Study of MoN$_2$ Monolayer as Electrochemical Catalysts for Nitrogen Reduction' by Qinye Li, Lizhong He, Chenghua Sun, Xiwang Zhang. (*J. Phys. Chem. C* 121, 27563-27568 (2017)).

Computational Study of MoN$_2$ Monolayer as Electrochemical Catalysts for Nitrogen Reduction

Qinye Li,[†] Lizhong He,[†] Chenghua Sun,*[,‡] and Xiwang Zhang*[,†]

[†]School of Chemical Engineering, Monash University, Clayton, VIC 3800, Australia

[‡]Department of Chemistry and Biotechnology, Faculty of Science, Engineering & Technology, Swinburne University of Technology, Hawthorn, VIC 3122, Australia

ABSTRACT: Metallic two-dimensional materials are emerging as promising catalysts for several reactions. This work reports a computational study of molybdenum nitride (MoN$_2$) nanosheet as a catalyst for ammonia synthesis at room temperature under the scheme of density functional theory. Pure MoN$_2$ shows excellent performance for dinitrogen adsorption and activation, but large energy input is needed to refresh the surface following the reaction. Iron (Fe) doping can effectively improve it to achieve full nitrogen reduction with a calculated overpotential of 0.47 V, indicating that Fe-doped MoN$_2$ is a promising catalyst for electrochemical synthesis of ammonia from water and air.
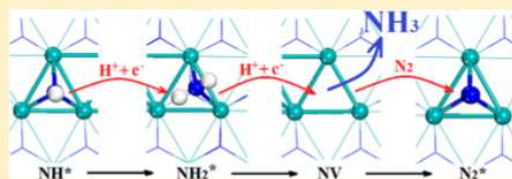
1. INTRODUCTION

Ammonia (NH$_3$) is a simple chemical and is massively produced in the industry, basically for modern fertilizer, and is widely employed as a reactant for the production of plastics, fibers, explosives, and so forth.[1−3] It is produced predominantly on the basis of the well-known Haber−Bosch process, typically operated at 500 °C and 300 ATM with natural gas as the hydrogen source, leading to large energy consumption and carbon emission.[4] This may not be necessary because the reaction is actually exothermic and, in nature, nitrogen can be fixed efficiently by specific bacteria at room temperature with the catalysis by nitrogenase.[5,6] As inspired by nature, electrochemical synthesis of ammonia, using proton from water as the hydrogen source, has been widely studied, which is carbon-free and more energy-efficient.[7−11] Different from the Haber−Bosch process, the energy needed to achieve excellent kinetics can be provided by electricity in electrochemical synthesis, avoiding high temperature. As a result, high yield can be achieved because the entropy contribution to the change of Gibbs free energy for this reaction is positive. The challenge is how to activate dinitrogen at mild condition, which underlines the need of high-performance catalysts for nitrogen reduction reaction (NRR).

So far, various catalysts have been proposed and studied, including molecular catalysts,[12−14] metals,[15−17] and complex compounds.[18−21] Molecular catalysts are often designed using nitrogenase as a model and are obtained on the basis of synthetic chemistry. Following such strategies, complex molecules have been successfully synthesized and tested as NRR catalysts,[12] but the high cost and the low conductivity need to be seriously addressed. Metals offer excellent conductivity and can be cheap if earth-abundant, but in most cases, protons prefer to generate hydrogen rather than react with dinitrogen;[17] as a result, the Faraday efficiency is very low.

Complex compounds, particularly perovskite-[19,20] and spinel-type[21] catalysts, show improved performance compared with pure metals,[18] but when operated at room temperature, most metal oxides are not ideal catalysts for electrochemical reactions because of their low conductivity. In recent years, 2D materials have been identified as promising NRR catalysts.[22,23] Among 13 nitrides studied by computational calculations, Mo-based nitride has been predicted to show excellent performance, which only needs an energy input of 0.36 eV.[22] Recently, our group studied MXene carbides and found that 2D carbides can offer excellent thermodynamic and kinetics performance for NRR,[23] underpinning the huge potentiality of 2D materials.

In the literature, Mo-based systems have been successfully developed as high-performance catalysts for ammonia synthesis under the Haber−Bosch scheme.[24−31] To extend such success to the electrochemical synthesis of ammonia at room temperature, catalysts with high conductivity, stability in electrochemical conditions, and large surface areas are targeted. 2D Mo−N nanosheets may be considered as potential NRR electrochemical catalysts on the basis of (1) MoN$_2$ phases have been explored as novel catalysts for electrochemical reactions, such as hydrogen evolution;[32−34,37] (2) layered MoN$_2$ has been synthesized successfully,[35,36] with an excellent performance in CO hydrogenation; (3) the layer−layer interaction in MoN$_2$ is weak, and thus it can be stripped as monolayers,[38] in which case ultralarge surface areas can be expected; (4) the stability of MoN$_2$ monolayer has been predicted by a recent calculation.[39] On the basis of the earlier studies, MoN$_2$ monolayer can offer high conductivity, large surface area, and high stability, which are ideal for electrochemical catalysts. As demonstrated later,

untreated MoN$_2$ is an excellent starting material for the design of advanced NRR catalysts.

2. COMPUTATIONAL METHODS

Spin-polarized calculations are performed under the standard scheme of density functional theory (DFT) with revised Perdew−Burke−Ernzerhof (RPBE) exchange correlation functional,[40,41] as embedded in using the Vienna Ab-Initio Simulation Package,[42] together with a cutoff energy of 380 eV and a k-mesh of $5 \times 5 \times 1$ for the employed supercell. Herein, RPBE is employed on the basis of our tests, predicting reaction entropy and free energy as −1.06 eV and −0.43 eV, which are close to experimental data (−0.96 eV and −0.34 eV, respectively). The geometries for all intermediate states are optimized until all residual forces are less than 0.01 eV/Å, followed with the calculations of total energies which have been further corrected with the consideration of zero-point energy (ZPE). In each case, a vacuum space of at least 15 Å thickness is employed to prevent unphysical interaction between periodic images. DFT-D3 method with the standard parameters programmed by Goerigk and Grimme has been employed to correct the explicit dispersion.[43]

3. RESULTS AND DISCUSSION

3.1. H-Covered Surface. Different from the typical Haber−Bosch process, electrochemical catalysts need to be stable in the proton-rich solution. Because our target is to synthesize ammonia from air and water, it is highly necessary to examine the states of MoN$_2$ monolayer in water. Under the electrochemical conditions for NRR, electrons will be injected to MoN$_2$ as an energy input; as a result, positively charged protons will be attracted and can combine with electrons to form adsorbed hydrogen. For a perfect MoN$_2$ monolayer, as shown in Figure 1a, a negatively charged nitrogen is the outmost atom, serving as the basic H-adsorption site, labeled as H$_N$, and Mo serves as the secondary site, labeled as H$_{Mo}$. In principle, hydrogen may adsorb over the center of the Mo-triangle (as indicated by the red lines) and the top site and is labeled as H$_{Mo1}$ and H$_{Mo2}$, respectively, with an adsorption of
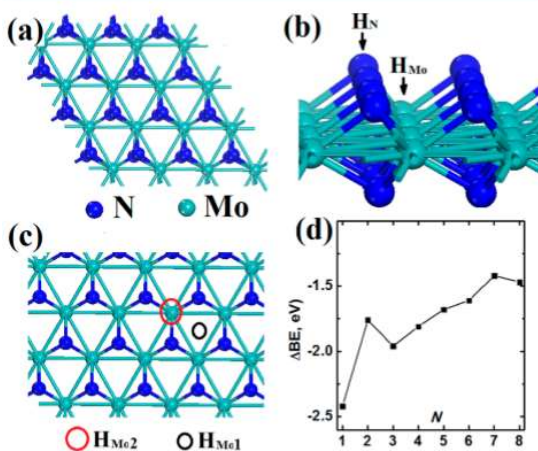

Figure 1. (a, b) Top and side views of MoN$_2$ monolayer. (c) Potential H-adsorption over Mo-site and (d) calculated Eads for H-adsorption over N-site versus H-coverage.

0.3−0.4 eV. The adsorption on nitrogen has been examined using the $2 \times 2 \times 1$ supercell, and the adsorption energy versus the number of adsorbed hydrogen, N, is shown in Figure 1d, according to which H-adsorption over nitrogen is much stronger than that on the Mo-site, with adsorption energy even lower than −1.00 eV for full coverage, suggesting that the monolayer will be terminated by hydrogen rapidly in the electrochemical condition.

3.2. Nitrogen Vacancy Generation. Once all nitrogen atoms are covered, a proton may combine with an electron over the electrode to react with −NH groups to form −NH$_2$, as indicated in Figure 2, which can further adsorb hydrogen to release NH$_3$ and generate the N-vacancy, with a small energy request (0.10 eV for H-terminated MoN$_2$); moreover, N-vacancy is an active site to fix molecular nitrogen, with a bonding energy BE = −0.28 eV. According to the earlier calculation, it appears that the Mars−van Krevelen mechanism for ammonia formation may be applicable to the MoN$_2$ monolayer, which has been proposed for Co$_3$Mo$_3$N,[44] one of the most active catalysts for ammonia synthesis on the basis of the Haber−Bosch process. However, it is necessary to point out that, for the Haber−Bosch process, it is often accepted that nitrogen is split as two N atoms at high temperature, namely, direct dissociation mechanism, while in the case of electrochemical conditions, both N$_2$ and H$_2$ do not have to be split. Thus, it is critical to examine whether adsorbed N$_2$ at the NV site can be effectively reduced.

3.3. Hydrogen Evolution Reaction (HER). HER is a major side reaction for NRR and can compete with NRR for the consumption of protons and electrons, resulting in low Faraday efficiency (FE) and low-energy efficiency.[17] Before we evaluate the catalysis performance of MoN$_2$, it would be good to examine the overpotential of HER over NV. In addition, it is helpful to test whether NV, as the key active site for N$_2$ adsorption as described earlier, can survive under the reaction condition given NV may be terminated by hydrogen.

In principle, HER may occur through the Heyrovsky step Hads $+ (H^+ + e^-) \rightarrow$ H$_2$ or the Tafel step 2Hads $\rightarrow$ H$_2$, with Hads referring to existing hydrogen bonded with nitrogen or molybdenum. We start from the analysis of HER associated with NH* given the surface will be terminated with hydrogen as described earlier. When the surface is fully H-terminated, the free-energy changes associated with HER steps are as follows:

$$NH^* + (H^+ + e^-) \rightarrow N^* + H_2 \qquad \Delta G = 1.07 \text{ eV}$$

$$NH^* + NH^* \rightarrow 2N^* + H_2 \qquad \Delta G = 2.09 \text{ eV}$$
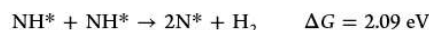
Clearly, HER over these NH* sites needs large energy input, which is essentially determined by the strong N−H bonding. Now, we turn to the examination of HER over NV, and the elementary steps with a need of energy input are shown (H* bonded with Mo):
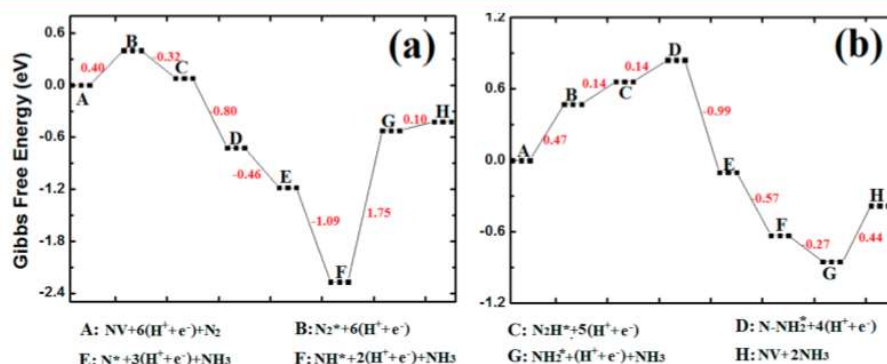
$$NV + (H^+ + e^-) \rightarrow H^* \qquad \Delta G = 0.70 \text{ eV}$$

$$H^* + (H^+ + e^-) \rightarrow 2H^* \qquad \Delta G = 0.20 \text{ eV}$$
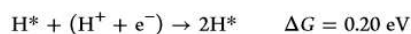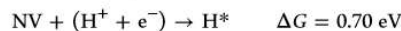
For comparison, the free-energy change associated with N$_2$ adsorption over NV has been listed as well

$$N_2 + NV \rightarrow N_2^* \qquad \Delta G = 0.40 \text{ eV}$$
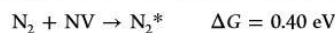
According to these results, N$_2$ adsorption is favorable over NV when no external voltage is applied, and HER needs a minimum energy input of 0.70 eV. This will be employed as a
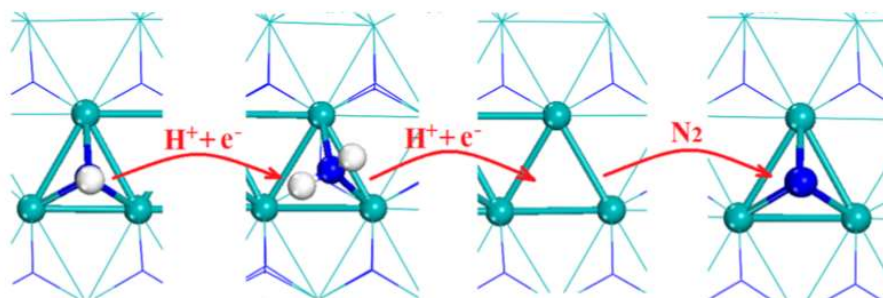
Figure 2. N_2 fixation through filling NV. (a) $NH^* + (H^+ + e^-) \rightarrow NH_2^*$; (b) $NH_2^* + (H^+ + e^-) \rightarrow NV + NH_3(g)$; (c) $N_2(g) + NV \rightarrow N_2^*$. N, Mo, and H are indicated by blue, cyan, and white spheres.

A: $NV+6(H^++e^-)+N_2$ B: $N_2^*+6(H^++e^-)$ C: $N_2H^*+5(H^++e^-)$ D: $N-NH_2^*+4(H^++e^-)$

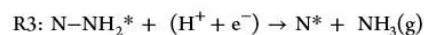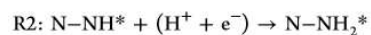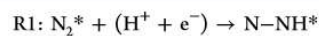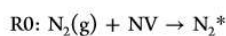E: $N^*+3(H^++e^-)+NH_3$ F: $NH^*+2(H^++e^-)+NH_3$ G: $NH_2^*+(H^++e^-)+NH_3$ H: $NV+2NH_3$

Figure 3. Proposed reaction steps associated with NRR on MoN_2 nanosheet. The component for each stage is indicated, and the calculated ΔG (red number) is shown in eV. (a) NRR over pure MoN_2; (b) NRR over Fe-doped MoN_2.
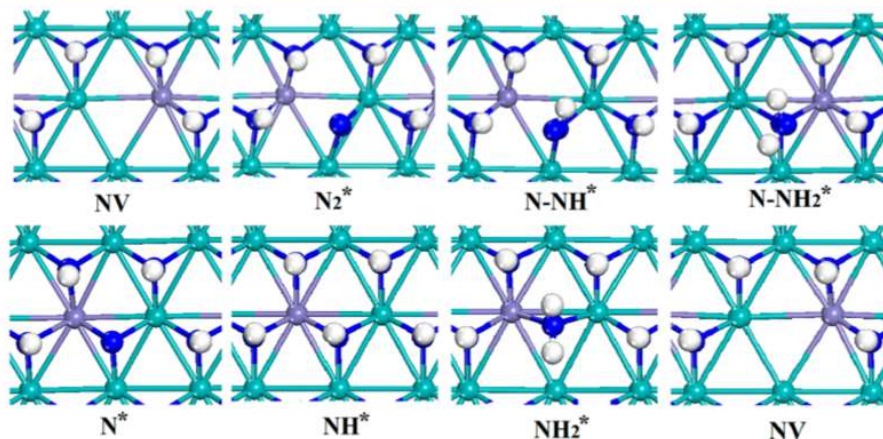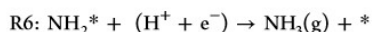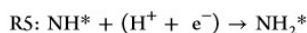

Figure 4. Optimized geometries for NRR intermediate states on Fe-doped MoN_2 nanosheet. Mo, Fe, N, and H are shown as surf, violet, blue, and white. The component (solid phase) for each stage is indicated below the image.

key parameter to evaluate the NRR catalysis in the following discussion.

3.4. NRR Elementary Steps. Now we turn to ammonia formation, starting from adsorbed N_2 on the NV site. Through comparison, the following elementary steps have been considered:

R0: $N_2(g) + NV \rightarrow N_2^*$

R1: $N_2^* + (H^+ + e^-) \rightarrow N-NH^*$

R2: $N-NH^* + (H^+ + e^-) \rightarrow N-NH_2^*$

R3: $N-NH_2^* + (H^+ + e^-) \rightarrow N^* + NH_3(g)$

R4: $N^* + (H^+ + e^-) \rightarrow NH^*$

R5: $NH^* + (H^+ + e^-) \rightarrow NH_2^*$

R6: $NH_2^* + (H^+ + e^-) \rightarrow NH_3(g) + *$
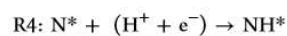
These results can be summarized in Figure 3a, in which the Gibbs free energy for the intermediate state $NV + 6(H^+ + e^-) + N_2(g)$ has been employed as the energy reference, together with the calculated ΔG (red numbers, in units of eV) for each elementary reaction, according to which the steps from N_2^* to the formation of the first ammonia are exothermic, suggesting that N_2 has been effectively activated. The real challenge comes from the formation of the second ammonia, and the rate-determining step (RDS) is the hydrogenation of NH^* to NH_2^*, which needs 1.75 eV, being remarkably higher than that requested by HER (0.70 eV), indicating that the FE should be low for pure MoN_2 when it is employed for ammonia synthesis. Such high energy demand indicates that the N−Mo bonding is too strong to break; therefore, dopants with relatively weak interaction with nitrogen is preferred. Later, iron (Fe) is employed given that Fe-based catalysts have been successfully employed for ammonia synthesis for decades, and the free-energy profile is shown in Figure 3b.

Fe-doping is modeled by replacing one Mo by Fe, and the optimized geometries for the NRR intermediates are shown in Figure 4, starting from clean Fe−MoN_2 with NV, labeled as NV. The calculated free energy is in Figure 3b for comparison. Three features are observed: (1) the adsorption of N_2 is still endothermic, with $\Delta G = 0.47$ eV, slightly higher than that on undoped MoN_2, confirming that Fe-doping weakens the N−metal interaction, and thus, early hydrogenations for the formation of the first ammonia becomes endothermic (0.14 eV), which is clearly different from undoped MoN_2; (2) the energy cost to form the second ammonia has been reduced remarkably, from 1.75 to 0.44 eV; and (3) RDS does not come from the formation of ammonia (maximum energy requirement is 0.44 eV for hydrogenation steps) but from N_2 adsorption ($\Delta G = 0.47$ eV), indicating that the overall performance is close to those of VN (0.51 eV) and CrN (0.46 eV), both of which have recently been predicted as high-performance NRR catalysts.[45] Further, HER has been examined for Fe-doped MoN_2, and over the vacancy, hydrogen may adsorb over Mo, or Fe, or the hole (surrounded by three metals). On the basis of our tests, H−Fe is favorable ($\Delta G = 0.49$ eV), which is slightly higher than that requested by NRR steps (0.47 eV), suggesting that Fe-doping can effectively improve the NRR selectivity over HER and offer higher FE. Overall, Fe-doped MoN_2 can be recommended as a promising NRR catalyst.

The promoting effect associated with Fe-doping can be understood from two aspects: (1) Mo−N interaction is very strong,[31] as evidenced by the capacity to catch N_2 and the negative ΔG for the first H-adding (see Figure 3a), which is helpful for N_2 activation but is not beneficial for the formation of the second NH_3, and Fe−N bonding is relatively weak and can balance the N_2 activation and NH_3 formation, being consistent with the design principle proposed by Jacobsen et al;[24] and (2) compared with Mo ([Kr] $5s^2 4d^4$), Fe ([Ar] $4s^2 3d^6$) offers more valence electrons, and with its four-coordinated states, high spin states at the t_2-states can be generated on the basis of the crystal field theory, and they are helpful for the reduction of N-containing moieties, agreeing well with the recent reports regarding FeN$_3$−graphene[46] and Fe−MoS_2,[47] both of which are promising candidates for NRR because of the existence of four-coordinated Fe.

It is worth to compare the presented Fe-doped MoN_2 nanosheet with several single-atom catalysts (SACs) designed in recent years.[46−48] For SACs, metals are lowly coordinated; as a result, strong N_2 adsorption is offered, and thus, N_2 can be effectively activated.[46−48] In some cases, the N_2 adsorption is through the enzyme module,[48] which is very beneficial for N_2 reduction. However, the disadvantage is that metal−N bonding may be too strong to release NH_3. In this work, N_2 adsorption and activation is achieved through NV, which can be regenerated with low energy input as discussed earlier, but stronger adsorption capacity is still needed to efficiently catch N_2 from the electrochemical solution. Our recent publication indicated that the use of ionic liquid is helpful to promote N_2 adsorption and to achieve much higher energy efficiency,[49] according to which the searching of high-performance NRR catalysts should be combined with the optimization of electrochemical reaction environment.

4. CONCLUSIONS

In summary, MoN_2 has been explored as a catalyst for electrochemical synthesis of ammonia at room temperature through DFT calculations. MoN_2 itself is not an ideal catalyst, requesting an energy input of 1.75 eV, but Fe-doping can remarkably improve its performance, with $\Delta G_{max} = 0.47$ eV for the RDS (N_2 adsorption). Accordingly, Fe-doped MoN_2 has been recommended as a promising catalyst for ammonia synthesis. Nitrogen vacancy plays the key role to adsorb and activate nitrogen, and Fe-dopants slightly weaken metal−nitrogen interactions and promote the formation of the second ammonia.

■ AUTHOR INFORMATION

Corresponding Authors

*E-mail: xiwang.zhang@monash.edu.
*E-mail: chenghuasun@swin.edu.au.

ORCID ◉

Lizhong He: 0000-0001-6569-526X
Chenghua Sun: 0000-0001-7654-669X

Notes

The authors declare no competing financial interest.

■ REFERENCES

(1) Smil, V. Detonator of the Population Explosion. *Nature* **1999**, *400*, 415.

(2) Smil, V. *Enriching the Earth: Fritz Haber, Carl Bosch, and the Transformation of World Food Production*; MIT Press: Cambridge, MA, 2004.

(3) *Mineral Commodity Summaries 2016*; U.S. Geological Survey, U.S. Government Printing Office: Washington, DC, 2016.

(4) Bozso, F.; Ertl, G.; Weiss, M. Interaction of Nitrogen with Iron Surfaces: II. Fe(110). *J. Catal.* **1977**, *50*, 519−529.

(5) Burgess, B. K.; Lowe, D. J. Mechanism of Molybdenum Nitrogenase. *Chem. Rev.* **1996**, *96*, 2983−3012.

33

(6) Hoffman, B. M.; Lukoyanov, D.; Yang, Z.; Dean, D. R.; Seefeldt, L. C. Mechanism of Nitrogen Fixation by Nitrogenase: the Next Stage. *Chem. Rev.* **2014**, *114*, 4041−4062.

(7) Shipman, M. A.; Symes, M. D. Recent Progress Towards the Electrosynthesis of Ammonia from Sustainable Resources. *Catal. Today* **2017**, *286*, 57−68.

(8) Kyriakou, V.; Garagounis, I.; Vasileiou, E.; Vourros, A.; Stoukides, M. Progress in the Electrochemical Synthesis of Ammonia. *Catal. Today* **2017**, *286*, 2−13.

(9) Garagounis, I.; Kyriakou, V.; Skodra, A.; Vasileiou, E.; Stoukides, M. Electrochemical Synthesis of Ammonia in Solid Electrolyte Cells. *Front. Energy Res.* **2014**, *2*, 1−10.

(10) Cui, B.; Zhang, J.; Liu, S.; Liu, X.; Xiang, W.; Liu, L.; Xin, H.; Lefler, M. J.; Licht, S. Electrochemical Synthesis of Ammonia Directly from N2 and Water over Iron-based Catalysts Supported on Activated Carbon. *Green Chem.* **2017**, *19*, 298−304.

(11) Chen, S.; Perathoner, S.; Ampelli, C.; Mebrahtu, C.; Su, D.; Centi, G. Electrocatalytic Synthesis of Ammonia at Room Temperature and Atmospheric Pressure from Water and Nitrogen on a Carbon-Nanotube-Based Electrocatalyst. *Angew. Chem.* **2017**, *129*, 2743−2747.

(12) Burford, R. J.; Yeo, A.; Fryzuk, M. D. Dinitrogen Activation by Group 4 and Group 5 Metal Complexes Supported by Phosphine-amido Containing Ligand Manifolds. *Coord. Chem. Rev.* **2017**, *334*, 84−99.

(13) McWilliams, S. F.; Holland, P. L. Dinitrogen Binding and Cleavage by Multinuclear Iron Complexes. *Acc. Chem. Res.* **2015**, *48*, 2059−2065.

(14) Li, Y.; Li, Y.; Wang, B.; Luo, Y.; Yang, D.; Tong, P.; Zhao, J.; Luo, L.; Zhou, Y.; Chen, S.; et al. Ammonia Formation by a Thiolate-bridged Diiron amide Complex as a Nitrogenase mimic. *Nat. Chem.* **2013**, *5*, 320−326.

(15) Mittasch, A. Early Studies of Multicomponent Catalysts. *Adv. Catal.* **1950**, *2*, 81−104.

(16) Amar, I. A.; Lan, R.; Petit, C. T. G.; Tao, S. Electrochemical Synthesis of Ammonia Using Fe3Mo3N Catalyst and Carbonate-Oxide Composite Electrolyte. *Int. J. Electrochem. Sci.* **2015**, *10*, 3757−3766.

(17) Montoya, J. H.; Tsai, C.; Vojvodic, A.; Nøskov, J. K. The Challenge of Electrochemical Ammonia Synthesis: A New Perspective on the Role of Nitrogen Scaling Relations. *ChemSusChem* **2015**, *8*, 2180−2186.

(18) Kyriakou, V.; Garagounis, I.; Vasileiou, E.; Vourros, A.; Stoukides, M. Progress in the Electrochemical Synthesis of Ammonia. *Catal. Today* **2017**, *286*, 2−13.

(19) Wang, X.; Yin, J.; Xu, J.; Wang, H.; Ma, G. Chemical Stability, Ionic Conductivity of BaCe0.9−xZrxSm0.10O3−α and Its Application to Ammonia Synthesis at Atmospheric Pressure. *Chin. J. Chem.* **2011**, *29*, 1114−1118.

(20) Amar, I. A.; Lan, R.; Tao, S. Synthesis of Ammonia Directly from Wet Nitrogen Using a Redox Stable La0.75Sr0.25Cr0.5-Fe0.5O3−δ−Ce0.8Gd0.18Ca0.02O2−δ Composite Cathode. *RSC Adv.* **2015**, *5*, 38977−38983.

(21) Amar, I. A.; Lan, R.; Petit, C. T. G.; Arrighi, V.; Tao, S. W. Electrochemical Synthesis of Ammonia Based on a Carbonate-oxide Composite Electrolyte. *Solid State Ionics* **2011**, *182*, 133−138.

(22) Abghoui, Y.; Garden, A. L.; Hlynsson, V. F.; Björgvinsdóttir, S.; Ólasfdóttir, H.; Skúlason, E. Enabling Electrochemical Reduction of Nitrogen to Ammonia at Ambient Conditions through Rational Catalyst Design. *Phys. Chem. Chem. Phys.* **2015**, *17*, 4909−4918.

(23) Azofra, L. M.; Li, N.; MacFarlane, D.; Sun, C. H. Promising Prospects for 2D d2−d4M3C2 Transition Metal Carbides (MXenes) in N2 Capture and Conversion into Ammonia. *Energy Environ. Sci.* **2016**, *9*, 2545−2549.

(24) Jacobsen, C. J. H.; Dahl, S.; Clausen, B. S.; Bahn, S.; Logadottir, A.; Norskov, J. K. Catalyst Design by Interpolation in the Periodic Table: Bimetallic Ammonia Synthesis Catalysts. *J. Am. Chem. Soc.* **2001**, *123*, 8404−8405.

(25) Kojima, R.; Aika, K. Cobalt Molybdenum Bimetallic Nitride Catalysts for Ammonia Synthesis—Part 1. Preparation and Characterization. *Appl. Catal., A* **2001**, *215*, 149−160.

(26) Kojima, R.; Aika, K. Cobalt Molybdenum Bimetallic Nitride Catalysts for Ammonia Synthesis—Part 2. Kinetic Study. *Appl. Catal., A* **2001**, *218*, 121−128.

(27) Yandulov, D. V.; Schrock, R. R. Catalytic Reduction of Dinitrogen to Ammonia at a Single Molybdenum Center. *Science* **2003**, *301*, 76−78.

(28) Liu, N.; Nie, L.; Xue, N.; Dong, H.; Peng, L.; Guo, X.; Ding, W. Catalytic Ammonia Synthesis over Mo Nitride/ZSM-S. *ChemCatChem* **2010**, *2*, 167−174.

(29) Zeinalipour-Yazdi, C. D.; Hargreaves, J. S. J.; Catlow, C. R. A. DFT-D3 Study of Molecular N2 and H2 Activation on Co3Mo3N Surfaces. *J. Phys. Chem. C* **2016**, *120*, 21390−21398.

(30) Wang, P.; Chang, F.; Gao, W.; Guo, J.; Wu, G.; He, T.; Chen, P. Breaking Scaling Relations to Achieve Low-temperature Ammonia Synthesis through LiH-mediated Nitrogen Transfer and Hydrogenation. *Nat. Chem.* **2017**, *9*, 64−70.

(31) Liu, H. Z. *Ammonia Synthesis Catalysts: Innovation and Practice.* Chemical; Industry Press: Beijing, 2013.

(32) Abe, H.; Cheung, T. K.; Bell, A. T. Catalytic Hydrotreating of Indole, Dibenzothiophene, and Benzofuran over Mo2N. *Catal. Lett.* **1993**, *21*, 11.

(33) Xie, J.; Xie, Y. Transition Metal Nitrides for Electrocatalytic Energy Conversion: Opportunities and Challenges. *Chem. - Eur. J.* **2016**, *22*, 3588−3598.

(34) Zhao, Y.; Kamiya, K.; Hashimoto, K.; Nakanishi, S. In Situ CO2-Emission Assisted Synthesis of Molybdenum Carbonitride Nanomaterial as Hydrogen Evolution Electrocatalyst. *J. Am. Chem. Soc.* **2015**, *137*, 110−113.

(35) Wang, S.; Ge, H.; Sun, S.; Zhang, J.; Liu, F.; Wen, X.; Yu, X.; Wang, L.; Zhang, Y.; Xu, H.; et al. A New Molybdenum Nitride Catalyst with Rhombohedral MoS2 Structure for Hydrogenation Applications. *J. Am. Chem. Soc.* **2015**, *137*, 4815−4822.

(36) Zhang, B.; Cui, G.; Zhang, K.; Zhang, L.; Han, P.; Dong, S. Molybdenum Nitride/Nitrogen-doped Graphene Hybrid Material for Lithium Storage in Lithium Ion Batteries. *Electrochim. Acta* **2014**, *150*, 15−22.

(37) Chen, W. F.; Iyer, S.; Sasaki, K.; Wang, C.; Zhu, Y.; Muckerman, J. T.; Fujita, E. Biomass-derived Electrocatalytic Composites for Hydrogen Evolution. *Energy Environ. Sci.* **2013**, *6*, 1818−1826.

(38) Das, S.; Kim, M.; Lee, J.; Choi, W. Synthesis, Properties, and Applications of 2-D Materials: A Comprehensive Review. *Crit. Rev. Solid State Mater. Sci.* **2014**, *39*, 231−252.

(39) Wang, Y.; Wang, S.; Lu, Y.; Jiang, J.; Yang, S. A. Strain-Induced Isostructural and Magnetic Phase Transitions in Monolayer MoN2. *Nano Lett.* **2016**, *16*, 4576−4582.

(40) Kohn, W.; Sham, L. M. Self-Consistent Equations Including Exchange and Correlation Effects. *Phys. Rev.* **1965**, *140*, A1133−A1138.

(41) Hammer, B.; Hansen, L. B.; Nørskov, J. K. Improved Adsorption Energetics within Density-Functional Theory using Revised Perdew-Burke-Ernzerhof Functionals. *Phys. Rev. B: Condens. Matter Mater. Phys.* **1999**, *59*, 7413−7421.

(42) Kresse, G.; Joubert, D. From Ultrasoft Pseudopotentials to the Projector Augmented-Wave Method. *Phys. Rev. B: Condens. Matter Mater. Phys.* **1999**, *59*, 1758−1775.

(43) Goerigk, L.; Grimme, S. A General Database for Main Group Thermochemistry, Kinetics, and Noncovalent Interactions − Assessment of Common and Reparameterized (meta-)GGA Density Functionals. *J. Chem. Theory Comput.* **2010**, *6*, 107−126.

(44) Zeinalipour-Yazdi, C. D.; Hargreaves, J. S. J.; Catlow, C. R. A. Nitrogen Activation in a Mars−van Krevelen Mechanism for Ammonia Synthesis on Co3Mo3N. *J. Phys. Chem. C* **2015**, *119*, 28368−28376.

(45) Abghoui, Y.; Garden, A. L.; Howalt, J. G.; Vegge, T.; Skúlason, E. Electroreduction of N2 to Ammonia at Ambient Conditions on Mononitrides of Zr, Nb, Cr, and V: A DFT Guide for Experiments. *ACS Catal.* **2016**, *6*, 635−646.

34

(46) Li, X.; Li, Q.; Cheng, J.; Liu, L.; Yan, Q.; Wu, Y.; Zhang, X.; Wang, Z.; Qiu, Q.; Luo, Y. An Fe-N2 Complex That Generates Hydrazine and Ammonia via Fe=NNH2: Demonstrating a Hybrid Distal-to-Alternating Pathway for N2 Reduction. *J. Am. Chem. Soc.* **2016**, *138*, 8706−8709.

(47) Azofra, L. M.; Sun, C.; Cavallo, L.; MacFarlane, D. R. Feasibility of N2 Binding and Reduction to Ammonia on Fe-Deposited MoS2 2D Sheets: A DFT Study. *Chem. - Eur. J.* **2017**, *23*, 8275−8279.

(48) Zhao, J.; Chen, Z. F. Single Mo Atom Supported on Defective Boron Nitride Monolayer as an Efficient Electrocatalyst for Nitrogen Fixation: A Computational Study. *J. Am. Chem. Soc.* **2017**, *139*, 12480−12487.

(49) Zhou, F.; Azofra, L.; Al-Agele, M.; Kar, M.; Simonov, A.; McDonnell-Worth, C.; Sun, C.; Zhang, X.; MacFarlane, D. Electrosynthesis of Ammonia from Nitrogen at Ambient Temperature and Pressure in Ionic Liquids. *Energy Environ. Sci.* **2017**, No. 10.1039/C7EE02716H, DOI: 10.1039/C7EE02716H.

Chapter 4 FeB$_x$ Nanosheet as NRR Catalyst

4.1 Overview

Based on the studies of graphene- and MoN$_2$-based catalysts, it is established that catalyst performance is strongly affected by the coordination of active sites, like lowly coordinated carbon (Chapter 2) and vacancies in MoN$_2$ (Chapter 3). This chapter will continue the coordination investigation on NRR performance, focusing on iron (Fe), another promising metal.

Boron has been selected to mediate the coordination number (CN) of iron, as Fe-B bonding can form various compounds with different CNs, such FeB, FeB$_2$, FeB$_6$, etc. Another reason to choose boron is the high performance of boron itself as recently reported, but N$_2$-B is not strong. Therefore, a hypothesis that Fe-B combination may lead to novel synergetic effect has been proposed in this work. To clarify it, systematic investigation of full NRR over Fe- and B-sites of Fe-B compounds, including FeB, FeB$_2$, FeB$_6$(α) and FeB$_6$(β), has been performed and presented in this chapter. The following conclusions have been obtained: (i) FeB$_6$(β) has been identified as the best candidate among these four with lowest ΔGmax (0.28 eV), even performing better than single-Ru catalysts (0.42 eV); (ii) lightly oxidized iron has been identified as active sites NRR; and (iii) hypercoordinated iron performs better than lowly-coordinated cases.

This work has been published on Journal of Materials Chemistry A titled as "Exploration of iron borides as electrochemical catalysts for the nitrogen reduction reaction" by Qinye Li, Chuangwei Liu, Siyao Qiu, Fengling Zhou, Lizhong He, Xiwang Zhang, Chenghua Sun. (*J. Mater. Chem. A* 7, 21507-21513 (2019)).

Exploration of iron borides as electrochemical catalysts for nitrogen reduction reaction

Qinye Li,[a] Chuangwei Liu,[b] Siyao Qiu,[c] Fengling Zhou,[c] Lizhong He,[a] Xiwang Zhang,[*a] and Chenghua Sun[*cd]

In recent years, boron (B) has been identified as p-block catalysts for nitrogen reduction reaction (NRR), but N_2 adsorption on B-site is often weak. In this report, iron has been introduced to improve N_2 fixation. Four iron borides, including FeB, FeB_2, $FeB_6(\alpha)$, and $FeB_6(\beta)$, have been explored as potential NRR catalysts under the framework of density functional theory (DFT). The key hypothesis is that Fe and B, both as active sites, may offer synergetic effect in N_2 fixation and reduction. As demonstrated by our calculations, $FeB_6(\beta)$ offers the best performance in terms of lowest maximum energy required for elementary steps (0.68 eV), which is close to recently reported single-atom catalysts. Following this computational work, lightly oxidized iron has been identified as active sites for the electrochemical synthesis of ammonia at room temperature.

Introduction

Over the last century, ammonia (NH_3) synthesis through nitrogen reduction reaction (NRR) has been extensively studied because of its paramount significance in both catalysis science and modern chemical and agriculture industry.[1-3] To date, the Haber-Bosch process, as developed one hundred years ago, is still the dominating approach for large-scaled ammonia synthesis.[3] Although nitrogen reduction by hydrogen is exothermic, the Haber-Bosch production needs high temperature and high pressure to achieve optimum kinetics, which is not energy efficient and brings large amount of carbon emission because hydrogen is often produced from hydrocarbon reforming.[4,5] Under this context, electrochemical synthesis, ideally at room temperature, has been extensively studied as a green technology for ammonia production.[6-16]

For NRR, one of the key challenges is the activation of nitrogen, which is highly stable due to the strong N≡N bond. Therefore, large amount of energy input is required to inject electrons to the antibonding states of nitrogen, under which its bond order can be reduced based on molecular orbital theory. Following this understanding, highly active metals, like lithium and potassium, are often employed for traditional Haber-Bosch process, but they are not applicable for aqueous electrochemical conditions. In recent years, single-atom catalysts (SACs)[17] have been emerged as a new strategy

to design high performance electrocatalysts and successfully employed for NRR.[18-25] For such designs, single atom is loaded on nanosheets as the active centre for N_2 fixation and reduction, such as Mo/BN,[19] Fe/MoS_2,[20] Fe/graphene,[24] etc. These SACs are promising to catalyze NRR with low energy input at room temperature. However, an open challenge is how to achieve high stability of catalysts for a long durability which is particularly difficult when high loading of dispersed metals is expected.[26,27] Another challenge comes from the reaction with the solution as NRR needs large amount of protons and electrons; consequently, single metals loaded on typical substrates may react and dissolve into the solution. Ideally, metals are not only highly dispersed to achieve high catalysis performance but also strongly stabilized by the substrate to confer high stability. These two requirements demand delicate control for SACs because they are highly sensitive to local coordination. For instance, $Fe-N_4$ performs much worse than $Fe-N_3$ when single Fe is deposited on carbon vacancies of graphene.[18]

Different from metal-based SACs, non-metals offer high stability in aqueous solution. Especially boron has empty orbitals to accept lone pairs from N_2 but also can generate B-to-N π-back bonding, leading to N_2 activation.[28-36] Most recently, boron loaded on 2D substrates has been particularly identified as promising single non-metal catalyst, offering high energy efficiency and ammonia selectivity.[32] However, sole boron site fails to provide strong capacity to adsorb N_2.[25-27] Therefore, this work aims to explore Fe-B as NRR catalyst, using iron to strengthen N_2 adsorption. Iron borides (FeB, FeB_2) were employed as starting point to establish essential knowledge for the exploration of new Fe-B catalysts because (i) both FeB and FeB_2 are industrially available, and if confirmed as promising catalysts, scaling up is feasible; and (ii) high stability and high loading of active sites may be achieved at the same time. As demonstrated below, hypercoordinated iron in FeB_6 is promising.

a. School of Chemical Engineering, Monash University, Clayton, Victoria 3800, Australia. E-mail: xiwang.zhang@monash.edu
b. School of Chemistry, Faculty of Science, Monash University, Clayton, Victoria 3800, Australia
c. Science & Technology Innovation Institute, Dongguan University of Technology, Dongguan, China
d. Department of Chemistry and Biotechnology, and Centre for Translational Atomaterials, FSET, Swinburne University of Technology, Hawthorn, Victoria 3122, Australia. E-mail: chenghuasun@swin.edu.au
†Electronic Supplementary Information (ESI) available: theoretical framework, analysis of other Conceptual DFT properties, and additional figures. See DOI: 10.1039/x0xx00000x

Computational Methods

In this work, all calculations were carried out under standard density functional theory using the Vienna Ab initio Simulation Package (5.4.4 VASP) under the generalized gradient approximation with the revised Perdew-Burke-Ernzerhof.[37-39] An energy cut-off of 380 eV was adopted, and the k-space was sampled with a grid of 3×3×1 under the Monkhorst-Pack scheme. Four Fe-B compounds were modelled by the slab of (001) surfaces, over which a vacuum space of 15 Å has been applied. All structures have been fully optimized until the maximum force on each atom was less than 0.01 eV/Å. Zero point energy corrections were calculated over gamma points. The van der Waals interaction has been considered using the DFT-D3 scheme.[40] The calculations of Gibbs free energy for NRR elementary steps were based on the scheme of standard hydrogen electrode, as well described in the literature.[41,42] More tests and lattice parameters for four Fe-B compounds have been listed in the supporting information (Sections 1&2).

Results and Discussion

Fig. 1(a)-(b) show bonding networks for FeB and FeB_2. For FeB, both Fe and B show two sets of Fe-B coordination structures, labelled as Fe_{6c}, Fe_{5c}, B_{6c} and B_{5c}, while FeB_2 is relatively simple, only showing Fe_{6c} and B_{3c}. Such bonding structures directly affect the charge distributions, as indexed by Bader charges in Table 1. It is interesting to see that the charges on Fe_{6c} in FeB_2 and FeB are remarkably different. Specifically, Fe-atoms in FeB are co-mediated by Fe and B (see Fig. 1); as a result, valence electrons from Fe-site are shared with other Fe-atoms, showing metallic nature, low oxidation and relatively large Fe-B distance (1.99-2.18 Å). While FeB_2 shows a different bonding network, with shorter Fe-B bondlength (1.88 Å) and high oxidation state, which difference is very informative, highlighting the strategy that Fe-Fe and B-B bonding can be employed to mediate Fe-site. This knowledge is helpful for further exploration of ideal Fe-state to achieve optimum NRR performance.
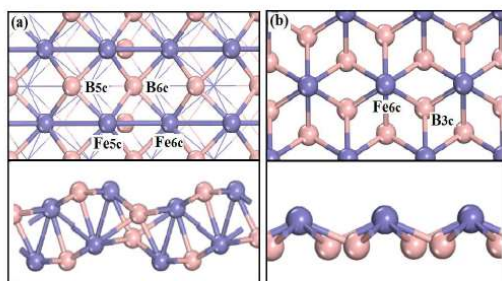
Figure 1. Slab models for FeB and FeB_2. (a) top and side views of FeB; (b) top and side views of FeB_2. Fe and B are shown as purple and pink spheres, respectively.
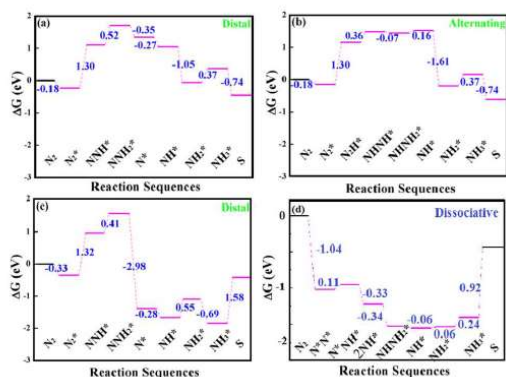
Table 1. Coordination, Bader charge, spin and calculated ΔGmax for four catalysts.

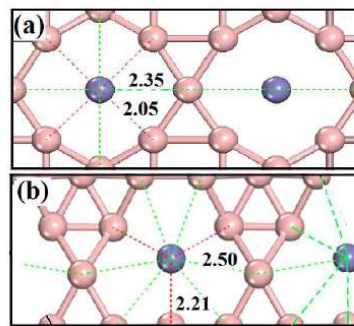| Catalyst	Coordination	Charge(e)	ΔGmax(eV)
FeB	Fe_{6c}	0.42	
	Fe_{5c}	0.47	1.30
	B_{6c}	-0.40	
	B_{5c}	-0.43	
FeB_2	Fe_{6c}	0.18	0.92
	B_{3c}	-0.09	
$FeB_6(\alpha)$	Fe_{5c}	0.53	1.02
	$B_{6c}(x)$	-0.07	
	$B_{6c}(y)$	+0.35	
	B_{5c}	-0.15	
$FeB_6(\beta)$	Fe_{5c}	0.31	0.68
	B_{6c}	-0.20	
	B_{5c}	-0.08	

For NRR, we start calculations from N_2 adsorption. In principle, N_2 may adsorb over Fe- and B-sites, over top-site, Fe-B bridging site, enzymatic and dissociative geometries, which have been tested and listed in the supporting information (Sections 3&4). It is found that: (i) For all these structures, N_2 adsorption on Fe-centre is favourable, confirming that Fe-adding to B-based catalyst is beneficial for N_2 fixation; (ii) enzymatic adsorption is not favourable in all cases; (iii) FeB_2 shows excellent capacity to dissociate N_2 and N_2H over Fe-site, underlining the need to consider dissociative NRR path over FeB_2. Clearly, FeB and FeB_2 present different capacity in N_2 fixation. For Fe with higher oxidized state (e.g., FeB), lone pairs from N_2 may fill its empty states, which can stabilize adsorbed N_2, together with valence electron transferring from Fe_{3d} to antibonding states of N_2. In the case of N_2-adsorption on FeB (Fe_{5c} shows +0.47), BE(N_2)=-0.48 eV has been obtained. At the same time Fe-Fe distance has been enlarged from 2.63 Å to 2.73 Å, indicating that the transferred electrons are partially contributed from Fe-Fe bonds. While for FeB_2, Fe shows lower oxidation (+0.18), being consistent with lower BE(N_2)=0.37 eV. Differently, N_2 dissociative adsorption is favourable, leading to BE(N_2)=-0.97 eV and different NRR path as described below. The calculated charge also indicates that only a part of Fe valence electrons are allocated to Fe-B bonding, while the left results in Fe-Fe interaction in FeB_2 layer, showing metallic features. Such active states play key roles for N_2 dissociative adsorption. The above knowledge highlights the importance of Fe-Fe interaction in the mediation of Fe-centred catalysts.

To establish a full evaluation of catalysis performance, Fig. 2 shows the calculated free energy change ΔG for elementary steps over Fe-sites, with different reaction paths (Dissociation path has been particularly considered for FeB$_2$), while enzymatic path is ignored as such adsorption is not stable based on our tests. Calculated maximum free energy change (ΔGmax) for elementary steps can be derived from the profile. Accordingly, the following features can be summarized: (i) the most favourable NRR path on FeB and FeB$_2$ will be Alternating and Dissociative path, respectively, with ΔGmax=1.30 eV and 0.92 eV, respectively; (ii) For association mechanisms, FeB performs much better than FeB$_2$, with Fe$_{5c}$ in FeB showing the best performance; (iii) For FeB$_2$, dissociative path not only leads to favourable N$_2$ adsorption (-0.97 eV for dissociative adsorption vs -0.29 eV for molecular adsorption), but also favours NH$_2$ dissociation and NH$_3$ release; and (iv) for associative NRR process on FeB$_2$, both initial hydrogenation (N$_2$ → N$_2$H) and final NH$_3$ release are difficult (ΔG>0.9 eV), which can hardly co-exist due to the linear relationship:[43,44] high energy required for NH$_3$ release often means strong Fe-N bonding, resulting in effective N$_2$ activation due to electron injection from Fe-centre to N$_2$. Therefore, it is worth to compare the final geometries for N* and NHx* species, as discussed later. Another interesting result is the remarkable difference of E(N*) on Fe-site: it is quite negative on FeB$_2$ (<-1.0 eV), but very positive on FeB (>1.0 eV), indicating that Fe-B bonding can remarkably affect Fe-N interaction. In the case of FeB$_2$, however, dissociative path has no such strong N*-adsorption issue as N* turns to NH* adsorbed on the top of single Fe-site, rather than on the hole of three Fe-sites. In the literature, E(N*) has been widely employed as an indicator for the design of NRR catalysts, using Ru(0001) as a reference.[45,46] Specifically, an ideal E(N*) would be around -0.46 eV using Ru(0001) as a reference[47]; therefore, we may further optimize the NRR performance of Fe-B system through the searching of new Fe-B compounds.

Figure 3. Models and bonding network for (a) FeB$_6$(α) and (b) FeB$_6$(β). Numbers along red and green dashed lines show Fe-B$_{5c}$ (short) and Fe-B$_{6c}$ (long) bonds in unit of Å.
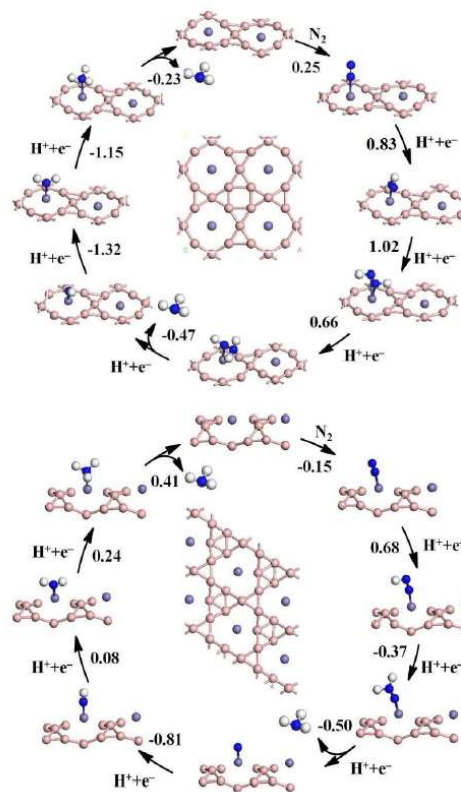
Figure 4. Calculated free energy profiles for NRR on Fe-site for FeB$_6$(α, top) and FeB$_6$(β, bottom). Fe, B, N and H are shown as purple, pink, blue and white spheres. Calculated ΔG for each elementary step is listed in unit of eV. Proton and electrons are labelled as (H$^+$+e$^-$).

Figure 2. Calculated free energy profiles for NRR on FeB and FeB$_2$. (a)&(b) Fe$_{5c}$ site of FeB; and (c)&(d) Fe$_{6c}$ site of FeB$_2$. Distal Alternating, Dissociative indicate the reaction paths. Calculated data of ΔG are labelled for elementary steps in unit of eV.

A direct approach to tune Fe-B interaction is to change the Fe/B atomic ratio. In the literature, two-dimensional Fe-B compounds have been explored by several groups[48,49] and two structures, namely FeB$_6(\alpha)$ and FeB$_6(\beta)$, have been identified as stable configurations, as shown in Fig. 3(a) and (b), in which Fe is hypercoordinated by 8 and 9 boron-atoms in α and β, respectively, but Fe-B distances are different as labelled. Based on the understanding established from FeB and FeB$_2$, the hypercoordination in FeB$_6$ can keep N$_2$-fixation capacity, but it is not clear how differentiated Fe-B bonding and newly introduced B-B interaction would change the catalysis performance. The charges on Fe- and B-site have been calculated and listed in Table 1, according to which Fe-charge in α is remarkably higher than that in FeB and FeB$_2$, but Fe$_{5c}$ in β is between that FeB and FeB$_2$, which offers the opportunity to investigate how this charge difference can be tuned to improve final NRR performance.

To examine NRR performance, full free energy profiles have been calculated for FeB$_6$ structures, as shown in Fig. 4, together with intermediate states and calculated ΔG for each step involved in the favorable reaction paths. According to this result, we found: (i) FeB$_6(\alpha)$ and FeB$_6(\beta)$ show $\Delta Gmax$=1.02 eV and 0.68 eV, respectively; (ii) Alternating and Distal mechanisms are favorable for FeB$_6(\alpha)$ and FeB$_6(\beta)$, respectively; (iii) NH$_3$ release has been remarkably improved with respect to FeB and FeB$_2$, and potential-determining step comes from early hydrogenation, N$_2$H$\rightarrow$N$_2$H$_2$ for FeB$_6(\alpha)$ and N$_2$$\rightarrow$N$_2$H for FeB$_6(\beta)$. Clearly, NH$_3$ release issue has been solved with such hypercoordinated Fe-B system, and the overall performance has also been improved, with FeB$_6(\beta)$ being identified as the best candidate ($\Delta Gmax$=0.68 eV).

To understand the performance difference among four catalysts, geometry and performance indicators are related for analysis. Fig. 5(a) shows three indicators (-$\Delta Gmax$, E(N), E(N$_2$)) versus the coordinator numbers for FeB, FeB$_2$ and FeB$_6$. Ideally, -$\Delta Gmax$ can be close to zero (dash line) so that almost no energy input will be requested for NRR. It is found that hypercoordinated FeB$_6$ (β) offers the best performance. As boron is well known as electron-deficient element, Fe$_{3d}$ electrons are partially shared by neighbouring boron; as a result, electron injection from Fe to N$_2$ is reduced, weakening Fe-N bonding. The −$\Delta Gmax$ versus E(N) can be further revealed by the famous volcano curve, as shown in Fig. 5(b), in which Ru(0001) and Fe(111) have been employed for comparison.[46] For FeB and FeB$_2$, active sites are indicated in the parentheses, while for FeB$_6$, α and β show the phase difference with Fe as active site. The curve shows that (i) FeB$_2$(Fe-site) slightly deviates from the linear relationship; and (ii) FeB$_6(\beta)$ is better than pure Fe and is close to noble metal Ru, suggesting that it is a promising catalyst for NRR.

There are still several unsolved questions. The first is why FeB$_2$ performs so different for dissociative and associative paths, especially its Distal path is much worse than that for FeB and FeB$_6$. For associated path on FeB$_2$, a remarkable difference is that N* (generated after releasing the first NH$_3$) turns from single- to three-coordinated with the catalyst, fixed by three Fe-atoms (initial Fe-atom to fix N$_2$ is labelled as Fe^1, and other two as Fe^2 in Fig. 6(a)); as

a result, strong Fe-N bonding has been resulted as indicated by the heavy charged N*, which is the reason for the large ΔG associated with the 2nd NH$_3$ release (1.58 eV, see Fig. 2(c)). While for dissociative adsorption, N* has been converted to NH* prior to Fe$_3$-N formation, avoiding the difficult NH$_3$ release and achieving $\Delta Gmax$=0.92 eV. Therefore, Fe$_3$-N bonding should be avoided, as it remarkably increases the energy input for NH$_3$ release.
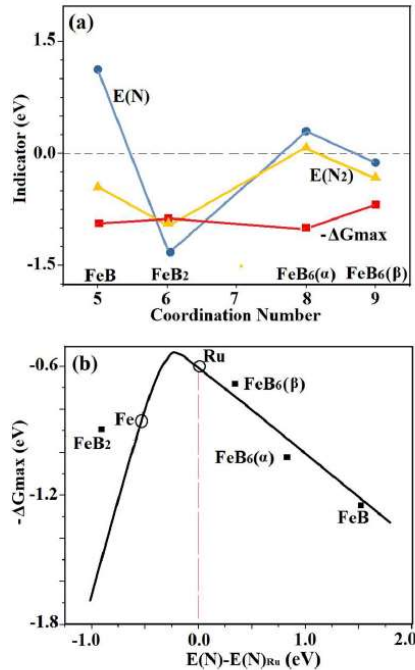

Figure 5. Structure-performance relationship. (a) Performance indicator versus coordination number; and (b) Volcano curve for −$\Delta Gmax$ versus E(N).

Second question is the poor performance of FeB in initial hydrogenation, from N$_2$*$\rightarrow$N$_2$H* (see Fig. 2). To answer this, Bader charge states for S, N$_2$* and N* have been listed in Table 2. The charge of Fe bonded with N$_2$ and N almost has no change (+0.44) with a typical Fe-N bondlength (1.54 Å); moreover, the net charge on N$_2$* is only -0.22, which is notably smaller than that on FeB$_6(\beta)$, indicating that N$_2$ has not been effectively activated. It is also worth to note that NH$_3$ release is not difficult on FeB, although E(N) is particularly large, indicating that NH$_3$ instability comes from other reasons. Fig. 6(b) shows the bonding network when N* is generated, in which a key change is the distance between active Fe and bottom B, enlarging from 2.13 Å to 2.28 Å. As volcano curve essentially origins from the linear relationship of adsorption energies of intermediate states, with the basic assumption that these states are linked by a common surface bond (e.g., NH* and N* share the same N-catalyst bond). When the basic bonding associated with the active site on the catalyst has been changed, such relationship

can be broken, which is why FeB(Fe) still shows a relatively small ΔG_{max} when large E(N) is presented.

Final question is why FeB$_6$(β) shows much better performance than the other three, especially FeB$_6$(α) also shows similar hypercoordination feature with β-phase. The difference between these two can be found from the Fe-charge of clean surface: α shows Fe$^{0.53}$ based on Bader charge, while β shows Fe$^{0.36}$, indicating a lower oxidation state of Fe in β-phase. As a result, newly introduced oxidizing agent, N$_2$, can obtain electrons and get activated on FeB$_6$(β), but difficult to do the same on FeB$_6$(α). This confirms our hypothesis that lightly oxidized iron is beneficial for NRR, following which rational design of ligands environment can further improve the performance of Fe-site. Recently, similar phenomenon has been found for Mo-based SACs,[23,50] in which lightly oxidized Mo has been identified as promising NRR catalysts, performing much better than N-mediated Mo.
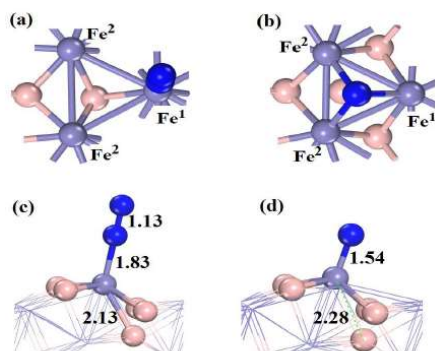

Figure 6. Understanding the performance of FeB$_2$ and FeB. (a) Single-coordinated N$_2$ and (b) three-coordinated N on FeB$_2$, (c) adsorbed N$_2$ and (d) single-coordinated N on FeB. Bond lengths are in unit of Å. Enlarged Fe-B bond (2.13 Å to 2.28 Å) has been highlighted by green dashed line.

Table 2 Charge analysis by Bader population in unit of e. S, N$_2$* and N* represent the states of clean surface, N$_2$- and N-adsorbed geometries. Nx indicates the adsorbed N-species.

Catalyst	Species	S	N$_2$*	N*
FeB	Fe	0.44	0.44	0.45
	N$_x$		-0.22	-0.59
FeB$_2$	Fe	0.18	0.24	0.36
	N$_x$		-0.23	-0.88
FeB$_6$(α)	Fe	0.53	0.46	0.54
	N$_x$		-0.20	-1.80
FeB$_6$(β)	Fe	0.36	0.30	0.30
	N$_x$		-0.22	-0.28

For high performance NRR catalyst, excellent selectivity is essential. To better understand the selectivity, optimized geometries for H*, N$_2$* and co-adsorbed N$_2$*-H* were presented in Fig. 7, together with HER diagram and calculated binding energy (BE) for these species being shown in Fig. 8. We found that the calculated ΔG(H*) is smaller than ΔGmax for NRR on these four catalysts, according to which NRR selectivity seems to be low in terms of energy. However, it is worth to note that H* adsorption (from H$^+$+e$^-$) is weak with respect to N$_2$ adsorption for all four catalysts, as indicated by calculated BE shown in Fig. 8(b). Therefore, active Fe-sites will prefer to be occupied by N$_2$, rather than H-terminals, which is beneficial for NRR. Even these sites are occupied by H-terminals, N$_2$ can still adsorb, pushing H-terminal to bond with neighbouring B or Fe without large energy request, as evidenced by optimized geometries shown in Fig. 7(i-l) and calculated BE in Fig. 8(b).

As described above, N$_2$-adsorption over H-terminated Fe can push H to neighbouring site, leading to H* co-stabilized by Fe-B or multiple Fe-sites, as shown in Fig. 7. Among these four, FeB is particularly interesting as N$_2$ adsorption on H-terminated Fe is even stronger than that on non-H-terminated case. Specifically, BE(N$_2$) is increased from -0.48 eV (without H-terminals) to -0.78 eV (with H-terminal), corresponding to the geometries in Fig. 7(e) and (i). To understand this result, Bader charges on Fe-site over which N$_2$*, H* and N$_2$*-H* are adsorbed has been calculated. In the clean case, Fe shows a charge state of +0.44, which has been no change after N$_2$ adsorption, suggesting that N$_2$ adsorption is dominated by the N$_2$-metal coordination, rather than Fe-N bonding. After H-adsorption, Fe-H bonding is generated through Fe→H electron transfer, as supported by the negative charge on H (-0.20). Associated with following N$_2$ adsorption, H-terminal has been pushed to neighbouring B, being co-stabilized by Fe and B and leading to new charge states, with Fe(+0.32), H(-0.39) and N$_2$(-0.22). Compared with the non-H-termination case, the charge on N$_2$ has no change (-0.22), but H gains more electrons from B, rather than Fe, corresponding to B-H formation and slightly weakened Fe-H bonding. Clearly, strengthened N$_2$ adsorption over H-terminated Fe-site can be viewed as a result of joint actions by weakened Fe-H bonding, newly introduced B-H bonding and strengthened N$_2$-Fe coordination. Therefore, the stability of H-termination after N$_2$ adsorption is critical, which can be affected by several factors, like Fe-B distance (which is key for Fe-B co-stabilized H*) and Fe-Fe distance (for H* over multiple Fe-sites). According to this unusual result, it appears that N$_2$ adsorption, as the starting point for NRR, can be complicated and deserves better understanding, given current researches often consider HER and NRR separately, which may miss key information regarding N$_2$*-H* co-adsorption and the evolution of surface geometries (like H* moves from the top of Fe to be co-stabilized by Fe-B or Fe-Fe, as shown in Fig. 7(i)-(l)).
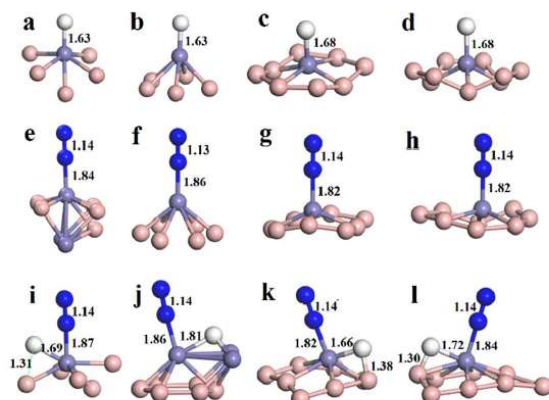
Figure 7 Optimized geometries for H*, N$_2$* and N$_2$*-H* on four catalysts, with (a,e,i) on FeB, (b,f,j) on FeB$_2$, (c, g, k) on FeB6(alpha) and (d, h, l) on FeB6(beta). Fe, B, N and H are shown as purple, pink, blue and white spheres.
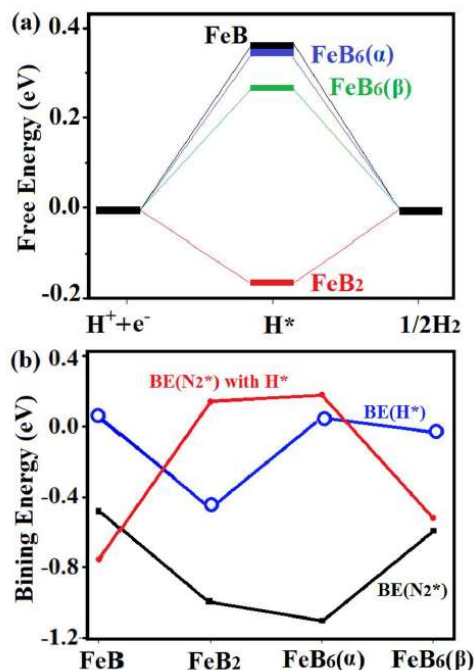
Figure 8 H-termination. (a) HER diagram; (b) Binding energies for H and N$_2$ on clean and H-terminated Fe-site.

Conclusions

In summary, we proposed Fe-B concept catalysts, demonstrated by industrially available FeB together with newly predicted FeB$_2$, FeB$_6$(α) and FeB$_6$(β) as examples. DFT calculations suggest that (i) FeB$_6$(β) is a promising NRR catalyst with ΔGmax=0.68 eV over Fe-site; (ii) lightly oxidized Fe-site has been identified as active sites for NRR; and (iii) metal-metal and B-B interaction can play an important role to optimize the catalysis performance of Fe-B compounds catalysts. It is worth to mention that the above performance was obtained from bulk or 2D materials, not by SACs; therefore, the loading of active sites can be very high (e.g., FeB$_6$(β), Fe-density is ~5/nm^2 and 46.3 wt%). Moreover, Fe-atoms have been effectively separated and hypercoordinated by boron network; as a result, they can perform like SACs while presenting high stability and density. We anticipate that this work will stimulate further interest in the design of high performance NRR catalysts to address the key challenges for NH$_3$ economy.

Conflicts of interest

The authors declare no competing financial interest.

Acknowledgements

References

1 K. Tamaru. Catalytic ammonia synthesis. Plenum Press: New York 1991.
2 R. Schlögl. Ammonia synthesis. Wiley Online Library, 2008.
3 T. Kandemir, et al. *Angew. Chem. Int. Ed.* **52**, 12723 (2013);
4 J.W. Erisman, et al. *Nature Geosci* **1**, 636 (2008).
5 J.G. Chen, et al. *Science* 360, 873 (2018).
6 L.M. Azofra, N. Li, D. MacFarlane, C.H. Sun. *Energy Environ. Sci.* 2016, **9**, 2545-2549.
7 D. Bao, Q. Zhang, F.-L. Meng, H. Zhong, M. Shi, Y. Zhang, J. Yan, Q. Jiang, X. Zhang, *Adv. Mater*. 2017, **29**, 1604799.
8 F. Zhou, L. M. Azofra, M. Ali, M. Kar, A. N. Simonov, C. McDonnell-Worth, C. Sun, X. Zhang and D. R. MacFarlane, *Energy Environ. Sci.*, 2017, **10**, 2516-2520.
9 Q. Li, L. He, C. Sun and X. Zhang, *J. Phys. Chem. C*, 2017, **121**, 27563-27568.
10 C. Guo, J. Ran, A. Vasileff and S.-Z. Qiao, *Energy Environ. Sci.*, 2018, **11**, 45-56.
11 Z. Wei, Y. Zhang, S. Wang, C. Wang, J. Ma. *J. Mater. Chem. A*, 2018, **6**, 13790-13796

12 J. Zhao, L. Zhang, X. Xie, X. Li, Y. Ma, Q. Liu, W. Fang, X. Shi, G. Cui, X. Sun. *J. Mater. Chem. A*, 2018, **6**, 24031-24035

13 L. Li, C. Tang, B. Xia, H. Jin, Y. Zheng, S.-Z. Qiao. *ACS Catal.* 2019, **9**, 2902-2908.

14 P. Chen, N. Zhang, S. Wang, T. Zhou, Y. Tong, C. Ao, W. yan, L. Zhang, W. Chu, C. Wu, Y. Xie. *PNAS*, 2019, **116**, 6635-6640.

15 B.H.R. Suranto, H. Du, D. Wang, J. Chen, A.N. Simonov, D.R. MacFarlane. *Nature Catal.* DOI: 10.1038/s41929-019-0252-4.

16 Q. Wang, Y. Lei, D. Wang, Y. Li. *Energy Environ. Sci.* 2019, DOI: 10.1039/C8EE03781G.

17 B. Qiao, A. Wang, X. Yang, L. F. Allard, Z. Jiang, Y. Cui, J. Liu, J. Li and T. Zhang, *Nat. Chem.*, 2011, **3**, 634-641

18 X. Li, Q. Li, J. Cheng, L. Liu, Q. Yan, Y. Wu, X. Zhang, Z. Wang, Q. Qiu and Y. Luo, *J. Am. Chem. Soc.*, 2016, **138**, 8706-8709

19 J. Zhao and Z. Chen, *J. Am. Chem. Soc.*, 2017, **139**, 12480-12487.

20 L.M. Azofra, C. Sun, L. Cavallo, D.R. MacFarlane. *Chem. -Eur. J.* 2017, **23**, 8275-8279.

21 C. Ling, Y. Ouyang, Q. Li, X. Bai, X. Mao, A. Du and J. Wang, *Small Methods*, 2018, **0**, 1800376.

22 X. Zhang, A. Chen, Z. Zhang and Z. Zhou, *J. Mater. Chem. A,* 2018, **6**, 18599-18604.

23 Q. Li, S.Y. Qiu, C.W. Liu, M.G. Liu, L.Z. He, X.W. Zhang, C. Sun. *J. Phys. Chem. C* 2019, **123**, 2347–2352.

24 M. Wang, S. Liu, T. Qian, J. Liu, J. Zhou, H. Ji, J. Xiong, J. Zhong, C. Yan. *Nature Comm.* 2019, **10**, 341

25 C. Liu, Q. Li, J. Zhang, Y. Jin, D. R. MacFarlane, C. Sun. *J. Mater. Chem. A* 2019, **7**, 4771-4776.

26 S. Duan, R. Wang, J. Liu, *Nanotechnol.* 2018, **29**, 204002.

27 B.W. Zhang, Y.X. Wang, S.L. Chou, H.K. Liu, S.X. Dou. *Small Methods*, 2019, DOI: 10.1002/smtd.201800497.

28 C. Ling, X. Niu, Q. Li, A. Du, J. Wang, *J. Am. Chem. Soc.*, 2018, 14161-14168.

29 X. Yu, P. Han, Z. Wei, L. Huang, Z. Gu, S. Peng, J. Ma, G. Zheng. *Joule*, 2018, **2**, 1610-1622.

30 C. Liu, Q. Li, J. Zhang, Y. Jin, D.R. MacFarlane, C. Sun, *J. Phys. Chem. C* 2018, **122**, 25268-25273.

31 J. Deng, C. Liu, *Chem*, 2018, **4**, 1773-1774.

32 C. Liu, Q. Li, C. Wu, J. Zhang, Y. Jin, D. R. MacFarlane, C. Sun, *J. Am. Chem. Soc.* 2019, **141**, 2884-2888.

33 X. Zhang, T. Wu, H. Wang, R. Zhao, H. Chen, T. Wang, P. Wei, Y. Luo, Y. Zhang, X. Sun. *ACS Catal.*, 2019, **9**, 4609-4615.

34 X. Mao, S. Zhou, C. Yan, Z. Zhu, A. Du. *Phys. Chem. Chem. Phys.* 2019, **21**, 1110-1116.

35 S. Ji, Z. Wang, J. Zhao, *J. Mater. Chem. A*, 2019, **7**, 2392-2399.

36 Z. Chen, J. Zhao, L. Yin, Z. Chen, *J. Mater. Chem. A*, 2019, **7**, 13284-13292.

37 W. Kohn and L. J. Sham, Phys. Rev., 1965, **140**, A1133-A1138

38 J. P. Perdew, K. Burke and M. Ernzerhof, *Phys. Rev. Lett.*, 1996, **77**, 3865.

39 G. Kresse and D. Joubert, *Phys. Rev. B*, 1999, **59**, 1758.

40 S. Grimme, J. Antony, S. Ehrlich and H. Kerieg, *Chem. Phys.*, 2010, **132**, 154104.

41 Q. Tang and D.-E. Jiang, *ACS Catal.*, 2016, **6**, 4953-4961.

42 G. Gao, A. P. O'Mullane and A. Du, *ACS Catal.*, 2017, **7**, 494-500.

43 P. Mehta, P. Barboun, F.A. Herrera, J. Kim, P. Rumbach, D.B. Go, J.C. Hicks, W.F. Schneider. *Nature. Catalysis* 2018, **1**, 269-275.

44 E.M. Fer Fernández, P.G. Moses, A. Toftelund, H.A. Hansen, J.I. Martínez, F. Abild-Pedersen, J. Kleis, B. Hinnemann, J. Rossmeisl, T. Bligaard, and J.K. Nørskov. *Angew. Chem. Int. Ed.* 2008, **47**, 4683 –4686.

45 C. J. H. Jacobsen, S. Dahl, B. S. Clausen, S. Bahn, A. Logadottir and J. K. Nørskov, *J. Am. Chem. Soc.*, 2001, **123**, 8404-8405.

46 E. Skúlason, T. Bligaard, S. Gudmundsdóttir, F. Studt, J. Rossmeisl, F. Abild-Pedersen, T. Vegge, H. Jónsson and J. K. Nørskov, *Phys. Chem. Chem. Phys.*, 2012, **14**, 1235-1245.

47 A. Vojvodic, A.J. Medford, F. Studt, F. Abild-Pedersen, T.S. Khan, T. Bligaard, J.K. Nørskov. *Chem. Phys. Lett.* 2014, **598**, 108-122.

48 H. Zhang, Y. Li, J. Hou, K. Tu, Z. Chen. *J. Am. Chem. Soc.* 2016, **138**, 5644-5651.

49 H. Zhang, Y. Li, J. Hou, A. Du, Z. Chen. *Nano Lett.* 2016, **16**, 6124-6129.

50 W. Zhao, L. Zhang, Q. Luo, Z. Hu, W. Zhang, S. Smith, J. Yang. *ACS Catal.* 2019, **9**, 3419-3425.

44

Chapter 5 Mo₂C Nanosheets as NRR Catalyst

5.1 Overview

During the studies of individual catalysts, hydrogen evolution reaction (HER) has been widely found as a major side reaction. In fact, it has been widely concerned as HER competes with NRR, leading to low Faraday efficiency. In addition, stable H-terminals may be generated with HER, in which cases active sites are not available for NRR. Therefore, advanced knowledge of HER and H-terminals are very important for the design of NRR catalysts.

As demonstrated in Chapter 3, Mo is active and offers strong capacity to fix N_2. However, it is also active for HER for its compounds, like carbides and sulphides. This chapter aims to examine HER and NRR on carbides, Mo_2C. The central question is whether Mo_2C is promising for NRR when active HER is occurring. As demonstrated below, it is found: (i) Mo-site will be heavily covered by adsorbed hydrogen (H*); (ii) N_2 can weakly adsorb over H-terminated Mo2C, but NRR performance is poor ($\Delta Gmax>1.5$ eV); and (iii) the reactivity can hardly be improved through iron doping as we achieved in MoN_2. Based on these results, Mo_2C is not recommended for NRR.

This work has been published on Physical Chemistry Chemical Physics titled as "Impact of H-termination on the nitrogen reduction reaction of molybdenum carbide as an electrochemical catalyst" by Qinye Li, Siyao Qiu, Lizhong He, Xiwang Zhang, Chenghua Sun (Phys. Chem. Chem. Phys. 20, 23338-23343 (2018)).

Check for updates

Impact of H-termination on the nitrogen reduction reaction of molybdenum carbide as an electrochemical catalyst

Qinye Li,[a] Siyao Qiu,[b] Lizhong He,[a] Xiwang Zhang 🔟 *[a] and Chenghua Sun 🔟 *[bc]

Transition metal molybdenum (Mo) exhibits a strong capacity to adsorb nitrogen (N_2), but the Mo–N_2 interaction is too strong and thus it is difficult for ammonia (NH_3) to be released from the catalyst surface. Bonding with nonmetals with strong electronegativity is helpful to weaken the Mo–N_2 interaction, while the effect of hydrogen termination on catalyst surfaces needs to be evaluated given that the hydrogen evolution reaction (HER) is a key side reaction. This computational work aims to explore α-molybdenum carbide (Mo_2C, orthorhombic phase) as an electrochemical catalyst for the full nitrogen reduction reaction (NRR). Our density functional theory (DFT) calculations focus on a (100) surface and demonstrate that (i) surface molybdenum and carbon can be terminated by hydrogen *via* the Volmer step and (ii) the NRR can occur on H-terminated $Mo_2C(100)$ with an energy requirement of 1.0–1.4 eV, depending on H-coverage. Although C–Mo bonding can remarkably reduce difficulty in NH_3 release from a Mo-site, H-terminals result in performance deterioration. These results provide new insights into the development of NRR catalysts.

1. Introduction

In nature, nitrogen (N_2) reduction is catalysed by nitrogenases, a type of enzyme widely found in certain bacteria.[1–3] Generally, protein fragments in enzymes play a key role in electron transfer and the mediation of dielectric environment,[4,5] but metal-centres in complex enzyme structures are often directly involved in the catalytic process.[1,2] In the case of nitrogenase, an [FeMo] cofactor is believed to be responsible for the nitrogen reduction reaction (NRR), including electron accepting, N_2 adsorption and reduction.[1–3] Inspired by the success of using nitrogenases in N_2 fixation, Mo-based NRR catalysts have been extensively studied, including metals,[6,7] molecular complexes,[8–10] newly studied two-dimensional (2D) structures[11–13] and single-atom catalysts.[14–17] Mo metal can strongly adsorb N_2, which is helpful to adsorb and activate N_2 gas, but the Mo–N interaction is too strong to release the product NH_3, underlining the need to explore better Mo-based NRR catalysts.

With respect to Mo metal, molybdenum compounds are much more promising for the NRR.[11–17] For instance, single Mo

supported by boron nitride can offer an ultralow overpotential for the NRR, in which strong Mo–N bonding *via* the nitrogen-vacancy plays a key role.[15] Another Mo–N example is 2D MoN_2 nanosheets, which have been predicted as an excellent NRR catalyst with the maximum change of free energies ΔG_{max} involved in NRR elementary steps being only 0.47 eV.[11] However, the limitation is that the potential determining step (PDS) comes from the initial nitrogen adsorption, which cannot be overcome through providing a larger external voltage.[11] Given that the basic strategy to tune the Mo–N interaction is to control the electron transfer from the Mo centre to adsorbed N_2, the relatively weak Mo–N_2 interaction reported in MoN_2 sheets indicates that too many electrons are taken by the host. Recently, the Mo–C structure has been proposed as a novel catalyst for the NRR, offering a small NRR potential (0.54 V);[18] moreover, the PDS comes from the first electrochemical reduction step ($N_2^* \rightarrow N_2H^*$, with * indicating the adsorbed state). Similarly, cubic MoC has been explored as a NRR catalyst with a NRR potential as low as 0.3 V offered by its (111) surface, confirming the value of the Mo–C structure for the NRR.[18]

The above theoretical predictions are encouraging and more efforts should be devoted to the investigation of the potential of Mo–C bonding for the NRR. In particular, hexagonal Mo_2C has been demonstrated as a catalyst for ammonia decomposition, exhibiting the capacity to stabilize NH_x intermediate states.[19] In addition, high-quality single crystals of Mo_2C have been recently synthesized, mainly with (100) as the dominating surface.[20–22] Compared with typical Mo-compounds, three-coordinated surface

[a] School of Chemical Engineering, Monash University, Clayton, VIC 3800, Australia. E-mail: xiwang.zhang@monash.edu; Fax: +61 3 9905 4597; Tel: +61 3 9902 9916
[b] Science & Technology Innovation Institute, Dongguan University of Technology, Dongguan, China
[c] Department of Chemistry and Biotechnology, Swinburne University of Technology, Hawthorn, VIC 3122, Australia. E-mail: chenghuasun@swin.edu.au

23338 | *Phys. Chem. Chem. Phys.*, 2018, **20**, 23338–23343

This journal is © the Owner Societies 2018

carbon is exposed, and this carbon is hypercoordinated (bonded with six neighbouring Mo-atoms) in the bulk, being similar to the central carbon in nitrogenase.[23] The hydrogen evolution reaction (HER) is often a major issue for NRR catalysts.[24–26] In the case of hexagonal Mo_2C, the HER catalysis is excellent,[27] which was also the case for molybdenum sulphide.[28,29] Considering that the HER is the major side reaction for the NRR, and a high Faraday efficiency can be achieved with very limited approaches,[30] the performance of H-terminated structures is closer to the real case. However, most computational predictions for NRR catalysts were often made without considering H-terminals, with surface Mo being directly exposed to the reactants (N_2 and protons), which may overestimate the capacity to fix N_2. Actually, protons under the electrochemical conditions may quickly adsorb on the catalyst surfaces through the Volmer step ($H^+ + e^- \rightarrow H^*$), resulting in H-terminated surfaces and even H_2 release given Mo-based compounds are widely reported as excellent HER catalysts.[24–29] In principle, two effects may directly be caused by H-terminals: (i) the active sites (like unsaturated Mo) may be occupied and thus efficient N_2 fixation cannot happen and (ii) the HER consumes some of the electrons and leads to a low Faraday efficiency for the NRR, both of which are harmful for the NRR. Therefore, a full consideration of the HER is essential for the evaluation of NRR catalysts. This work aims to study this topic using α-Mo_2C as a model catalyst considering that the experimental validation of the results is feasible as high-quality Mo_2C crystals are available experimentally.[20–22] As demonstrated below, H-terminals can form on the surface easily, which affects NRR performance remarkably.

2. Computational details

$Mo_2C(100)$ is modelled with a $(2 \times 2 \times 1)$ supercell with five Mo_2C layers along the c-direction, as shown in Fig. 1. Over the slab, a vacuum of 13 Å has been employed and intermediate states associated with the HER and NRR are introduced to the surface. Catalysis has been investigated by calculating the free energy change ΔG for each elementary reaction, including N_2 adsorption, six-step N_2 reduction and final NH_3 release, labelled ΔG_i for step i = 1–8 and the PDS has been identified from the maximum ΔG, defined as $G_{max} = \text{Max}\{\Delta G_i\}$ with i = 1–8, as described in the literature.[31–33] The clean (100) surface contains six active sites, including two carbon atoms (outmost) and four molybdenum atoms (sublayer).
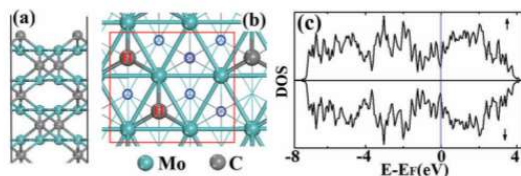

Fig. 1 Computational model of $Mo_2C(100)$. (a) Side view of the slab; (b) top view (red line indicates the supercell used for the calculation; red H and blue circles show potential H- and N_2-adsorption sites); (c) calculated density of states (arrows show spin up and spin down).

Spin-polarized density functional theory (DFT) calculations were performed under the scheme of generalized gradient approximation (GGA) using the revised Perdew–Burke–Ernzerhof (RPBE) functional, as embedded in the Vienna ab initio simulation package (VASP 5.4.4).[34–37] Plane waves with a kinetic energy of 380 eV have been used, together with the use of ultrasoft pseudopotentials for all elements except hydrogen. The DFT-D3 scheme[38] has been employed to correct the van der Waals interaction. All optimizations were converged with a force of less than 0.02 eV Å^{-1} and energy change less than 10^{-3} eV. A $3 \times 3 \times 1$ Monkhorst–Pack k-points sampling has been employed for all surfaces. The N_2-adsorption energy (AE) on the catalyst surface (S) has been calculated by

$$AE(N_2^*) = E(S–N_2^*) - E(S) - E(N_2) \quad (1)$$

where $E(S)$, $E(N_2)$ and $E(S–N_2)$ are the calculated total energies for the catalyst surface, gas-phase N_2 and N_2 adsorbed on the catalyst. The star * indicates the adsorption state. All energies have been corrected with zero-point energy. The free energy change associated with N_2-adsorption, labelled $G(N_2^*)$, has been calculated by

$$G(N_2^*) = G(S–N_2^*) - G(S) - G(N_2) \quad (2)$$

where $G(S)$, $G(N_2)$ and $G(S–N_2^*)$ are the calculated Gibbs free energies for the catalyst surface, gas-phase N_2 and N_2 adsorbed on the catalyst. Transition states have been searched for key elementary steps (e.g., PDS). To treat the pair of protons and electrons, a reference state, hydrogen adsorbed on the surface (H^*), has been employed following the literature.[39–41] It is worth highlighting that all calculations were based on the proton-coupled electron transfer approach with a standard hydrogen electrode (SHE) as the reference,[42] which is a rough approximation as accurate calculation of electrochemical kinetics is still an open challenge.

3. Results and discussion

3.1 NRR on clean $Mo_2C(100)$

Before the calculation of electrochemical reactions, we evaluated the electronic structure of $Mo_2C(100)$ through calculating the density of states (DOS), as shown in Fig. 1(c), and found that the line for Fermi energy (blue line) crosses the DOS profile, indicating the metallic nature and high conductivity, which is good for electrochemical catalysis.

To investigate the effect of H-terminals, we first investigate the NRR on clean $Mo_2C(100)$, with calculated energy profiles and intermediate states shown in Fig. 2, in which the catalyst is shown in the central part. For N_2, end-on adsorption on the top of Mo is favourable, with an adsorption energy AE(N_2^*) = −0.76 eV and $\Delta G(N_2^*)$ = −0.13 eV, indicating that the surface has a strong capacity to fix N_2. The N–N distance is enlarged to 1.13 Å, suggesting the activation of a N≡N bond. Generally, it is believed that the NRR may follow three typical mechanisms, namely distal, alternating and enzymatic paths,[2,3] depending on the N_2 adsorption and NRR energy profile. Starting from
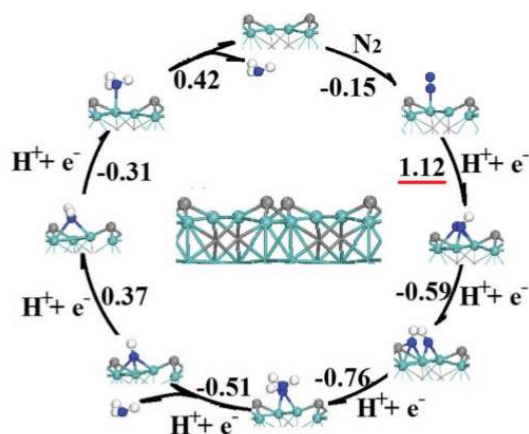
This journal is © the Owner Societies 2018

Phys. Chem. Chem. Phys., 2018, **20**, 23338–23343 | 23339

47

Fig. 2 Energy profile and intermediate states for full NRR on $Mo_2C(100)$ without H-terminals. Mo, C, N and H are shown as cyan, grey, blue and white spheres. Calculated ΔG for each step is shown in the unit of eV.

Fig. 3 Geometries of H-covered $Mo_2C(100)$ with different coverages. (a) $N = 1$; (b) $N = 2$; (c) $N = 3$; (d) $N = 4$; (e) $N = 5$; and (f) $N = 6$. Mo, C and H are shown as cyan, grey and white spheres. The bottom layers are shown as lines.

end-on adsorption, the NRR may follow the distal or alternating path. Our calculations show $\Delta G_{max} = 1.12$ eV and 1.13 eV for the distal and alternating mechanism, respectively. The energy profile and intermediate states for the preferred distal/alternating mixed path are shown in Fig. 2, according to which the PDS has been identified as $N_2^* \rightarrow N_2H^*$, with a kinetic barrier of 1.35 eV. As ΔG_{max} is still large and the PDS comes from the stage of 1st NH_3 formation, N_2 activation needs stronger activation.

3.2 Hydrogen termination

In principle, the HER starts from the formation of the H-adatom *via* the Volmer step, $H^+ + e^- \rightarrow H^*$. According to the model of $Mo_2C(100)$, both Mo and C are exposed and may react with protons. For single hydrogen, the adsorption on Mo is slightly stronger than that on C, with $\Delta G = -0.81$ eV on the bridging site of two Mo atoms and $\Delta G = -0.50$ eV on the top of C, as shown in Fig. 3(a). Starting from the 2nd H*, the C- and Mo-sites are favourable alternately due to the coverage effect, and the optimized geometries with different numbers of H-terminals are shown in Fig. 3(b–f) with $N = 2$–6. Given that the surface contains six surface atoms (Mo_4C_2), $N = 6$ leads to full coverage. In terms of energy, the formation of the 5th and 6th H-terminal is endothermic, with $\Delta G(H^*) = 0.03$ eV and 0.15 eV, respectively. Under the electrochemical conditions for the NRR, additional energy input is often provided with an external voltage, which can be the driving force for the formation of these high-coverage H-terminals. Therefore, it is concluded that $Mo_2C(100)$ is actually H-terminated when it is applied in the NRR.

Another key parameter is the overpotential for the HER. H* may further react with protons or neighbouring H* to release H_2. Using the SHE as a reference,[42] the HER overpotential can be estimated using $\Delta G(H^*)$, as widely reported in the literature.[43,44] In the case of $Mo_2C(100)$, the HER overpotential should be small, around 0.1–0.8 V, depending on the coverage.

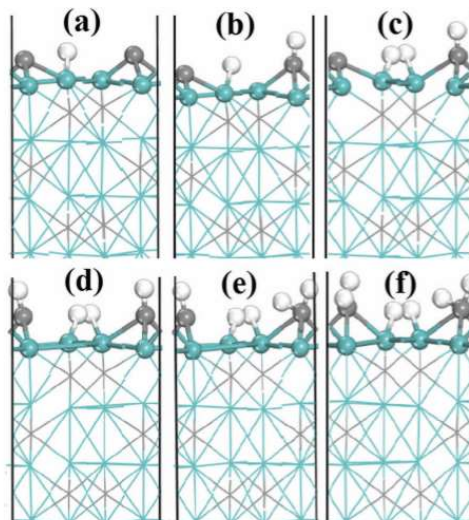The fast HER will compete with the NRR, resulting in low energy efficiency, which is a key issue for Mo-based NRR catalysts. Recently, cubic MoC has been explored as a NRR catalyst, whose $|\Delta G(H^*)|$ is in the range of 0.1–0.6 eV for MoC and $Mo_{0.5}C$, depending on surface orientation.[18] It is worth mentioning that this calculation is for single H*, which is often stronger than the full coverage case. $|\Delta G(H^*)|$ is 0.81 eV for the adsorption of single H* in the case of Mo_2C, which is higher than that of the surfaces of cubic MoC.

3.3 NRR on H-terminated $Mo_2C(100)$

To investigate the NRR on H-terminated $Mo_2C(100)$, the H-covered surface needs to be selected. Based on the calculated $\Delta G(H^*)$, high coverages with $N = 5$ and $N = 6$ are highly possible under the NRR conditions (as an external potential U is applied). Therefore, $Mo_2C(100)$ with $N = 5$ and $N = 6$ has been employed for the study of NRR elementary steps. The key question is whether H-covered Mo_2C can offer the capacity to adsorb and activate N_2. Fig. 4 shows the model, NRR energy profile and intermediate states involved in the elementary steps. From Fig. 4, we can see that three of the five adsorbed H-atoms are bonded with carbon, leaving two Mo-atoms as the potential adsorption sites for N_2. One N_2 molecule has been introduced to the surface, as shown in Fig. 4, and Mo–N_2 bonding has been found with the Mo–N distance of 2.04 Å, which is close to the Mo–N bond length in MoN_2 nanosheets (2.09 Å[11,45,46]). The calculated $AE(N_2^*)$ is -0.50 eV, which is smaller than that on clean $Mo_2C(100)$ ($AE = -0.76$ eV), suggesting that the adsorption becomes weak due to H-termination.

Once N_2 is adsorbed, six pairs of ($H^+ + e^-$) have been added to release two NH_3 molecules, and the reaction reaches the

48

Fig. 4 Energy profile and intermediate states for full NRR on H-covered $Mo_2C(100)$ with N = 5. Mo, C, N and H are shown as cyan, grey, blue and white spheres. Calculated ΔG for each step is shown in the unit of eV.

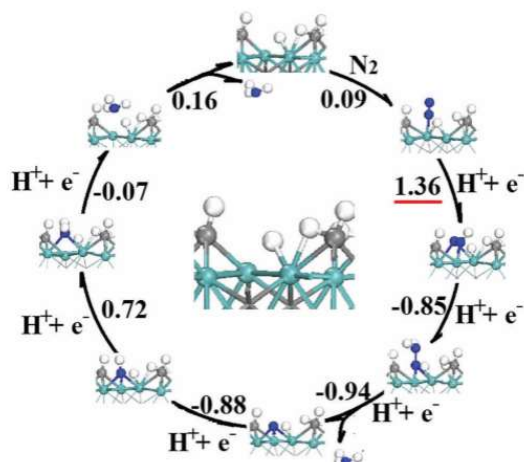**Fig. 5** Energy profile and intermediate states for the full NRR on H-covered $Mo_2C(100)$ with N = 6. Mo, C, N and H are shown as cyan, grey, blue and white spheres. Calculated ΔG for each step is shown in the unit of eV.
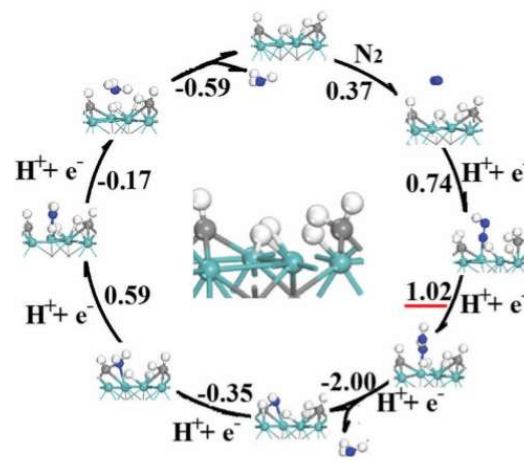
reduction stage. The 2nd change due to the H-terminals is the change of the reaction mechanism as now the distal mechanism is favourable, as shown in Fig. 4. The PDS is still the same and comes from the first hydrogenation step with ΔG = 1.36 eV and a barrier of 1.91 eV. Generally, a PDS from the formation of the first NH_3 often means that N_2 activation is not enough and stronger N_2 adsorption is needed. Among the remaining steps, the maximum ΔG is 0.72 eV for $NH^* \rightarrow NH_2^*$. From the NH^* geometry (see Fig. 4), N^* is three-coordinated by Mo. H-adding to form NH^* results in full coordination for N, and additional H-adding will turn Mo_3–N^* into Mo_2–NH^*, demanding energy to make this happen. Final NH_3 release gives ΔG = 0.16 eV, indicating that the Mo–NH_3 bond strength is weak and ideal for the NRR. Overall, a minimum overpotential of 1.36 V is needed for full $N_2 \rightarrow NH_3$ conversion, which is larger than that of several transition metals and newly reported 2D NRR catalysts.[6–13]

Now, we turn to the case of N = 6 to understand the coverage effect on NRR catalysis. Fig. 5 shows the calculated results. Compared with N = 5, another –CH_2 has been generated. It seems that H-termination on the Mo-sites causes little change. However, the energy profile has been notably changed with respect to that for N = 5, including: (i) $\Delta G(N_2^*)$ increases from 0.09 eV to 0.37 eV, suggesting that N_2 adsorption becomes very weak; (ii) ΔG_{max} decreases from 1.36 eV to 0.74 eV for the addition of the 2nd hydrogen ($N_2H^* \rightarrow NNH_2^*$); and (iii) final NH_3 release becomes exothermic. From the optimized geometry, it is clear that N_2 can only physically adsorb on the fully H-terminated surface, due to which the energy change from N_2 to N_2H becomes smaller. To achieve excellent kinetics under electrochemical conditions, efficient electron transfer is essential; therefore, fast kinetics can be hardly obtained from such physical N_2-adsorption. This can be directly reflected by the large barrier of 2.17 eV because inserting N_2 to form a N–Mo bond requires the breaking of two H–Mo bonds under the full H-termination.

This can also be reflected by the fact that both the most and second most energy-demanding steps come from the generation of the first NH_3. Overall, full H-termination results in performance deterioration for Mo_2C.

Another interesting result is that surface hydrogen is actively involved in the surface reaction, including (i) the stabilization of NHx, which is related to the hydrogen bonding between the H* and NHx* species; and (ii) the internal H-transfer between different bonding sites (Mo- and C-site, see Fig. 3), which may result in the formation of CH_4 gas, generating carbon-vacancies. Therefore, better understanding of the behaviour of surface hydrogen is critical for the analysis of the catalysis of this material.

3.4 Effect of Fe-doping

For Mo metal, the Mo–N_2 interaction is too strong; therefore, a relatively weak N_2-adsorber can be considered as an alloy element to improve NRR performance.[31] Given that Fe and Mo are the two metals contained in nitrogenase cofactors,[23,47,48] the FeMo combination has been employed in the design of NRR catalysts.[11] In our early study on MoN_2 nanosheets,[11] Fe-doping was reported as an effective approach to improve the performance of the MoN_2 nanosheets. Therefore, Fe-doping has also been considered here for Mo_2C. Using H-terminated Mo_2C with N = 6 as an example, the NRR energy profile has been calculated and is listed in Fig. 6. Compared with the undoped case, three features can be summarized: (i) N_2 adsorption is even worse, with $\Delta G(N_2^*)$ slightly increasing from 0.38 eV to 0.40 eV; (ii) the PDS shifts from the formation of the 1st NH_3 to the second, with ΔG_{max} = 1.36 eV ($NH^* \rightarrow NH_2^*$, highlighted in Fig. 6 by a red line); and (iii) the final NH_3 release remains exothermic. Clearly, the key issue of N_2 adsorption has not been improved by Fe-doping, and the overall NRR performance has shown almost no improvement.
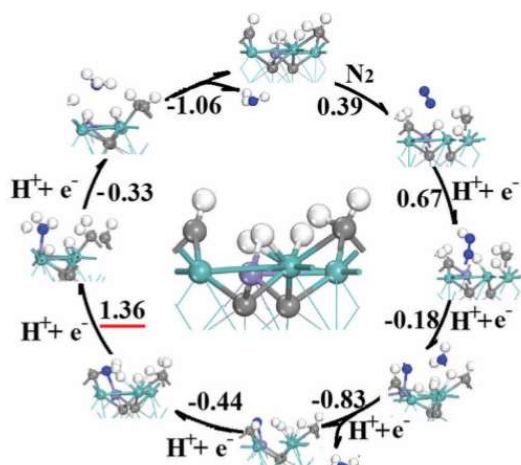
49

Fig. 6 Energy profile and intermediate states for full NRR on H-covered Fe-doped $Mo_2C(100)$ with $N = 6$. Fe, Mo, C, N and H are shown as purple, cyan, grey, blue and white spheres. Calculated ΔG for each step is shown in the unit of eV.

For MoN_2, N_2 is adsorbed by a N-vacancy;[11] as a result, strong Mo–N bonding is generated and the PDS for the full NRR comes from the formation of the 2nd NH_3 ($NH^* \rightarrow NH_2^*$). For the single-Mo catalyst, the PDS may come from $N_2^* \rightarrow N_2H^*$, but ΔG is often small as N_2 can be effectively activated.[49] In such Mo–N systems, a weaker N_2-adsorber, like Fe, is helpful, as demonstrated before.[11] However, for both $N = 5$ and $N = 6$ in the case of H-terminated Mo_2C, the PDS comes from formation of the first NH_3, suggesting that a stronger N_2-adsorber is needed, which is why Fe-doping does not help in this case. The given Mo is already a strong N_2-adsorber,[11] and the weak Mo–N_2 interaction is essentially due to the H-terminals; therefore, the suppression of H-termination becomes critical, not only for reducing the HER, but also to maximize use of the active sites.

4. Conclusions

In summary, α-$Mo_2C(100)$ has been explored as a NRR catalyst by DFT calculations. It is found that the surface can be easily H-terminated, being consistent with cubic MoC. Such H-termination can remarkably affect NRR performance, including: (i) N_2 adsorption becomes weak; (ii) N_2 reduction to generate the first NH_3 is endothermic, requesting an energy input of $\sim$1.4 eV for heavily H-covered surfaces; and (iii) Fe-doping cannot provide a similar improvement to that reported in the case of MoN_2. In terms of the performance, H-covered Mo_2C is not an ideal NRR catalyst considering its low HER overpotential, large ΔG_{max} ($\sim$1.4 eV) and kinetic barrier ($\sim$2.0 eV). It is worth highlighting that the relatively poor performance is essentially due to H-termination. Based on this knowledge, we strongly suggest that the H-termination effect needs to be seriously evaluated for NRR catalysts, considering not only that HER is a side reaction and

directly affects Faraday efficiency, but also that it changes the nature of the catalyst surfaces.

Conflicts of interest

There are no conflicts to declare.

Acknowledgements

Notes and references

1 B. K. Burgess and D. J. Lowe, *Chem. Rev.*, 1996, **96**, 2983–3012.

2 B. M. Hoffman, D. Lukoyanov, D. R. Dean and L. C. Seefeldt, *Acc. Chem. Res.*, 2013, **46**, 587–595.

3 B. M. Hoffman, D. Lukoyanov, Z.-Y. Yang, D. R. Dean and L. C. Seefeldt, *Chem. Rev.*, 2014, **114**, 4041–4062.

4 S. Qiu, L. M. Azofra, D. R. MacFarlane and C. Sun, *ACS Catal.*, 2016, **6**, 5541–5548.

5 S. Qiu, L. M. Azofra, D. R. MacFarlane and C. Sun, *Phys. Chem. Chem. Phys.*, 2016, **18**, 15369–15374.

6 E. Skúlason, T. Bligaard, S. Gudmundsdóttir, F. Studt, J. Rossmeisl, F. Abild-Pedersen, T. Vegge, H. Jónsson and J. K. Nørskov, *Phys. Chem. Chem. Phys.*, 2012, **14**, 1235–1245.

7 J. G. Howalt, T. Bligaard, J. Rossmeisl and T. Vegge, *Phys. Chem. Chem. Phys.*, 2013, **15**, 7785–7795.

8 D. V. Yandulov and R. R. Schrock, *Science*, 2003, **301**, 76–78.

9 R. R. Schrock, *Acc. Chem. Res.*, 2005, **38**, 955–962.

10 B. M. Flöser and F. Tuczek, *Coord. Chem. Rev.*, 2017, **345**, 263–280.

11 Y. Abghoui, A. L. Garden, V. F. Hlynsson, S. Björgvinsdóttir, H. Ólafsdóttir and E. Skúlason, *Phys. Chem. Chem. Phys.*, 2015, **17**, 4909–4918.

12 L. M. Azofra, N. Li, D. R. MacFarlane and C. Sun, *Energy Environ. Sci.*, 2016, **9**, 2545–2549.

13 Q. Li, L. He, C. Sun and X. Zhang, *J. Phys. Chem. C*, 2017, **121**, 27563–27568.

14 J. Rittle and J. C. Peters, *J. Am. Chem. Soc.*, 2016, **138**, 4243–4248.

15 J. Zhao and Z. Chen, *J. Am. Chem. Soc.*, 2017, **139**, 12480–12487.

16 L. M. Azofra, C. Sun, L. Cavallo and D. R. MacFarlane, *Chem. – Eur. J.*, 2017, **23**, 8275–8279.

17 M. Shao, Y. Shao, W. Chen, K. L. Ao, R. Tong, Q. Zhu, I. N. Chan, W. F. Ip, X. Shi and H. Pan, *Phys. Chem. Chem. Phys.*, 2018, **20**, 14504–14512.

18 I. Matanovic and F. H. Garzon, *Phys. Chem. Chem. Phys.*, 2018, **20**, 14679–14687.

50

19 W. Zheng, T. P. Cotter, P. Kaghazchi, T. Jacob, B. Frank, K. Schlichte, W. Zhang, D. S. Su, F. Schüth and R. Schlögl, *J. Am. Chem. Soc.*, 2013, **135**, 3458–3464.

20 C. Xu, L. Wang, Z. Liu, L. Chen, J. Guo, N. Kang, X.-L. Ma, H.-M. Cheng and W. Ren, *Nat. Mater.*, 2015, **14**, 1135.

21 Z. Liu, C. Xu, N. Kang, L. Wang, Y. Jiang, J. Du, Y. Liu, X.-L. Ma, H.-M. Cheng and W. Ren, *Nano Lett.*, 2016, **16**, 4243–4250.

22 C. Xu, S. Song, Z. Liu, L. Chen, L. Wang, D. Fan, N. Kang, X. Ma, H.-M. Cheng and W. Ren, *ACS Nano*, 2017, **11**, 5906–5914.

23 K. M. Lancaster, M. Roemelt, P. Ettenhuber, Y. Hu, M. W. Ribbe, F. Neese, U. Bergmann and S. DeBeer, *Science*, 2011, **334**, 974–977.

24 J. H. Montoya, C. Tsai, A. Vojvodic and J. K. Nørskov, *ChemSusChem*, 2015, **8**, 2180–2186.

25 C. Guo, J. Ran, A. Vasileff and S.-Z. Qiao, *Energy Environ. Sci.*, 2018, **11**, 45–56.

26 C. Xiaoyang, T. Cheng and Z. Qiang, *Adv. Energy Mater.*, 2018, 1800369.

27 J. S. Kang, J. Kim, M. J. Lee, Y. J. Son, D. Y. Chung, S. Park, J. Jeong, J. M. Yoo, H. Shin, H. Choe, H. S. Park and Y.-E. Sung, *Adv. Sci.*, 2018, **5**, 1700601.

28 X. Junfeng, Z. Hao, L. Shuang, W. Ruoxing, S. Xu, Z. Min, Z. Jingfang, L. X. Wen and X. Yi, *Adv. Mater.*, 2013, **25**, 5807–5813.

29 G. Li, D. Zhang, Q. Qiao, Y. Yu, D. Peterson, A. Zafar, R. Kumar, S. Curtarolo, F. Hunte, S. Shannon, Y. Zhu, W. Yang and L. Cao, *J. Am. Chem. Soc.*, 2016, **138**, 16632–16638.

30 F. Zhou, L. M. Azofra, M. Ali, M. Kar, A. N. Simonov, C. McDonnell-Worth, C. Sun, X. Zhang and D. R. MacFarlane, *Energy Environ. Sci.*, 2017, **10**, 2516–2520.

31 C. J. H. Jacobsen, S. Dahl, B. S. Clausen, S. Bahn, A. Logadottir and J. K. Nørskov, *J. Am. Chem. Soc.*, 2001, **123**, 8404–8405.

32 J. Zhao, J. Zhao and Q. Cai, *Phys. Chem. Chem. Phys.*, 2018, **20**, 9248–9255.

33 J. G. Howalt and T. Vegge, *Phys. Chem. Chem. Phys.*, 2013, **15**, 20957–20965.

34 W. Kohn and L. J. Sham, *Phys. Rev.*, 1965, **140**, A1133–A1138.

35 B. Hammer, L. B. Hansen and J. K. Nørskov, *Phys. Rev. B: Condens. Matter Mater. Phys.*, 1999, **59**, 7413–7421.

36 G. Kresse and D. Joubert, *Phys. Rev. B: Condens. Matter Mater. Phys.*, 1999, **59**, 1758–1775.

37 G. Kresse and J. Hafner, *Phys. Rev. B: Condens. Matter Mater. Phys.*, 1993, **47**, 558–561.

38 L. Goerigk and S. Grimme, *J. Chem. Theory Comput.*, 2010, **6**, 107–126.

39 X. Nie, M. R. Esopi, M. J. Janik and A. Asthagiri, *Angew. Chem., Int. Ed.*, 2013, **52**, 2459.

40 X. Nie, W. Luo, M. J. Janik and A. Asthagiri, *J. Catal.*, 2014, **312**, 108–122.

41 L. M. Azofra, C. Sun, L. Cavallo and D. R. MacFarlane, *Chem. – Eur. J.*, 2017, **23**, 8275–8279.

42 Q. Tang and D.-E. Jiang, *ACS Catal.*, 2016, **6**, 4953–4961.

43 G. Gao, A. P. O'Mullane and A. Du, *ACS Catal.*, 2017, **7**, 494–500.

44 W. Ya-Pan, Z. Wei, Z. Jun, D. Wen-Wen, L. Ya-Qian, L. Dong-Sheng, S. Chenghua and B. Xianhui, *Angew. Chem., Int. Ed.*, 2017, **56**, 13001–13005.

45 S. Wang, H. Ge, S. Sun, J. Zhang, F. Liu, X. Wen, X. Yu, L. Wang, Y. Zhang, H. Xu, J. C. Neuefeind, Z. Qin, C. Chen, C. Jin, Y. Li, D. He and Y. Zhao, *J. Am. Chem. Soc.*, 2015, **137**, 4815–4822.

46 Y. Wang, S.-S. Wang, Y. Lu, J. Jiang and S. A. Yang, *Nano Lett.*, 2016, **16**, 4576–4582.

47 J. Schimpl, H. M. Petrilli and P. E. Blöchl, *J. Am. Chem. Soc.*, 2003, **125**, 15772–15778.

48 T. Lovell, J. Li, T. Liu, D. A. Case and L. Noodleman, *J. Am. Chem. Soc.*, 2001, **123**, 12392–12410.

49 C. Ling, X. Bai, Y. Ouyang, A. Du and J. Wang, *J. Phys. Chem. C*, 2018, **122**, 16842–16847.

This journal is © the Owner Societies 2018

Phys. Chem. Chem. Phys., 2018, **20**, 23338–23343 | **23343**

51

Chapter 6 Single-atom Catalyst for NRR

6.1 Overview

Starting from molybdenum (Mo) embedded in black phosphorus (BP), 17 single Mo catalysts with various combinations of ligands, including phosphorous (P), boron (B), nitrogen (N), sulphur (S) and carbon (C), have been computationally examined as catalysts for nitrogen reduction reaction. Among them, Mo-PC$_2$, Mo-PB$_2$ and Mo-BC$_2$ have been identified as the most promising catalysts, offering an overall overpotential less than 0.60 V. Mo-BC$_2$ is particularly attractive as it also shows a high NRR selectivity over hydrogen evolution reaction. Such high performance essentially is originated from the mediation of the ligands, which effectively shift the d-band center of Mo-atom towards the Fermi energy.

Computational Design of Single-Molybdenum Catalysts for the Nitrogen Reduction Reaction

Qinye Li,[†] Siyao Qiu,[§] Chuangwei Liu,[‡] Mingguo Liu,[∥] Lizhong He,[†] Xiwang Zhang,*,[†] and Chenghua Sun*,[§,⊥]

[†]School of Chemical Engineering and [‡]School of Chemistry, Monash University, Clayton, VIC 3800, Australia

[§]Science & Technology Innovation Institute, Faculty of Science, Dongguan University of Technology, Dongguan 523808, China

[∥]Hubei Key Laboratory of Natural products Research and Development, College of Biological and Pharmaceutical Sciences, China Three Gorges University, Yichang 443002, China

[⊥]Department of Chemistry and Biotechnology, Faculty of Science, Engineering & Technology, Swinburne University of Technology, Hawthorn, VIC 3122, Australia

Ⓢ *Supporting Information*

ABSTRACT: Starting from molybdenum (Mo) embedded in black phosphorus, 17 single-Mo catalysts with various combinations of ligands, including phosphorous (P), boron (B), nitrogen (N), sulfur (S), and carbon (C), have been computationally examined as catalysts for the nitrogen reduction reaction. Among them, Mo−PC$_2$, Mo−PB$_2$, and Mo−BC$_2$ have been identified as the most promising catalysts, offering an overall overpotential less than 0.60 V. Mo−BC$_2$ is particularly attractive as it also shows a high nitrogen reduction reaction selectivity over the hydrogen evolution reaction. Such high performance is originated essentially from the mediation of the ligands, which effectively shift the d-band center of the Mo atom toward the Fermi energy.
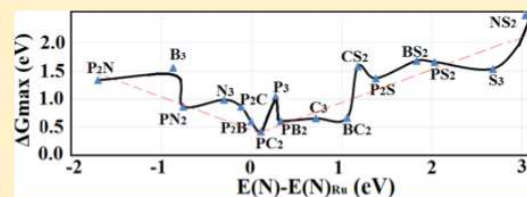
■ INTRODUCTION

Molybdenum (Mo) offers a strong capacity to adsorb nitrogen (N$_2$), but the Mo−N$_2$ interaction is too strong for the full nitrogen reduction reaction (NRR),[1,2] a key step for ammonia (NH$_3$) synthesis.[3−5] Therefore, additional mediation is needed. Schrock and co-workers demonstrated N$_2$ reduction to ammonia using a Mo−N complex bearing tetradentate triamidoamine ligands,[6] achieving 8 equiv of ammonia because of the Mo atom of the catalyst. Later, a Mo complex bearing 2,6-bis(di-*tert*-butylphosphinomethyl)pyridine (PNP) ligands has been developed, in which phosphorous (P) have been introduced to optimize the performance, achieving 23 equiv of ammonia with the catalyst, of which one molybdenum atom produces 12 equiv of ammonia.[7] When more P ligands have been introduced, like a mer-triphosphine, up to 63 equiv of ammonia can be produced because of the molybdenum atom.[8] Last year, Mo mediated by PNP-type pincer ligands even set a new record of 415 equiv of NH$_3$ per Mo.[9,10] These achievements vividly demonstrated the importance of ligand optimization in the design of NRR catalysts.

Following these successes in the design of a molecular complex, the search for Mo-based NRR catalysts has been extended to inorganic materials and single-Mo catalysts in recent years.[11−17] Azofra et al. examined M$_3$C$_2$ MXene (M = d^2−d^4 transition metals), including Mo$_3$C$_2$ (Mo is three-coordinated as Mo−C$_3$), which shows a strong capacity to adsorb N$_2$.[11] Mo−N bonding has also been considered for

NRR catalysis.[12−14] As reported by Li et al., a MoN$_2$ nanoshseet may generate N vacancy under electrochemical conditions, which actively fills N$_2$ via Mo−N$_3$ bonding and offers excellent NRR performance, especially after Fe doping.[14] In addition, single-Mo catalysts have been incorporated into the boron nitride nanosheet[15] and N-doped graphene,[16] for which Mo−N bonding has been identified as an effective way to optimize the performance of the Mo center. In contrast, P and boron (B) ligands are rarely studied in the design of inorganic NRR catalysts, although the Mo−P$_3$ complex has shown great success.[7,8] To further optimize its performance, a systematic search for optimum ligands is still needed. Herein, we envisaged the design of novel single-Mo catalysts on the basis of Mo−P bonding through density functional theory (DFT) calculations. Inspired by the findings of Nishibayashi and co-workers,[6−8] Mo−P$_3$ bonding has been employed as a basic point through introducing a single Mo atom on black phosphors (BPs) to provide an ideal Mo−P$_3$ bonding environment, followed by an additional evaluation of various ligand combinations. As demonstrated below, Mo−BC$_2$ has been successfully identified as a new promising model catalyst for NRR.
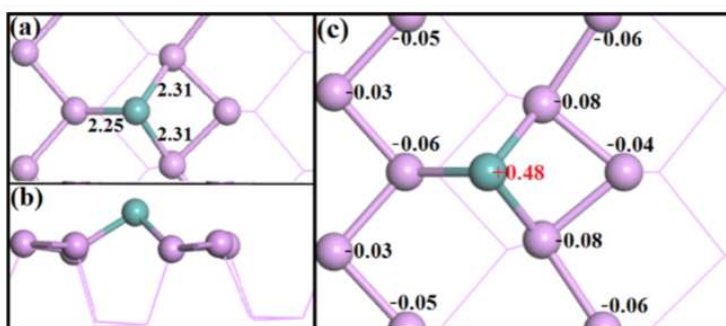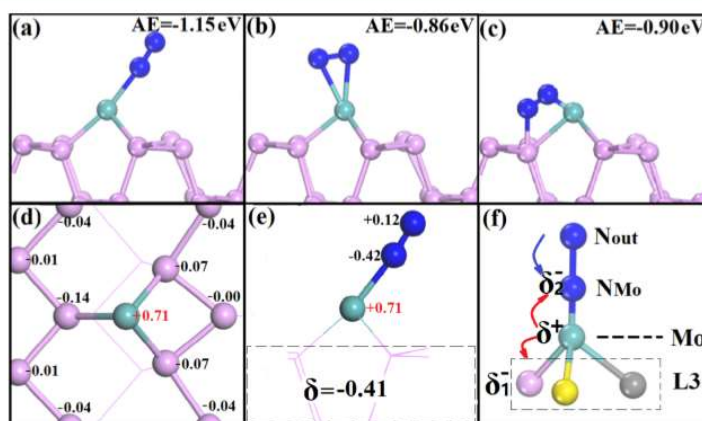
Figure 1. Mo−P$_3$ catalyst. (a) Top view and (b) side view of a single Mo atom adsorbed on BP. (c) Bader charge distribution. Mo and P are shown as cyan and purple spheres. The charges shown in (c) are in the unit of e.

Figure 2. N$_2$ adsorption on the Mo−P$_3$ catalyst. (a) End-on adsorption, (b) side-on adsorption, (c) tilt end-on adsorption, (d) Bader charge distribution after N$_2$ adsorption for Mo (cyan) and P (purple, only showing the first layer), (e) Bader charges for Mo and adsorbed N$_2$ (blue), and (f) schematic configuration for the charge transfer involved with Mo−L$_3$ catalysts after N$_2$ adsorption. The charges are in the unit of e.

METHODS

The computational searching and calculations were carried out through spin-polarized density functional theory (DFT) with the generalized gradient approximation using the revised Perdew−Burke−Ernzerhof functional.[18,19] BP has been simulated with a 2 × 2 supercell, with a single Mo atom bonded by three P ligands (Mo$_1$−P$_{16}$, dimension: 8.98 Å × 6.62 Å), labeled as Mo−P$_3$. The optimization of ligands is further carried out by replacing bonded P atoms with new ligands, including C, N, S, and B. NRR was studied through the calculation of free energy changes (ΔG) associated with all elementary steps, including N$_2$ adsorption, reduction by six pairs of H$^+$ and e$^-$, and NH$_3$ release, as described in the literature.[20−22] The maximum ΔG, labeled as ΔG_{max}, was employed to identity the rate-determining steps (RDS) and was also employed as an indicator to evaluate the NRR performance. Small ΔG_{max} means low energy request for full NRR. ΔG_{max} of 1.08 eV for flat ruthenium (Ru) (0001) was used as a reference for the discussion.[23]

RESULTS

Figure 1a,b shows the top and side views of optimized geometries of a single Mo atom on BP, respectively, showing

that Mo is three-coordinated and the planar shape of BP has been kept well. Specifically, the averaged distance between Mo and the nearest phosphorus is 2.27 Å, slightly shorter than that of a single Mo−P bond in typical Mo-based complexes (2.4− 2.6 Å),[24] indicating the effective Mo−P bonding. To further determine the oxidation state of Mo, Bader charge has been particularly calculated, as presented in Figure 1c. Mo shows an oxidation state of +0.48e, indicating net electrons transferred from Mo to BP, which are mainly distributed in the first P layer.

N$_2$ adsorption on a single Mo atom adsorbed on BP with three potential geometries was analyzed, including end-on, side-on, and tilt end-on adsorption geometries.[25] The optimized geometries are shown in Figure 2a−c, together with the calculated adsorption energies (AEs, in eV), according to which end-on adsorption is more favorable by >0.2 eV than the other two, demonstrated by a calculated adsorption energy, AE(N$_2$*), of −1.15 eV. N−N distance increases from 1.10 Å (free N$_2$) to 1.13 Å, indicating that the N≡N bond is partially activated. Figure 2d shows the detailed distribution of Bader charges after N$_2$ adsorption. Clearly, the net charge on Mo has been slightly changed, from +0.48e to +0.71e, donating 0.41e to BP and 0.30e to N$_2$. This result suggests a competition between N$_2$ and the substrate for electrons. Interestingly, two

N atoms show quite different charge states, $-0.42e$ (bonded with Mo, N_{Mo}) and $+0.12e$ (the outside one), as shown in Figure 2e. Another interesting change is that the charge for one of three P ligands varies from $-0.06e$ to $-0.14e$, suggesting that the ligands can strongly affect the charge state of the Mo center and consequently the charge transfer from Mo to N_2, which is critical for N_2 activation and reduction. Figure 2f summarizes the basic information on charge transfer involved in N_2 adsorption on such Mo$-L_3$ catalysts. Specifically, the charge on N_{out} (the first hydrogenation site for NRR) is determined by $N_{out} \rightarrow N_{Mo}$ and Mo $\rightarrow N_{Mo}$ electron transfer, highlighting the importance of ligands in the tuning of charge state of the Mo center.

For full NRR, three mechanisms have been investigated for Mo$-P_3$, including distal, alternating, and enzymatic paths and their hybrid forms.[26] In the case of Mo$-P_3$, the distal path is preferred on the basis of our tests (see the Supporting Information, Figure S1). The geometry of the Mo$-P_3$ catalyst and the calculated ΔG for each elementary step are shown in Figure 3a,b, respectively. Accordingly, ΔG_{max} of 1.04 eV has
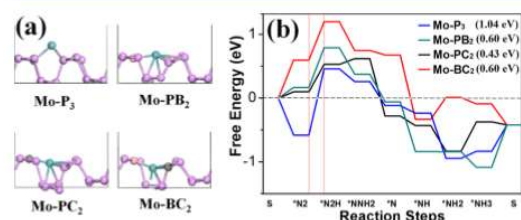
Figure 3. Promising NRR catalysts. (a) Optimized geometries and (b) calculated NRR profile. Mo, P, N, and H are shown as cyan, purple, blue, and white spheres, respectively. The free energy change for $N_2 \rightarrow N_2H$ is the maximum one for overall NRR and has been shown in parentheses in the unit of eV.

been derived for the rate-determining step (RDS), $N_2^* + H^+ + e^- \rightarrow N_2H^*$, with all intermediate states shown in Figure S2(a). To understand the $N_2$$-$Mo interaction, we start from the molecular orbitals of free nitrogen whose bonding states of σ_{2p} and π_{2p} are fully occupied; therefore, electron injection to antibonding states or electron donation to catalysts can reduce the N$-$N bond order, activating the N≡N bond. According to Figure 2e, electron injection of 0.30e from Mo to N_2 occurs, which is the basis for the strong Mo$-$N interaction, leading to

large AE. However, such charge transfer is highly localized to N_{Mo}. N_{out}, as the preferred site for the first H addition, is positively charged ($+0.12e$); as a result, its σ_{2p} is partially empty. Following this analysis, the NRR performance of the Mo center may be improved through tuning its capacity of electron donation to N_2. As P_3 ligands are competing with N_2 for electron transfer, it is likely to regulate the reactivity of the Mo center through introducing new nonmetals to replace P ligands.

Following the above analysis, a series of model catalysts starting from the Mo$-P_3$ configuration were screened with p-block ligands, including B, C, N, S, and P. The optimized geometries for these 17 catalysts are shown in Figures S3 and S4. In most cases, Mo can be stably fixed by the ligands, except S ligands that result in severe distortion, indicating the low stability of these structures as listed separately in Figure S4. Therefore, S ligands are not recommended for the mediation of single-Mo catalyst, as confirmed later by a calculation of full NRR.

For NRR, the adsorption energy of a single nitrogen, labeled as $E(N^*)$, has been widely employed as an indicator to search for potential catalysts and a volcano curve has often been obtained when the experimental values of the turnover frequency are plotted against $E(N^*)$.[27] Promising NRR catalysts offer a value of $E(N^*)$ close to that of the Ru benchmark catalyst. Among the 17 concept catalysts, Mo$-P_2B$ and Mo$-PC_2$ show $E(N^*)$ of -0.47 and -0.36 eV, respectively, close to that of stepped Ru(0001),[28] suggesting that these two are promising NRR catalysts. To further examine this result, a calculation of full NRR over these catalysts has been carried out, with calculated ΔG_{max} plotted versus $E(N^*)$ in Figure 4a, in which the catalysts are indicated by the ligands for clarity. A reversed volcano curve between ΔG_{max} and $E(N^*) - E(N^*)_{Ru}$ has been plotted, confirming the validity of the $E(N^*)$ indicator. It is worth noting that such validity origins from the linear relationship between the adsorption energies of intermediates; therefore, scattering or deviation from the linear is often seen, particularly when the RDS comes from N_2 adsorption, NH_3 release, or surface reconstruction during the reaction (e.g., for S-mediated single-Mo catalysts in this work, severe distortion has been found, see Figure S4).

In Figure 3a, several concept catalysts have been identified as 'good candidates' using the $E(N^*)$ indicator, which have been confirmed as excellent catalysts by the calculated ΔG_{max} (e.g.,
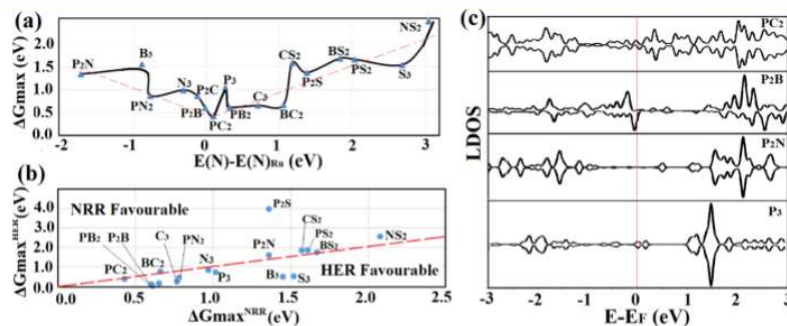
Figure 4. Computational screening of ligands combinations. (a) ΔG_{max} vs $E(N) - E(N)_{Ru}$, (b) $\Delta G_{max(HER)}$ vs $\Delta G_{max(NRR)}$, and (c) calculated local density of states (LDOS) for the Mo center for catalysts Mo$-P_3$, $-P_2B$, $-PC_2$, and $-P_2N$, using Fermi energy E_F as the reference.

0.43 eV for Mo−PC$_2$ and ∼0.60 eV for Mo−BC$_2$ and Mo−PB$_2$). Moreover, the RDS is similar to the Mo−P$_3$ case, which comes from the *N$_2$ → *N$_2$H step (see the dashed rectangle in Figure 3b), but the overall energy request becomes smaller as shown by the full energy profile. Such performance is close or even lower than half of that for flat Ru(0001) (0.54 eV),[23] a benchmark NRR catalyst. Note that N and S ligands do not bring notable improvement with respect to the Mo−P$_3$ system, consistent with the observation for molecular catalysts.[6,7] Using calculated ΔG_{max} as an indicator of the performance, a reversed volcano curve has been indicated by the dashed red line in Figure 4a, in which $E(N)_{Ru}$ is the adsorption energy of the N atom on stepped Ru(0001).[28] It is also worth noting that (i) such volcano curve points out that an optimum value for $E(N*)$ is close (but not exactly) to that for $E(N)_{Ru}$, consistent with an early study,[2] and (ii) for both P$_2$B and PC$_2$, $E(N*)$ is very close to that of the Ru benchmark catalyst, highlighting the value of these conceptual catalysts and importance of B and C ligands in the tuning of the Mo center.

For NRR, hydrogen evolution reaction (HER) is the key side reaction, leading to low Faraday efficiency (FE) when HER is more favorable than NRR, which has become a major challenge for most NRR catalysts.[29−31] Therefore, additional calculations have been performed for these catalysts and presented with ΔG_{max} for HER versus that for NRR in Figure 4b, with the red dashed line showing ΔG_{max} for NRR being equal to that for HER, in which case the points above the line indicate that NRR is favorable. In the case of Mo−P$_2$S, sulfur diffuses into the BP lattice, resulting in heavy local strain energy associated with a notable deviation from the starting geometry. With H adsorption, such strain has been partially released and the calculated $\Delta G(H*)$ is as low as −3.99 eV; as a result, releasing H$_2$ becomes extremely difficult (>4.0 eV). For other catalysts without S ligands, the calculated ΔG_{max} for HER is in the range of 0.13−1.60 eV, but only those catalysts with ΔG_{max}(NRR) < 1.0 eV are attractive for further consideration in terms of energy efficiency. As shown in Figure 4b, Mo mediated by BC$_2$, PC$_2$, and N$_3$ offers ΔG_{max}(NRR) close to ΔG_{max}(HER), which deserves experimental efforts as they may offer relatively good FE. Especially, Mo−BC$_2$, whose NRR energy profile is shown in Figures 3b and S2c, is the only candidate having NRR preference (ΔG_{max} of 0.60 eV for NRR vs 0.76 eV for HER) among the nine with ΔG_{max}(NRR) < 1.0 eV. With a full consideration of balance and trade-off between NRR and HER for these concept catalysts, Mo−B$_2$C has been recommended as the most promising candidate.

To understand the role of ligands, the charge state of the Mo center before N$_2$ adsorption, δMo, has been first analyzed. Given the valence electron from Mo is shared by the substrate and adsorbed N$_2$, large δMo means that the electron donated by the Mo center is mainly taken up by the ligands; as a result, only a few electrons can be injected to adsorbed N$_2$. However, if δMo is too small, Mo−substrate bonding is very weak and the Mo−N$_2$ interaction may be too strong for NH$_3$ release. Using the combinations of P, N, and B ligands as the example, ΔG_{max} versus δMo has been plotted in the Supporting Information (see Figure S5), showing a poor relevance between δMo and ΔG_{max} (NRR). Therefore, δMo is not a good indicator for the mediation and the searching of ligand combinations. We turn to the local density of states (LDOS) for the Mo atom bonded with different ligands, as presented in Figure 4c for Mo−P$_3$, −P$_2$N, −P$_2$B, and −BC$_2$. Clearly, the N ligand can remarkably stabilize the Mo electrons as major

occupied LDOS are below −1.0 eV, whereas for Mo−P$_2$B and Mo−BC$_2$, quite a lot of states move to the top of valence bands, suggesting that B and C ligands can effectively shift the d-band center, which is helpful to achieve high performance during catalysis. Such a d-band shifting strategy has been widely applied to the design of electrochemical catalysts in the literature, such as for generating defects for FeNiOOH catalysts for oxygen evolution[32] or introducing alloy elements in the metal−organic framework for hydrogen evolution.[33] Very recently, Mo−C$_2$N has been identified as a high-performance NRR catalyst, using a C$_2$N monolayer as the line substrate.[34] Experimentally, the proposed B and C ligands can be introduced with the doping approach, as demonstrated in the literature.[35−37]

CONCLUSIONS

In summary, a systematic search for optimum single-Mo catalysts for NRR has been carried out via the computational DFT approach. Learning from molecular catalysts, Mo−P$_3$ using BP as the substrate has been employed as the model system and 17 concept catalysts with different ligands have been systematically studied. Accordingly, Mo−BC$_2$ has been identified as the most promising catalyst offering ΔG_{max} of 0.60 eV, together with excellent NRR selectivity. Experimental efforts have been made to successfully prepare BP,[35] phosphorous carbides,[36] and boron-doped graphene,[37] and the predicted catalysts (Mo−PB$_2$, Mo−PC$_2$, and Mo−BC$_2$) are highly likely to be synthesized in the lab in the near future. As revealed by calculated LDOS, B, and C ligands can effectively shift the d-band center to the Fermi energy and thus improve the reactivity of the Mo center for N$_2$ adsorption and reduction. Such knowledge can serve as a guideline to tune the electronics of transition metals for NRR and other reactions.

ASSOCIATED CONTENT

ⓢ Supporting Information

The Supporting Information is available free of charge on the ACS Publications website at DOI: 10.1021/acs.jpcc.8b11509.

> Computational details; calculated energy profile for NRR; calculated NRR profile for Mo−P$_3$, Mo−PC$_2$, and Mo−BC$_2$; optimized geometries with Mo; and calculated ΔG_{max} for NRR vs δMo (PDF)

AUTHOR INFORMATION

Corresponding Authors
*E-mail: xiwang.zhang@monash.edu (X.Z.).
*E-mail: chenghuasun@swin.edu.au (C.S.).

ORCID
Lizhong He: 0000-0001-6569-526X
Xiwang Zhang: 0000-0002-4319-527X
Chenghua Sun: 0000-0001-7654-669X

Notes
The authors declare no competing financial interest.

REFERENCES

(1) Jennings, J. R. *Catalytic Ammonia Synthesis: Fundamentals and Practice*; Springer Science & Business Media, 2013.

(2) Jacobsen, C. J. H.; Dahl, S.; Clausen, B. S.; Bahn, S.; Logadottir, A.; Nørskov, J. K. Catalyst Design by Interpolation in the Periodic Table: Bimetallic Ammonia Synthesis Catalysts. *J. Am. Chem. Soc.* 2001, 123, 8404−8405.

(3) Chen, J. G.; Crooks, R. M.; Seefeldt, L. C.; Bren, K. L.; Bullock, R. M.; Darensbourg, M. Y.; Holland, P. L.; Hoffman, B.; Janik, M. J.; Jones, A. K.; et al. Beyond Fossil Fuel-Driven Nitrogen Transformations. *Science* 2018, 360, No. eaar6611.

(4) Guo, C.; Ran, J.; Vasileff, A.; Qiao, S. Z. Rational Design of Electrocatalysts and Photo(electro)catalysts for Nitrogen Reduction to Ammonia (NH$_3$) under Ambient Conditions. *Energy Environ. Sci.* 2018, 11, 45−56.

(5) Cui, X.; Tang, C.; Zhang, Q. A Review of Electrocatalytic Reduction of Dinitrogen to Ammonia under Ambient Conditions. *Adv. Energy Mater.* 2018, 8, No. 1800369.

(6) Yandulov, D. V.; Schrock, R. R. Catalytic Reduction of Dinitrogen to Ammonia at a Single Molybdenum Center. *Science* 2003, 301, 76−78.

(7) Arashiba, K.; Miyake, Y.; Nishibayashi, Y. A Molybdenum Complex Bearing PNP-type Pincer Ligands Leads to the Catalytic Reduction of Dinitrogen into Ammonia. *Nat. Chem.* 2011, 3, 120−125.

(8) Arashiba, K.; Kinoshita, E.; Kuriyama, S.; Eizawa, A.; Nakajima, K.; Tanaka, H.; Yoshizawa, K.; Nishibayashi, Y. Catalytic Reduction of Dinitrogen to Ammonia by Use of Molybdenum−Nitride Complexes Bearing a Tridentate Triphosphine as Catalysts. *J. Am. Chem. Soc.* 2015, 137, 5666−5669.

(9) Arashiba, K.; Eizawa, A.; Tanaka, H.; Nakajima, K.; Yoshizawa, K.; Nishibayashi, Y. Catalytic Nitrogen Fixation via Direct Cleavage of Nitrogen−Nitrogen Triple Bond of Molecular Dinitrogen under Ambient Reaction Conditions. *Bull. Chem. Soc. Jpn.* 2017, 90, 1111−1118.

(10) Eizawa, A.; Arashiba, K.; Tanaka, H.; Kuriyama, S.; Matsuo, Y.; Nakajima, K.; Yoshizawa, K.; Nishibayashi, Y. Remarkable Catalytic Activity of Dinitrogen-bridged Dimolybdenum Complexes Bearing NHC-based PCP-pincer Ligands Toward Nitrogen Fixation. *Nat. Commun.* 2017, 8, No. 14874.

(11) Azofra, L. M.; Li, N.; MacFarlane, D. R.; Sun, C. Promising Prospects for 2D d^2−d^4 M$_3$C$_2$ Transition Metal Carbides (MXenes) in N$_2$ Capture and Conversion into Ammonia. *Energy Environ. Sci.* 2016, 9, 2545−2549.

(12) Abghoui, Y.; Garden, A. L.; Hlynsson, V. F.; Björgvinsdóttir, S.; Ólafsdóttir, H.; Skúlason, E. Enabling Electrochemical Reduction of Nitrogen to Ammonia at Ambient Conditions Through Rational Catalyst Design. *Phys. Chem. Chem. Phys.* 2015, 17, 4909−4918.

(13) Liu, N.; Nie, L.; Xue, N.; Dong, H.; Peng, L.; Guo, X.; Ding, W. Catalytic Ammonia Synthesis over Mo Nitride/ZSM-5. *ChemCatChem* 2010, 2, 167−174.

(14) Li, Q.; He, L.; Sun, C.; Zhang, X. Computational Study of MoN$_2$ Monolayer as Electrochemical Catalysts for Nitrogen Reduction. *J. Phys. Chem. C* 2017, 121, 27563−27568.

(15) Zhao, J.; Chen, Z. Single Mo Atom Supported on Defective Boron Nitride Monolayer as an Efficient Electrocatalyst for Nitrogen Fixation: A Computational Study. *J. Am. Chem. Soc.* 2017, 139, 12480−12487.

(16) Ling, C.; Bai, X.; Ouyang, Y.; Du, A.; Wang, J. Single Molybdenum Atom Anchored on N-Doped Carbon as a Promising Electrocatalyst for Nitrogen Reduction into Ammonia at Ambient Conditions. *J. Phys. Chem. C* 2018, 122, 16842−16847.

(17) Chen, Z. W.; Lang, X. Y.; Jiang, Q. Discovery of Cobweb-like MoC$_6$ and its Application for Nitrogen Fixation. *J. Mater. Chem. A* 2018, 6, 9623−9628.

(18) Perdew, J. P.; Burke, K.; Ernzerhof, M. Generalized Gradient Approximation Made Simple. *Phys. Rev. Lett.* 1996, 77, No. 3865.

(19) Hammer, B. H.; Hansen, L. B.; Nørskov, J. K. Improved Adsorption Energetics within Density-functional Theory Using Revised Perdew-Burke-Ernzerhof Functionals. *Phys. Rev. B* 1999, 59, No. 7413.

(20) Abghoui, Y.; Skúlason, E. Onset Potentials for Different Reaction Mechanisms of Nitrogen Activation to Ammonia on Transition Metal Nitride Electro-catalysts. *Catal. Today* 2017, 286, 69−77.

(21) Abghoui, Y.; Garden, A. L.; Hlynsson, V. F.; Björgvinsdóttir, S.; Ólafsdóttir, H.; Skúlason, E. Enabling Electrochemical Reduction of Nitrogen to Ammonia at Ambient Conditions Through Rational Catalyst Design. *Phys. Chem. Chem. Phys.* 2015, 17, 4909−4918.

(22) Abghoui, Y.; Garden, A. L.; Howalt, J. G.; Vegge, T.; Skúlason, E. Electroreduction of N$_2$ to Ammonia at Ambient Conditions on Mononitrides of Zr, Nb, Cr, and V: A DFT Guide for Experiments. *ACS Catal.* 2016, 6, 635−646.

(23) Skúlason, E.; Bligaard, T.; Gudmundsdóttir, S.; Studt, F.; Rossmeisl, J.; Abild-Pedersen, F.; Vegge, T.; Jónsson, H.; Nørskov, J. K. A Theoretical Evaluation of Possible Transition Metal Electro-catalysts for N$_2$ Reduction. *Phys. Chem. Chem. Phys.* 2012, 14, 1235−1245.

(24) Wilkinson, G.; Stone, F. G. A.; Abel, E. W. *Comprehensive Organometallic Chemistry*; Pergamon Press, 1982.

(25) Zeinalipour-Yazdi, C. D.; Hargreaves, J. S. J.; Catlow, C. R. A. DFT-D$_3$ Study of Molecular N$_2$ and H$_2$ Activation on Co$_3$Mo$_3$N Surfaces. *J. Phys. Chem. C* 2016, 120, 21390−21398.

(26) Singh, A. R.; Rohr, B. A.; Schwalbe, J. A.; Cargnello, M.; Chan, K.; Jaramillo, T. F.; Chorkendorff, I.; Nørskov, J. K. Electrochemical Ammonia Synthesis—The Selectivity Challenge. *ACS Catal.* 2017, 7, 706−709.

(27) Montoya, J. H.; Tsai, C.; Vojvodic, A.; Nørskov, J. K. The Challenge of Electrochemical Ammonia Synthesis: A New Perspective on the Role of Nitrogen Scaling Relations. *ChemSusChem* 2015, 8, 2180−2186.

(28) Vojvodic, A.; Medford, A. J.; Studt, F.; Abild-Pedersen, F.; Khan, T. S.; Bligaard, T.; Nørskov, J. K. Exploring the Limits: A Low-pressure, Low-temperature Haber-Bosch Process. *Chem. Phys. Lett.* 2014, 598, 108−122.

(29) Zhou, F.; Azofra, L. M.; Ali, M.; Kar, M.; Simonov, A. N.; McDonnel-Worth, C.; Sun, C.; Zhang, X.; MacFralane, D. R. Electro-Synthesis of Ammonia from Nitrogen at Ambient Temperature and Pressure in Ionic Liquids. *Energy Environ. Sci.* 2017, 10, 2516−2520.

(30) Suryanto, B. H. R.; Kang, C. S. M.; Wang, D.; Xiao, C.; Zhou, F.; Azofra, L. M.; Cavallo, L.; Zhang, X.; MacFarlane, D. R. Rational Electrode−Electrolyte Design for Efficient Ammonia Electrosynthesis under Ambient Conditions. *ACS Energy Lett.* 2018, 3, 1219−1224.

(31) Montoya, J. H.; Tsai, C.; Vojvodic, A.; Nørskov, J. K. The Challenge of Electrochemical Ammonia Synthesis: A New Perspective on the Role of Nitrogen Scaling Relations. *ChemSusChem* 2015, 8, 2180−2186.

(32) Asnavandi, M.; Yin, Y.; Li, Y.; Sun, C.; Zhao, C. Promoting Oxygen Evolution Reactions through Introduction of Oxygen Vacancies to Benchmark NiFe−OOH Catalysts. *ACS Energy Lett.* 2018, 3, 1515−1520.

(33) Zhao, S. L.; Wang, Y.; Dong, J. C.; He, C. T.; Yin, H. J.; An, P. F.; Zhao, K.; Zhang, X. F.; Gao, C.; Zhang, L. J.; Lv, J. W.; Wang, J. X.; Zhang, J. Q.; Khattak, A. M.; Khan, N. A.; Wei, Z. X.; Zhang, J.; Liu, S. Q.; Zhao, H. J.; Tang, Z. Y. Ultrathin Metal-Organic Framework Nanosheets for Electrocatalytic Oxygen Evolution. *Nat. Energy* 2016, 1, No. 16184.

(34) Zhang, X.; Chen, A.; Zhang, Z.; Zhou, Z. Double-atom catalysts: transition metal dimer-anchored C2N monolayers as N2 fixation electrocatalysts. *J. Mater. Chem. A* 2018, 6, 18599−18604.

(35) Chen, P.; Li, N.; Chen, X.; Ong, W.; Zhao, X. The Rising Star of 2D Black Phosphorus Beyond Graphene: Synthesis, Properties and Electronic Applications. *2D Mater.* 2018, 5, No. 014002.

(36) Tan, W. C.; Cai, Y.; Ng, R. J.; Huang, L.; Feng, X.; Zhang, G.; Zhang, Y.; Nijhuis, C. A.; Liu, X.; Ang, K. Few-Layer Black Phosphorous Carbide Field-Effect Transistor via Carbon Doping. *Adv. Mater.* 2017, 29, No. 1700503.

58

(37) Agnoli, S.; Favaro, M. Doping Graphene with Boron: A Review of Synthesis Methods, Physicochemical Characterization, and Emerging Applications. *J. Mater. Chem. A* **2016**, *4*, 5002−5025.

59

Chapter 7 Summary and Future Work

7.1 Key Results

Through computational calculations, this PhD project has investigated 20 graphene-based structures (Chapter 2), 3 typical 2D materials (Chapters 3-5) and 21 Mo-L3 SACs (Chapter 6). The calculated results and key conclusions are summarized: (i) Graphene-based structures present $\Delta G_{max} \approx 0.9 - 2.4$ eV, depending on the local active sites, and lowly coordinated carbon (LCC) has been identified as active sites for NRR; (ii) for 2D catalysts, Fe-doped MoN_2 and H-terminated $FeB_6(\beta)$ are promising, with $\Delta G_{max} = 0.47$ eV and 0.28 eV, respectively, while Mo2C performance is relatively poor with $\Delta G_{max} = 1.0$-1.4 eV, due to heavy H-termination; (iii) Mo-L3 is an excellent bonding network for NRR, with B, P, C as the recommended ligands as indicated by calculated ΔG_{max}, 0.47 eV for $Mo-P_2B$, 0.36 eV for $Mo-PC_2$ and 0.60 eV for $Mo-BC_2$.

Given that NRR over H-terminated $FeB_6(\beta)$ is actually catalysed by single iron, such $FeB_6(\beta)$ is actually a special single-Fe catalyst. Therefore, this project has identified two categories of active sites for NRR, namely defects and single atoms. High reactivity offered by LCC-rich graphene and Fe-doped MoN_2 origins from defects, and $FeB_6(\beta)$/Mo-L3 catalysts are supported by SACs. In terms of electronic structures, both empty orbitals and dangling bonds associated with these active sites play the key role. As demonstrated for graphene case, LCC active sites need special agent to stabilize; otherwise, high reactivity will lose after H-termination (see Chapter 2). Similar situation has been met for NV-dominated MoN_2, Mo_2C surface, FeB_6 and Mo-L3. Therefore, H-termination is critical for NRR catalysts.

Hydrogen evolution reaction (HER) is another important reason to study H-termination. HER is the major side reaction, but abundant protons are essential for NRR. Therefore, it is essential to compare ΔG_{max} for HER and NRR, as demonstrated in Chapters 5&6. Given H_2 is released through $H^* + (H^+ + e^-) \rightarrow H_2$ or $H^* + H^* \rightarrow H_2$, the suppression of H* formation should be effective to improve NRR selectivity, which in turn protects active sites from H-terminals, as described in Chapter 2.

Computational practice by this project also advances the knowledge for NRR catalyst design, especially on how to optimize the thermodynamics of elementary steps. In chemistry, one cannot change the overall thermodynamics for a reaction, but major opportunities can be found from the mediation for elementary steps. A basic principle is to split a difficult job, like NRR, to several steps with smaller difficulties. Given NRR is a spontaneous process, catalysts which can boost the reaction with very small thermodynamic barrier are possible, as listed in Chapter 1 (Tables 1 and 2) and demonstrated in chapter 4 (0.28 eV for H-terminated FeB_6).

The high performance of promising candidates is the breakage of linear constraint relationship between intermediates [1]. As demonstrated in Chapters 4&6, several single-atom catalysts deviate from the linear relationship. A possible reason is that lowly coordinated atoms, like single atoms on 2D substrates, bring unique interactions. For instance, LCC in graphene can be stabilized by N_2 adsorption due to the stabilization of dangling bonds (Chapter 2). Similarly, iron in FeB_6 can also be stabilized by adsorbed N_2 and H. Smart introduction of stable active sites into the substrate is thus a key direction for following design of NRR catalysts.

Such ration design can be guided from efficient screening, as demonstrated in Chapter 6, in which 21 Mo-L3 concept catalysts have been screened. Further, unsuccessful candidates can be effectively improved through doping (e.g, MoN_2, by Fe-doping, Chapter 3), changing coordination (Fe-B system, Chapter 5) and ligands optimization (Mo-L3, Chapter 6). Specifically, the following strategy works well from my practise. Overall, two NH_3 molecules should be produced from the full reduction of each N_2, with six couples of proton and electron. For the first NH_3 production, strong catalyst-N interaction is favourable due to the need to activate N_2, but for the second, weak catalyst-N bonding is beneficial for NH_3 release. This justifies the volcano curve: Catalyst-N with medium strength is ideal; therefore, adsorption energy of single N can be employed as an indicator for accurate electronic mediation. Similarly, adsorption energy of single H from computation can be a valid indicator for HER, guiding experimental efforts for both NRR thermodynamics and selectivity.

Last but not least, Fe, Mo and B are the most promising earth-abundant elements for NRR, as supported by mechanism of nitrogenases in nature [2] and large amount of experiments and calculations [3-5]. This project demonstrates that the case for Fe-doped MoN_2, Mo-L3 and FeB_6, but Mo_2C is not among these promising ones. A primary analysis on the effect of ligands on d-band of transition metals has been presented, and such knowledge could be useful for future catalysts design.

7.2 Future Work

It is worth to note two huge gaps in NRR research. The first one is the performance of current catalysts and the expectation from the industry. Specifically, the yield R and the Faraday efficiency (FE) need to be ~10^{-7} mol s^{-1}cm^{-2} and FE > 90% (FE=100% means all electrons are used for NH$_3$ production) [6]. So far, however, the performance of electrochemical synthesis is typically shown as R<10^{-9} mol s^{-1}cm^{-2} and FE<30% [3-5]. This highlights a huge space for further improvement, providing an opportunity for computational design.

Catalyst design and optimization is undoubtedly the focus for following NRR research. Following this, additional efforts could be made on the design of novel catalysts, such as p-block catalyst (e.g., boron) as emerged in recent years. In addition, integrated design should be seriously considered, such as the balance between thermodynamics optimization and kinetics consideration, the improvement of NRR and suppression of HER.

In Chapter 2, lowly coordinated carbon (LCC) has been proposed as potential active sites for NRR, as metal-free catalysts. This is a new concept, while its stability and NRR performance are poorly known yet. Primary work has been done with this PhD project (see Appendices, **Primary results for LCC stability**), and additional work should be done with optimized computational methods to handle large systems so that the effect of proton and metal ions (e.g., K+, Na+, etc.) can be fully considered.

Fresh idea is highly expected for future design. Although SACs are very successful, it is worth to note that SACs are not perfect for multiple step reactions, like NRR, due to the nature of single-site catalysis. Therefore, catalysts with multiple active centres (MAC) could be a specific direction for NRR catalyst design. Primary work has been done with this PhD project (see Appendices, **Primary results for MACs Design**), which vividly shows that MACs can effectively break the linear relationship and improves catalyst performance.

For integrated design, several challenges should be addressed fully, including kinetics prediction, solution effect (for buffer optimization), and multiple-electron coupled reactions, which needs strong capacity to handle large systems at the electronic level. Moreover, electron transfer over the complex interface between electrolyte (with the solution, buffer, N$_2$) and catalyst surfaces (charged or uncharged) calls for better theoretical strategies, which is very challenging, but of paramount importance.

7.3 References

[1] E. Skúlason, et al. *Phys. Chem. Chem. Phys*. 2012, 14, 1235.

[2] B.M. Hoffman, D. Lukoyanov, Z.-Y. Yang, D.R. Dean, and L. C. Seefeldt, *Chem. Rev.* 2014, 114, 4041–4062.

[3] C. Guo, J. Ran, A. Vasileff and S.-Z. Qiao, *Energy Environ. Sci.*, 2018, 11, 45-56.

[4] N. Cao and G. Zheng, *Nano Res.*, 2018, 11, 2992-3008.

[5] G.-F. Chen, S. Ren, L. Zhang, H. Cheng, Y. Luo, K. Zhu, L.-X. Ding and H. Wang, *Small Methods*, 2018, 1800337

[6] I.J. McPherson, et al. *Dalton Trans*. 2019, 48, 1562-1568.

Appendices

Computational Setting

During this project, NRR has been studied through calculating the free energy change associated with various elementary steps. All geometries are fully relaxed under the spin-polarized DFT method. The calculations have been carried out under the generalized gradient approximation (GGA) [1], together with the functional by Perdew, Burke, and Ernzerhof [2], as embedded in the Vienna Ab-Initio Simulation Package [3]. K-space is sampled by the Monkhorst-Pack scheme, and the cutoff energy is set as 380 eV. The van der Waals interaction has been considered with the use of DFT-D3 method, as developed by Grimme and co-workers [4, 5]. All calculations have been carried out on Australian National Computational Infrastructure (NCI).

[1] Kohn, W; Sham, L. M. Phys Rev **1965**, 140, A1133.

[2] Perdew, J. P.; Burke, K.; Ernzerhof, M. Phys. Rev. Lett. **1996**, 77, 3865.

[3] Kresse, G.; Joubert, D. Phys. Rev. B **1999**, 59, 1758.

[4] Goerigk, L.; Grimme, S. J. Chem. Theory Comput. **2010**, 6, 107.

[5] Grimme, S.; Ehrlich, S.; Goerigk, L. J. Comput. Chem. **2011**, 32, 1456.

Supporting Information for Chapter 2

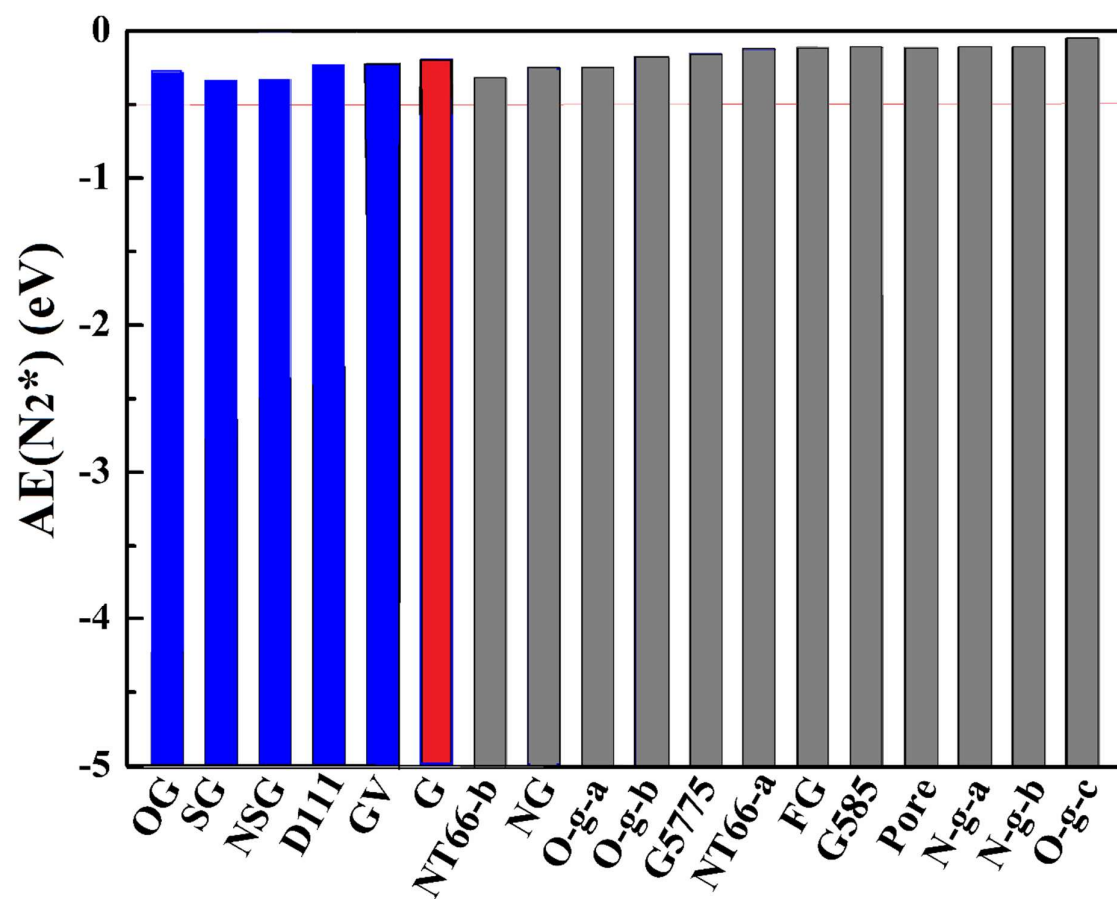**Insight into the Reactivity of Carbon Structures for Nitrogen Reduction Reaction**

Qinye Li,[a] Siyao Qiu,[b] Chuangwei Liu,[c] Fengling Zhou,[b] Lizhong He,[a] Xiwang Zhang,[*,a] Chenghua Sun[*,d]

[a] School of Chemical Engineering, Monash University, Clayton, Victoria 3800, Australia

[b] Science & Technology Innovation Institute, Dongguan University of Technology, Dongguan 523808, China

[c] School of Chemistry, Monash University, Clayton, Victoria 3800, Australia

[d] Department of Chemistry and Biotechnology, Center for Translational Atomaterials, Faculty of Science, Engineering & Technology, Swinburne University of Technology, Hawthorn, VIC 3122, Australia

Figure S1 Calculated adsorption energies for N_2 on different active sites listed in Scheme 1.
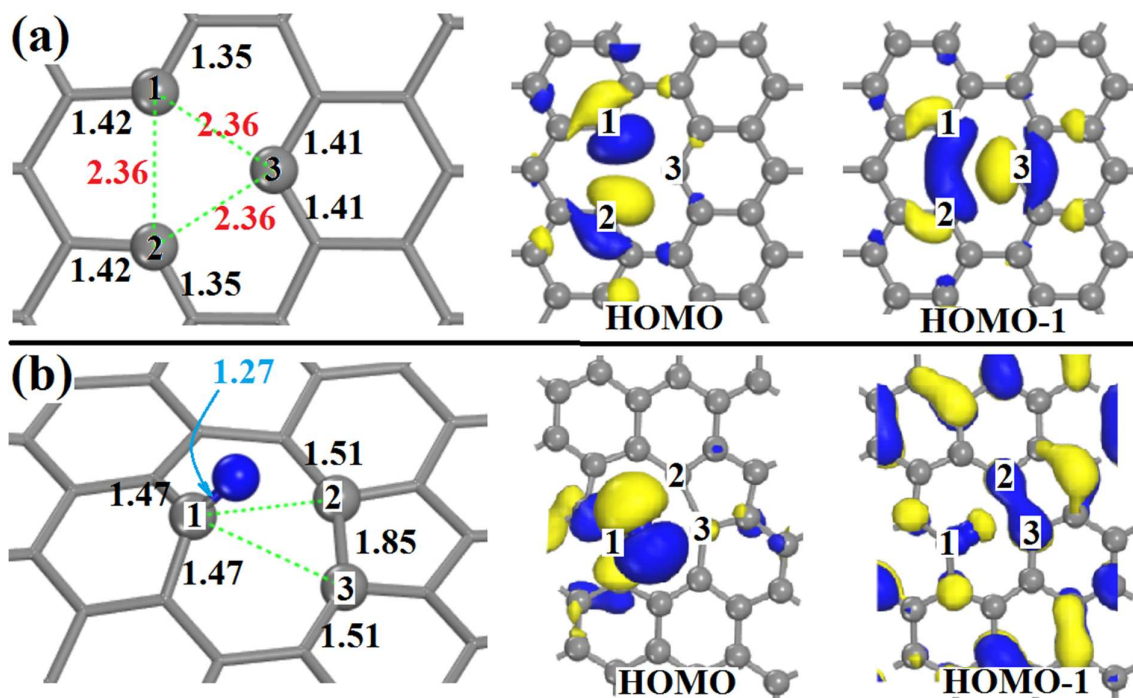
Figure S2 Molecular orbitals for catalyst GV. (a) LCC shown in optimized GV and HOMO&HOMO-1 for GV; (b) N* adsorbed over GV and HOMO&HOMO-1 for N*.

Table S1 Experimental data for carbon-based NRR catalysts.

Reference information	Catalyst	Properties		Active Sites
		Yield	FE	
J. Am. Chem. Soc. 139, 9771 (2017)	Li+ incorporation into poly(N-ethyl-benzene-1,2,4,5-tetracarboxylic diimide)	2 ug h^{-1} cm^{-2}	3%	Li+ sites in PEBCD
Chem Comm. 54, 11188 (2018)	Nitrogen-free commercial carbon cloth; Na$_2$SO$_4$ electrolyte	2.59 ×10^{-10} mol cm^{-2} s^{-1}	6.92%	
Small Methods 1800251 (2018)	S-doped carbon nanospheres Na$_2$SO$_4$ electrolyte	19.07 μg h^{-1} mg^{-1} cat	7.47%	S-doping
ACS Energy Lett. 4, 377 (2019)	biomass-derived porous carbon	1.31 mmol h^{-1} g^{-1} cat.	9.98%	pyridinic-N; N-vacancies
ACS Catal., 8, 1186 (2018)	N-doped Porous Carbon H2SO4 electrolyte	0.84 μmol cm^{-2} h^{-1}		
Nano Energy 48, 217 (2018)	MOF-derived N-doped disordered carbon	3.4×10^{-6} mol cm^{-2} h^{-1}	10.2%	
Chem. Comm. 55, 2684 (2019)	O-doped hollow carbon	25.12 lg h^{-1} mg cat^{-1}	9.1%	oxygen dopants
Chem. Comm. 55, 4266 (2019)	Defect-rich fluorographene nanosheets	9.3 lg h^{-1} mg cat^{-1}	4.2%	
Chem. Comm. 55, 4997 (2019)	oxidized carbon nanotubes	32.33 lg h^{-1} mgcat^{-1}	12.5%	-CO group
Chem. Comm. 55, 3371 (2019)	S-doped graphene	27.3 μg h^{-1} mgcat^{-1}	11.5%	carbon atoms close to S-dopants
ChemElectroChem, 6, 2215 (2019)	Polyaniline（PANI）	5.45×10^{-11} mols^{-1}cm^{-2}	3.76%	Functional groups
J Mater Sci. 54, 9088 (2019)	N-S codoped graphene	7.7 μg h^{-1} mg-1	5.8%	
J. Mater. Chem. A 10.1039/C9TA03654G (2019)	perylene-3,4,9,10-tetracarboxylic acid nanorod-reduced graphene oxide	24.7 μg h^{-1} mg^{-1}cat^{-1}	6.9%	surface of PTCA-rGO

Table S2 Calculated ΔG for full NRR catalysed by G, OG, D111, SG, NSG, and GV in unit of eV. Intermediate states are labelled as N_2^*, N_2H^*, NNH_2^*, N^*, NH^*, NH_2^*, and NH_3^*. After NH_3 released, the catalyst gets back to clean surface, as S.

Distal Mechanism

	N_2^*	N_2H^*	NNH_2^*	N^*	NH^*	NH_2^*	NH_3^*	S	$\Delta Gmax$
G	0.35	2.27	0.81	-0.27	-1.36	-0.83	-1.05	-0.33	2.27
OG	0.12	2.10	0.44	-1.40	-1.68	0.62	-1.14	-0.52	2.10
D111	0.38	0.65	0.23	0.68	-1.31	-1.79	-1.35	2.07	2.07
SG	0.48	2.43	0.55	-1.05	-0.79	0.43	-1.89	-0.58	2.43
NSG	0.49	2.09	0.28	0.12	-1.37	0.28	-1.79	-0.53	2.09
GV	0.47	0.35	-1.12	0.25	-1.46	-0.10	1.21	-0.02	1.21

Alternating Mechanism

	N_2^*	N_2H^*	$NHNH^*$	$NHNH_2^*$	NH^*	NH_2^*	NH_3^*	S	$\Delta Gmax$
G	0.35	2.27	0.15	-0.05	-0.91	-0.83	-1.05	-0.33	2.27
OG	0.12	2.10	-0.16	-0.22	-1.45	0.62	-1.14	-0.52	2.10
D111	0.38	0.65	0.31	-0.71	0.00	-1.79	-1.35	2.07	2.07
SG	0.48	2.43	-0.05	0.00	-1.24	0.43	-1.89	-0.58	2.43
NSG	0.49	2.09	0.20	-0.65	-0.51	0.28	-1.79	-0.53	2.09
GV	0.47	0.35	-0.50	-0.12	-1.70	-0.10	1.21	-0.02	1.21

Supporting Information for Chapter 4

Exploration of iron borides as electrochemical catalysts for nitrogen reduction reaction

Qinye Li,[a] Chuangwei Liu,[b] Siyao Qiu,[c] Fengling Zhou,[c] Lizhong He,[a] Xiwang Zhang,[*a] and Chenghua Sun[*cd]

[a.] *School of Chemical Engineering, Monash University, Clayton, Victoria 3800, Australia. E-mail: xiwang.zhang@monash.edu*

[b.] *School of Chemistry, Faculty of Science, Monash University, Clayton, Victoria 3800, Australia*

[c.] *Science & Technology Innovation Institute, Dongguan University of Technology, Dongguan, China*

[d.] *Department of Chemistry and Biotechnology, and Centre for Translational Atomaterials, FSET, Swinburne University of Technology, Hawthorn, Victoria 3122, Australia. E-mail: chenghuasun@swin.edu.au*

Section 1. Computational tests

Before running the calculations, cutoff energy and k-points have been tested, using FeB and FeB-N_2 as an example. The tested results are shown below:

	Cutoff energy test with K=1×1×1			K-point test with Cutoff energy=380 eV		
	380 eV	420 eV	450 eV	1×1×1	3×3×1	5×5×1
E(FeB) (eV)	-227.486	-227.464	-227.461	-227.486	-229.753	-229.696
E(FeB-N2) (eV)	-248.744	-248.746	-248.747	-248.744	-250.946	-250.892

Based on the tests, cutoff energy of 380 eV and k-space has been sampled with 3×3×1 as higher setting can only improve the reaction energy slightly (<0.06 eV).

Section 2. Space groups and lattice parameters for four Fe-B compounds

	Space Group	Lattice parameters		
FeB	Pnma	a= 4.00 Å b=5.41 Å; c= 2.95 Å(this work) α= β= γ=90° a=4.05 Å; b= 5.49 Å; c= 2.95 Å [1,2]		Note
FeB2	P6/mmm	a= b= 3.01 Å (this work) α=β=90°; γ=120° a=b=3.05 Å [2] a= b = 3.18 [3] a= b = 3.02 [4]		FeB+FeB2 mixed; AlB2-type
FeB6(α)	P6/mmm	a= b = 4.46 Å α=β=90°; γ=88.05° (this work) a= b = 4.45 Å [5] α=β=90°; γ=88.05°		Jahn−Teller effect
FeB6(β)	P6/mmm	a=b=4.80 (this work) α=β=90°; γ=120° a=b=4.75 [6] α=β=90°; γ=120°		

References:

[1] Z. Kristallogr. 2006, 221, 477–481 (Experiments)

[2] *Metal Science and Heat Treatment. 2013, 55, 68–72. (Experiments)*

[3] Nano Lett. 2016, 16, 6124-6129 (Computational work)

[4] Materials Project. (No. mp-569376) https://materialsproject.org/materials/mp-569376/

[5] J. Am. Chem. Soc. 2016, 138, 5644−5651.

[6] J. Mater. Chem. C, 2016, 4, 9613—9621.

Section 3. Tests for N_2 adsorption on four compounds. Calculated total energies are listed in unit of eV. The bold numbers are the total energies for most stable configurations.

Tested N_2 adsorption

	Fe-site	Fe-B sites	Fe-Fe sites	Enzymatic	Dissociative	B-Site
FeB-N2	**-250.892**	-248.611	-248.865	-248.074	-247.751	-249.241
FeB2-N2	-202.791	-202.790*	-202.764	-201.796	**-203.472**	-200.332
FeB6(α)-N2	**-111.527**	-111.408	Fe-Fe is too far	-110.833	-108.384	-109.484
FeB6(β)-N2	**-111.464**	-111.241	Fe-Fe is too far	-111.194	-105.886	-110.546

* It changes to sole Fe-site adsorption.

Calculated N_2H dissociation on four compounds.

| Catalysts	N_2H^*	N^*+NH^*	deltaE($N_2H^* \rightarrow N^*+NH^*$)
FeB	-253.486	-251.961	1.525
FeB2	-204.812	-207.208	-2.396
FeB6(α)	-204.328	-202.481	1.847
FeB6(β)	-111.655	-110.003	1.652

Primary results for LCC stability

In **Chapter 2**, LCC has been proposed as the potential active sites for NRR. To support this new concept, LCC at armchair and zigzag edge sites of graphene monolayer has been particularly studied as general models for LCC. The calculated results are shown below. It is clear that these LCC sites are very reactive to adsorb and reduce N_2. It is also worth to note that the regeneration of LCC is energy-consuming, being up to ~1.7 eV and ~2.2 eV for armchair and zigzag LCC, respectively. To better understand whether such LCC will be terminated by protons, an energy scan for proton diffusion from the solution to bond with LCC has been performed, as shown in Fig. S4. It is clear that H-termination can remarkably reduce the total energy of the system, by ~4.5 eV and ~2.2 eV when LCC is at armchair and zigzag edge sites, respectively. This is not surprising as H-LCC bonding reduces radicals. However, from Fig. S4b, a barrier for proton diffusion has been observed, suggesting that LCC can survive for some time, depending on the concentration of the solution and the kinetics for H-diffusion. Therefore, LCC is likely to interact with N_2 before H-LCC bond is generated.
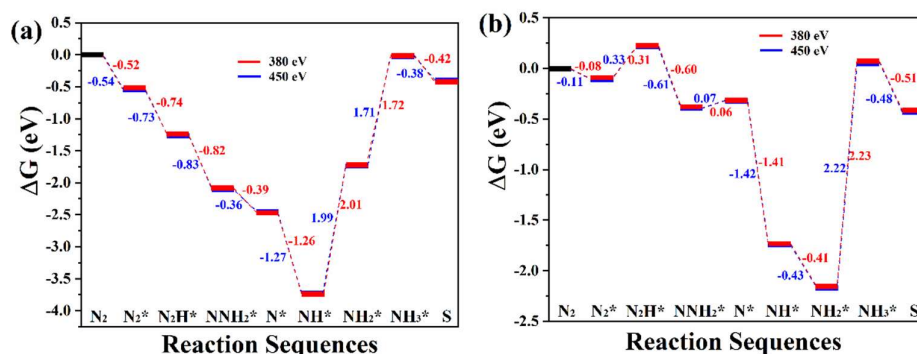

Figure S3 Calculated NRR performance for LCC at (a) Armchair carbon and (b) Zigzag carbon. Two cutoff energies (380 eV and 450 eV) have been tested.
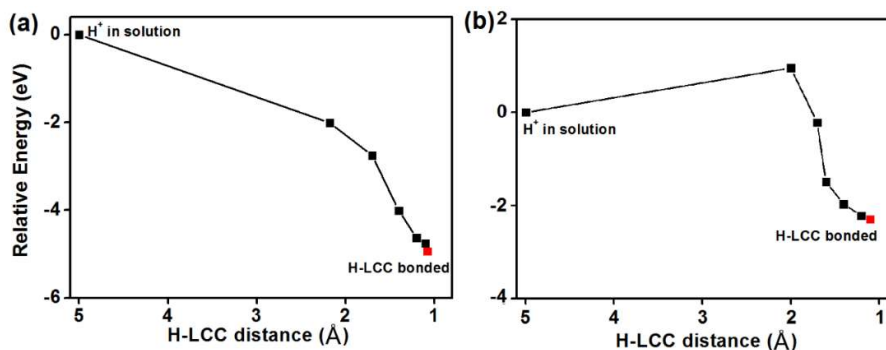
Figure S4 Calculated relative energies versus H-LCC distance. (a) LCC at armchair edge site; and (b) LCC at zigzag edge site.

Primary results for MACs design

In **Chapter 7**, MACs have been proposed as new concept catalysts in this PhD thesis. To support such concept, a primary collaboration work has been presented in Fig. S5, in which M3-featured MACs with three metal atoms to form a cluster are loaded on g-C_3N_4 for NRR. The NRR performance of these catalysts with M=Fe, Cu, Ru and Mo has been investigated. And it is clearly shown that MACs can perform much better than M1 SACs. Moreover, such improvement origins from the breakage of linear relationship associated with the intermediate states associated with NRR elementary steps. This primary result supports the MACs concept, but more efforts are needed to generate more MAC examples to establish a full understanding.
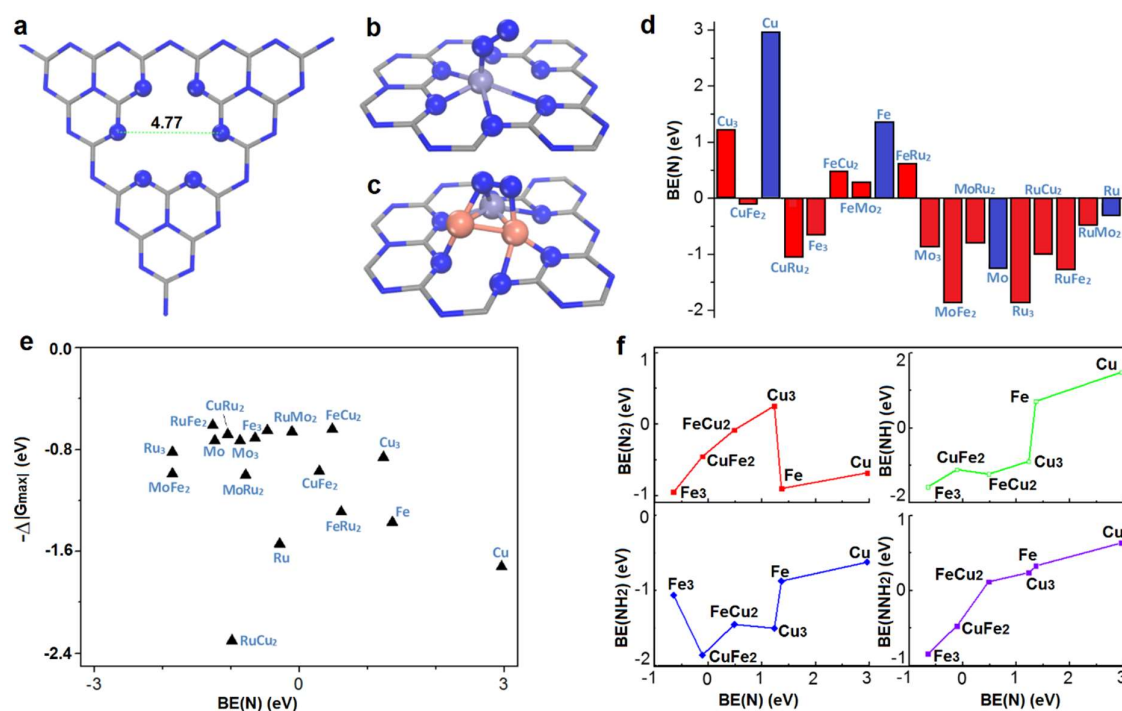
Fig. S5 Computational scanning of MACs and SACs. (a) g-C_3N_4 substrate; (b) N_2 adsorption on M1(SAC); (c) N_2 adsorption on M3 (MAC); (d) calculated BE(N); (e) calculated ΔGmax; (f) calculated BE(NxHy) versus BE(N).